ASSESSING INTERNAL CONTAMINATION AFTER A RADIOLOGICAL DISPERSION DEVICE EVENT USING A 2X2-INCH SODIUM-IODIDE DETECTOR

A Thesis
Presented to
The Academic Faculty

By

Shaheen Azim Dewji

In Partial Fulfillment
Of the Requirements for the Degree
Master of Science in the
School of Nuclear and Radiological Engineering

Georgia Institute of Technology

May 2009

ASSESSING INTERNAL CONTAMINATION AFTER A RADIOLOGICAL DISPERSION DEVICE EVENT USING A 2X2-INCH SODIUM-IODIDE DETECTOR

Approved by:

Dr. Nolan E. Hertel, Advisor
School of Nuclear and Radiological Engineering
Georgia Institute of Technology

Dr. Chris Wang
School of Nuclear and Radiological Engineering
Georgia Institute of Technology

Dr. Armin Ansari
Radiation Studies Branch
Centers for Disease Control and Prevention

Date Approved: March 2, 2009

ACKNOWLEDGEMENTS

I must first start by thanking God for guidance – everyday I say *Shukar Alhamdulliah* for the opportunities I have been granted. They are certainly the manifestation of God's plan for me, and I pray for guidance in my future endeavors.

I would like to extend my deep gratitude to Dr. Nolan Hertel, who has become much more than an adviser these past few years. You have truly instilled confidence in my abilities as an engineer, and I have learned a great deal from you – both inside and outside the lab. I will forever consider myself fortunate to have such a charismatic mentor, and hope that we are able to collaborate for many years to come.

I would also like to thank my committee, Drs. Chris Wang and Armin Ansari, for their guidance throughout the duration of my academic and research endeavors in graduate school. None of this work would be possible without the collective research efforts of my colleagues in Team Hertel – it was a privilege and pleasure to work alongside all of you. I would especially like to thank Eric Burgett, whose open-door policy has helped me to overcome obstacles and progress in my research. All of your contributions are greatly appreciated!

Of course, I would like to thank my family (my other "committee") – Mom, Dad, and Sheliza (my mini-adviser!). Your love, support, and prayers have been my motivation and the driving factor behind my accomplishments. Last, but not least, I would like to thank my cousin, Farooq Habib, who initially encouraged that I undertake graduate studies in engineering in the first place.

TABLE OF CONTENTS

LIST OF TABLES

LIST OF FIGURES

SUMMARY

The detonation of a radiological dispersion device (RDD) may result in a situation where many individuals are exposed to contamination due to the inhalation of radioactive materials. Assessments of contamination may need to be performed by emergency response personnel in order to triage a potentially exposed public. The feasibility of using readily available standard 2x2-inch sodium-iodide [NaI(Tl)] detectors to determine the internal contamination level of a patient following the acute inhalation of a radionuclide has been investigated.

An assessment of the level of contamination after a selected period of time requires computer modeling, since the inhalation and distribution of nuclides cannot readily be modeled in the laboratory. The 2x2-NaI(Tl) detector response was simulated using MCNP-5 [1], and the model was validated via a series of experimental benchmark measurements using a polymethyl methacrylate (PMMA) slab phantom. Upon collecting experimental data using PMMA thicknesses ranging from 0-mm to 90-mm in 6-mm increments, the measurements were simulated using MCNP. The detector response was calculated for six radionuclides to ensure that the detector model was validated over a broad range of gamma-ray energies. The integrated photopeaks in the benchmark measurements were compared with the corresponding MCNP model. From these comparisons, scaling factors were calculated for each nuclide. The purpose of simulating multiple thicknesses was to verify that each nuclide scaling factor was constant regardless of chest-wall thickness, thus showing no variance in detector response. Such validation is essential in reproducing the actual detector response for extended geometries and sources.

Upon verification of the detector model, six anthropomorphic phantoms (Reference Male, Reference Female, Adipose Male, Adipose Female, Post-Menopausal Adipose Female, and Child) based on the MIRD-V (Medical Internal Radiation Dose) phantoms [2] were used to model nuclides distributed to simulate inhaled contamination. The nuclides assessed with the anthropomorphic phantoms included ^{241}Am, ^{60}Co, ^{137}Cs, ^{131}I, and ^{192}Ir. The modeling assumed that all external contamination had already been removed and that only one radionuclide was inhaled and has been identified. The detectors were placed at four positions on the phantoms: anterior right torso, posterior right torso, anterior neck, and lateral left thigh. The detected count-rate varied with respect to detector position and the resulting optimal detector location was determined on the body. The simulation data were used with biokinetic modeling data to determine time-dependent count-rate values for each radionuclide. Threshold limits were determined for use in triaging, based on an intake that would lead to a minimum committed effective dose of 250-mSv [3]. The source distribution and activity in the body as a function of post-inhalation time was determined using the Dose and Risk Calculation software (DCAL) [4].

The detector response was determined as a function of count-rate per becquerel of activity at initial intake. This was converted to a count-rate value per 250-mSv of intake for triage use by first responders. A set of procedure sheets for use by first responders was compiled for each of the phantoms and nuclides investigated. These procedure sheets were designed to instruct first responders in detector use, determination of background, acquisition of patient data, and the use of count-rate decision levels to determine if further medical attention is required. Although readily available, the 2x2-NaI(Tl) requires initial set-up and calibration by a skilled technician before use by first responders with limited experience in radiation detection instrumentation.

CHAPTER 1: INTRODUCTION

The attacks of September 11, 2001 have stirred the nation to strengthen its homeland security defenses and have reaffirmed the need to refine emergency preparedness in the purview of an imminent terrorist threat using weapons of mass destruction (WMD). Although a "nuclear 9/11" or an attack using a fission-based weapon are of paramount concern, the concerns regarding WMDs have also extended to include radiological terrorism. A radiological dispersion device (RDD), colloquially referred to as a "dirty bomb", is a radiological weapon that employs conventional explosives with radioactive material with the purpose of dispersing radioactive material and consequently contaminating a large area or population with the possibility of causing severe radiation induced-illnesses to its victims. The use of an RDD is not just limited to the use of explosive means to disperse radioactive material, but can also disperse radiological contamination passively using aerosolized material. The use of such a weapon by extremists would cause ubiquitous psychological and economic detriment.

To date, there has been only one confirmed case of radiological terrorism, occurring in Moscow in November 1995 by radical Chechen separatists [5]. Although the decision to detonate the ^{137}Cs-dynamite device was abandoned, the capability of such radical groups to commit acts of radiological terrorism was revealed to be tangible and imminent. Although an RDD event has fortunately been eluded, the effects of the radiological accident in Goiânia, Brazil in 1987, involving a stolen medical device containing ^{137}Cs, highlight the shared detrimental consequences of such an event [5].

Radiological contamination can occur in the form of alpha, beta, or gamma radiation. A joint report by the Department of Energy (DOE) and Nuclear Regulatory Commission (NRC)

identified ^{241}Am, ^{60}Co, ^{137}Cs, and ^{192}Ir as radionuclides that pose the highest risk in the employment of an RDD [6]. Such nuclides are available industrially as medical diagnostic devices and in smoke detectors (^{241}Am), food irradiators (^{60}Co), and medical radiation therapy devices for cancer treatment (^{137}Cs, ^{192}Ir). In addition to these four nuclides, ^{131}I was investigated at the request of the Centers for Disease Control and Prevention, as it is commonly used in the medical diagnosis of thyroid cancer.

In light of such threats, a risk reduction strategy to mitigate the effects in the event of an RDD, including the development of emergency response plans and training for first responders, has become a priority concern for security-minded officials. An RDD event would leave its victims both externally and internally contaminated. Methods for assessing external contamination are better defined; however, methods for assaying internal contamination for mass populations are still deficient, especially in a case where substantial amounts of radioactive material have been inhaled or ingested, and internalized. Although whole-body counters are the preferred method of assessing contamination (as opposed to invasive bioassay procedures), their use in a triage scenario are obviated by their limited availability, and consequently their limited abilities in handling screening mass populations for internalized contamination. Whole-body counters are additionally too sensitive for the assaying required in an emergency triage scenario. Such limitations are the inherent motivation to investigate whether readily available handheld instruments could be used by first responders to assess the inhaled dose in a triage environment. Sodium-iodide detectors are available in most university and radiation safety laboratories in major metropolitan cities. These detectors are spectrometers, capable of producing a spectrum with photopeaks characteristics of a given radionuclide. They are robust compared to their semiconductor counterparts, and are comparatively inexpensive to purchase. Such detectors

consequently possess the characteristics of a portable detector that may be useful in a triage scenario in assessing the internalized contamination of RDD victims.

CHAPTER 2: BACKGROUND

The five radionuclides investigated were those said by the DOE/NRC study to be the nuclides of "greatest concern" in the deployment of an RDD [6]. Both organizations have published numerous reports on emergency response, medical, and triage procedures to be followed in the event of a deployment of an RDD. The Department of Homeland Security Working Group on RDD Preparedness has established a report on the medical treatment of radiological casualties [7]. In this study, *in-vitro* medical triage procedures were recommend for assessing internal dose by employing nasal swabs - which were said to represent 5% of the deposition in the lungs - in addition to cytogenetic biodosimetry and complete blood counts.

In-vivo methods are preferable to *in-vitro* methods, as they facilitate the rapid screening of triage patients without cumbersome and invasive procedures that are time consuming, limited in resources, and highly subject to error. In the latter category, whole body counters are the preferred method of assessing internal and external contamination. With over 300 people requiring assay, whole-body counters were successfully employed in assessing contamination in the ^{137}Cs accident in Goiânia, Brazil [8]. In this situation, a whole-body counter employing a 20-cm NaI(Tl) detector was installed at 2.05-m above the center of the room, and was collimated and shielded with 5-cm of lead. The detector was installed at a standoff distance due to the high level of contaminant activity in the subjects. Studies by Kramer *et al.* have investigated the use commercially available portal monitors (Constellation Technology Corporation P3 and Canberra Industries MiniSentry) for emergency response [9], in addition to assessing the feasibility of whole body counting by employing a commercially available portable instrument (ORTEC

Detective) involving a HPGe detector for automated nuclide identification and spectral analysis, and a compensated Geiger-Mueller tube to determine dose-rate [10].

A common obstacle in performing counts externally over the lungs includes compensating for varying chest wall thicknesses. Kramer *et al.* have studied the uncertainty introduced by varying chest thicknesses using the Lawrence Livermore National Laboratory torso phantom and a lung counting system employing an array of four large area germanium detectors [11]. In addition, Kramer *et al.* found that the variation in the chest wall thickness depth profile for male workers varies between 13% and 26%, contributing an uncertainty factor of approximately 1.07 [12]. In this study, they additionally postulate that the uncertainty factor for females is higher, around 1.2 of under- or over-estimation.

However, in addition to portal monitor applications, the use of NaI(Tl) detectors has been limited to the use of medical instrumentation such as gamma cameras and thyroid uptake systems [13], [14], [15]. These thyroid uptake systems employ NaI(Tl) detectors as spectrometers, but are attached via a lead collimator, typically 6-inches in length, and possess an automated data acquisition system. In order to validate the detector models to account for varying chest-wall thicknesses, Angistein *et al.* conducted simulations using acrylic slab phantoms and water phantoms with a thyroid uptake probe to compensate for varying chest-wall thicknesses. This study consequently determined that waste monitoring, gamma camera, and thyroid uptake systems were all capable of potential use following an RDD event [13].

Assaying inhaled contamination to determine the committed effective dose using handheld and readily available radiation detectors has been the focus of recent work at the Georgia Institute of Technology. Investigating the use of the aforementioned thyroid uptake systems have been conducted by Lorio [14], then later by Scarboro [15], for assaying the

committed effective dose due to inhaled contamination. Lorio's investigation using the Atomlab 950 Thyroid Uptake System additionally assessed the feasibility of using such a system to estimate dose in the event of a radiological attack and incorporated a validated Monte Carlo model to estimate counts due to lung uptake. Although Lorio's work was able to ascertain the use of this system following a radiological attack, Scarboro's work with the Capintec Captus 3000 thyroid uptake probe incorporated biokinetics to determine the time-dependent movement of inhaled radionuclide contaminants throughout the body, and also calculated the retention fraction by select organs over time. Scarboro's work additionally employed a set of decision levels for assaying inhaled dose for use in a first-responder triage scenario.

Although commercially available NaI(Tl) systems are available and have been proven effective for use in radiological emergency response, these detectors tend to be automated, costly, and lack the customizability due to their task-specific design. Portal monitors and whole body counters are too sensitive and are limited in availability for emergency triage scenarios. Medical assay equipment would only be available in hospitals in extremely limited quantities. Therefore, this study investigates the use of a standard 2x2-NaI(Tl) - a spectrometer in its bare form - in a triage field scenario to assess the committed effective dose of a patient due to inhaled contamination.

CHAPTER 3: METHODOLOGY

In order to assess the triage criteria for the inhalation and distribution of nuclides over a select period of time, computer modeling was employed since the inhalation and distribution of nuclides cannot feasibly be reproduced in the laboratory. Thus, a 2x2-NaI(Tl) detector was modeled for Monte Carlo simulation and validated via a series of benchmark measurements, as outlined in the depiction of the procedural overview in Figure 3.0.1. This detector model was validated by conducting experimental measurements using a polymethyl methacrylate (PMMA) slab phantom and six gamma-ray sources spanning a broad range of energies. Validation of the model resulted from the comparison of the experimental data from the slab phantoms to its simulated Monte Carlo model. Upon verification of the Monte Carlo detector model, six anthropomorphic phantoms - representative of various body types - were modeled with nuclides distributed throughout select organs for each of the five sources under consideration. After simulation, the data were incorporated with the time-dependent biokinetic modeling, from which the threshold count-rate values determined whether a subject is considered to have received a significant dose as per pre-established guidelines.

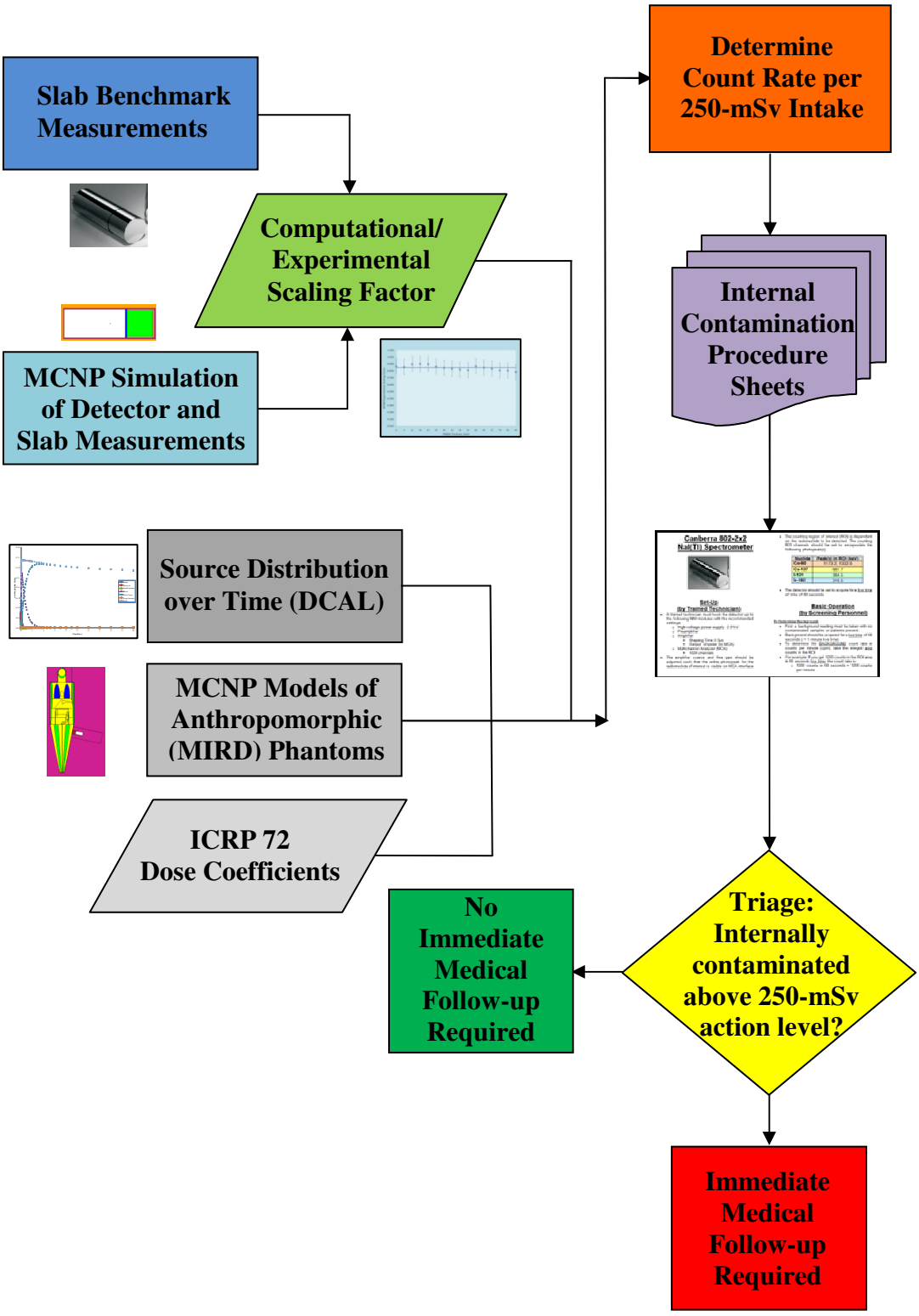

Figure 3.0.1 Procedure for Determining Inhalation Contamination Triage Levels Using a 2x2-NaI(Tl) Detector

3.1 Canberra 802-2x2 NaI(Tl) Detector

The 802-2x2 NaI(Tl) detector assembly is manufactured by Canberra Inc. [16] and contains a 2 Ø×2-inch thallium-activated sodium-iodide crystal manufactured by Saint Gobain Crystals [17]. The 802-2x2 NaI(Tl) detector is shown in Figure 3.1.1. The detector assembly includes the 2x2-inch NaI(Tl) crystal, a photomultiplier tube, and an internal magnetic/light shield, which are all hermetically sealed in an aluminum housing. The rear of the detector contains a 14-pin connector, capable of mounting a Canberra Model 2007P combination tube base and pre-amplifier. The detector works in conjunction with external high voltage and amplifier modules to produce an output spectrum via a multi-channel analyzer (MCA). The detector-module circuit for data acquisition with the sodium-iodide detector is shown in Figure 3.1.2 and depicts the mounted tube base and pre-amplifier assembly. Data were acquired using the Canberra 2007P combination tube base and preamplifier, which was powered by a Canberra 3002D High Voltage Power Supply at 0.91 kV and amplified by the Canberra 2022 module with coarse gain ×300, fine gain ×0.613, 0.5μs shaping time, and *UNIPOLAR* output to the MCA.

Figure 3.1.1 Canberra 802-2x2 NaI(Tl) Detector

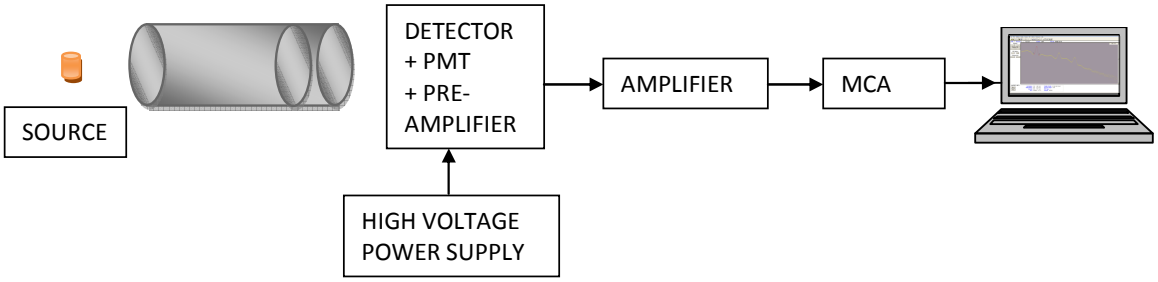

Figure 3.1.2 2x2 NaI(Tl) Detector Circuit Set-up

Canberra's Multiport II MCA, a module extra to the 802-2x2 detector assembly, is expandable to 16,384 channels and employs the Genie 2000 Gamma Acquisition and Analysis Software [18] as a user interface. A spectrum collected using this software is shown in Figure 3.1.3. In this experiment, 1024 MCA channels were used over the energy range investigated. Using more channels would subject the spectrometer to a higher counting error per acquisition channel. Using the MCA software and known gamma-ray radionuclide sources, the sodium-iodide detector was manually energy calibrated. It was best to select gamma-ray sources that cover a full range of energies to ensure accurate calibration. The MCA software is capable of storing customized energy calibration files, thus enabling the spectrometer to be calibrated with various gamma-ray sources and to be saved/recalled for later use by the same detector at specific module settings.

The MCA is also capable of selecting regions of interest (ROI) over a specified channel or energy range, and provides the number of counts in that region for a given live acquisition time from which a count rate can be easily calculated. For data saved in 1024 channels, the first two channels contain the real and live acquisition times and the remaining 1022 channels store data as counts per channel. These features are not unique to the Canberra Multiport II or 802-2x2 detector, but are representative of MCA software tools that are readily available to operate in conjunction with sodium-iodide detectors.

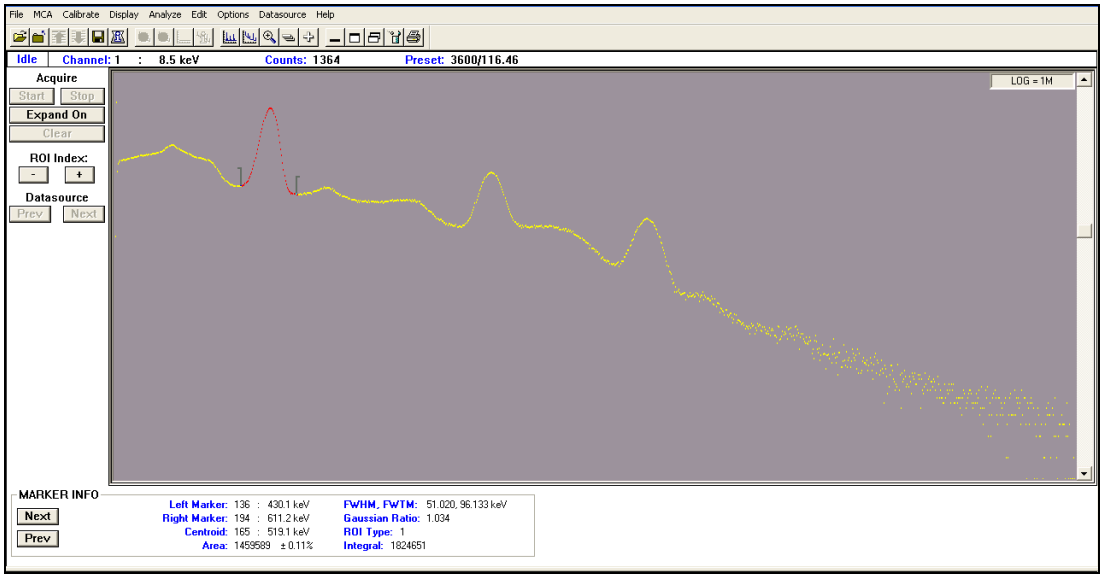

Figure 3.1.3 Canberra Genie 2000 Gamma Acquisition and Analysis Software User Interface

In this experiment, the MCA interface was calibrated using known checked sources to a gain of 3.18-keV per channel commencing from the first channel containing energy information (channel 3) to channel 1024. Thus, energy information is stored in 1022 channels and was fit linearly to known photopeaks to yield the energy calibration given Figure 3.1.4.

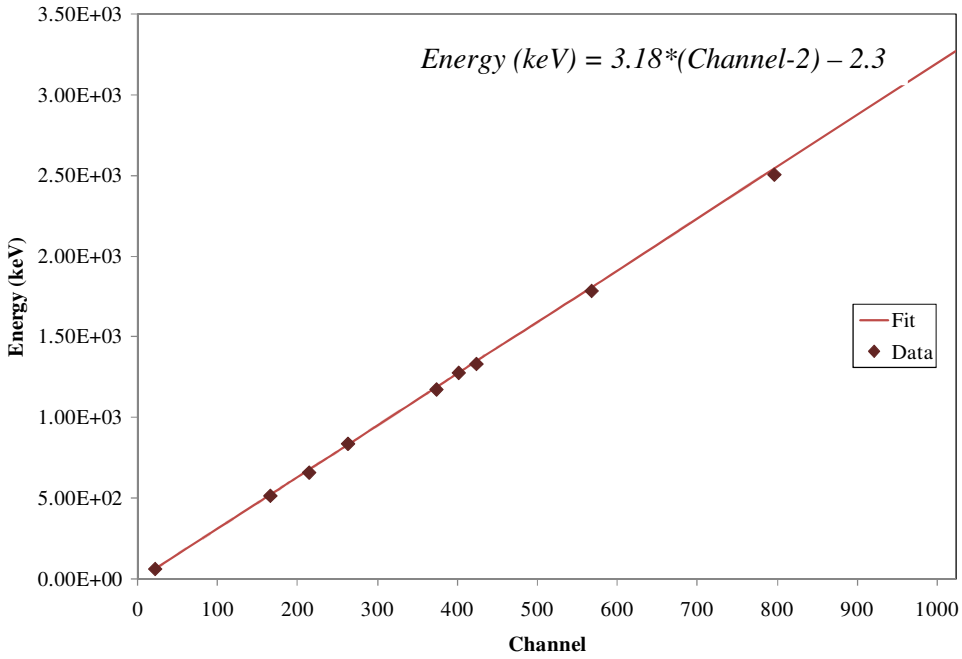

Figure 3.1.4 Energy Calibration Curve for 2x2 Na(Tl) Detector

Based on the source calibration data, the ROIs were selected to encompass the photopeaks of the radionuclides studied. The MCA is able to store ROIs, but does not consistently or accurately automatically select the peak ROIs, thus necessitating manual assignment over the peak area. Although the MCA is capable of manually assigning and storing ROIs, this must be done for specific detector and module settings for a given energy calibration. This therefore necessitates that the detector be operated at the settings at which it was energy calibrated. The ROIs can thence be assigned as the user requires, making the detector system very customizable, and capable of saving/recalling data for analysis *ex-post facto*.

3.2 Polymethyl Methacrylate Slab Phantom Measurements

The computational model of the 802-2X2 NaI(Tl) detector was validated via a series of benchmark measurements using a PMMA slab phantom. As depicted in Figure 3.2.1, the slab phantom consisted of varying thicknesses of PMMA, followed by a source holder to affix the radionuclide source, and Virtual Water^{TM} [19] behind the source. For all benchmark measurements, a 100-mm thickness of Virtual Water was maintained behind the source holder to simulate the gamma-ray backscattering that would result from human tissue. The source holder was constructed from a 6mm-thick sheet of PMMA bored with a cylindrical hole to center and encapsulate the radionuclide source, preventing it from shifting during data acquisition and maintaining the source position at the center of the detector face.

The six sources investigated with the PMMA slab include ^{241}Am, ^{133}Ba, ^{60}Co, ^{137}Cs, ^{54}Mn, and ^{22}Na. These nuclides were selected for their broad range of gamma energies interacting with the detector. Additionally, ^{241}Am, ^{60}Co, and ^{137}Cs, have been identified as materials of greatest concern in the employment of an RDD [6]. The energies and intensities for the primary photopeaks under analysis for the nuclides employed in the PMMA benchmark measurements were obtained from the Oak Ridge National Laboratory program, RadToolbox [20], and are summarized in Table 3.2.1.

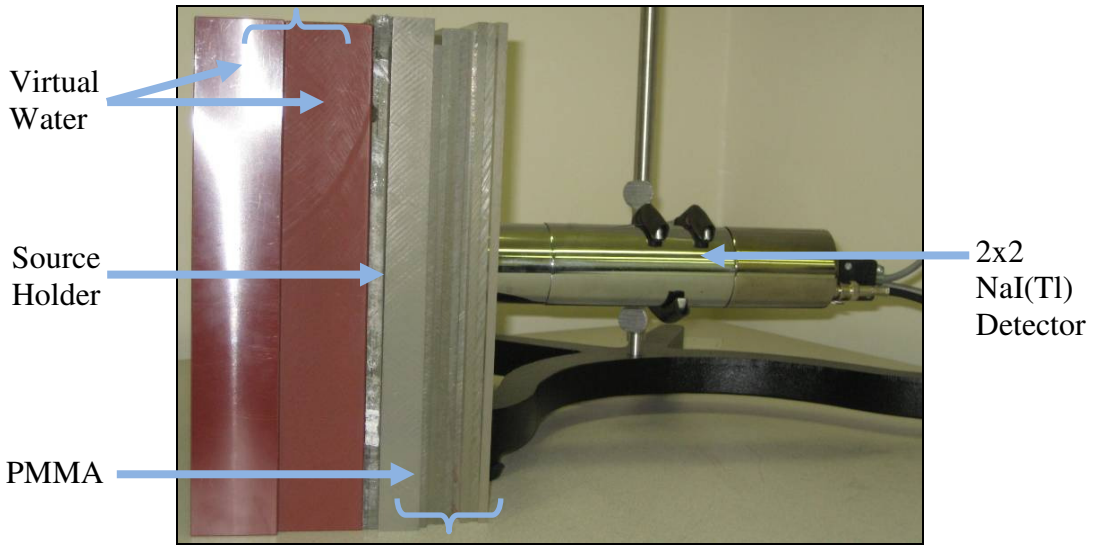

Figure 3.2.1 PMMA Slab Phantom Set-up

Table 3.2.1 Photopeak Gamma Energies Investigated for Slab Phantom Radionuclide Sources

Nuclide	Peak Energy (keV)	Intensity
^{241}Am	59.5	0.357
^{133}Ba	276.397	0.071
	302.851	0.184
	356.005	0.622
^{60}Co	1173.2	0.998
	1332.5	0.999
^{137}Cs	661.7	0.898
^{54}Mn	834.8	0.999
^{22}Na	511.0 *(Annihilation Peak)*	1.798
	1274.5	0.999

Varying thicknesses of PMMA were placed in front of the source holder, ranging in 6-mm increments from 0-mm to 90-mm between the source and detector (with the exception of ^{241}Am and ^{133}Ba measurements, for which data were taken up to only 60-mm in thickness). PMMA was chosen for its tissue-like attenuation behavior with gamma-rays; thus, varying thicknesses of PMMA were used to mimic varying chest-wall thicknesses in humans. Increasing the PMMA thickness, and thus the source-to-detector distance, adds an additional inverse of distance-squared factor to the attenuation behavior of PMMA on the incident gamma-rays.

The acquisition time was determined based on the number of counts accumulated under the ROI encompassing the selected photopeaks. This was set to acquire until at least 10,000 gross counts (prior to background subtraction) were accumulated – corresponding to approximately 1% counting error under the peak. The ROIs for the investigated nuclides, listed in Table 3.2.1, were selected to encompass the peak(s) under investigation and were based on the detector response to bare sources (without the PMMA phantom). These ROIs were determined during energy calibration with the bare sources and were applied as the integral counting regions for the PMMA phantoms. The ROIs over which the counts were integrated for each radionuclide were selected to capture the nuclide's primary photopeaks. For example, if a radionuclide emitted three distinct, high-intensity gamma-ray lines, then three separate ROIs were applied, each encompassing a corresponding photopeak. In practice, the endpoints of the ROIs were set manually, such that they encompassed the edges of the photopeaks to be counted. A sample ROI selection for both the experimental and MCNP simulated peaks for the 0.662-MeV peak for ^{137}Cs is shown in Figure 3.2.2.

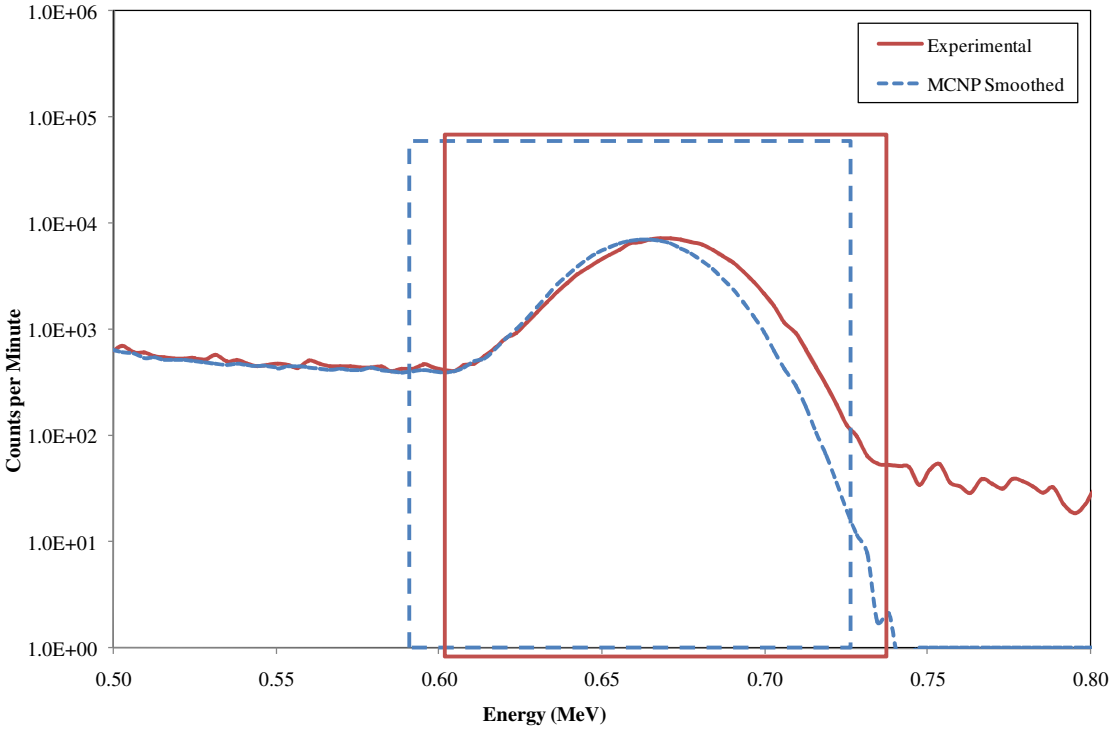

Figure 3.2.2 Sample Region of Interest Comparison for ^{137}Cs for Experimental Slab Phantom Data and MCNP Simulation Model

As listed in Table 3.2.1, the ROIs for ^{133}Ba and ^{60}Co consisted of the amalgamation of multiple adjacent photopeaks. These peaks were merged into a single ROI due to their close proximity to each other, thus preserving count rates, as well as reducing the error required to separate the peaks due to variable detector resolution. The remaining nuclides' ROIs were singly selected peak regions, since these characteristic photopeaks were relatively isolated in energy vis-à-vis other emissions and were high intensity emissions. The selection of the ROI was manually conducted, as the boundaries encompassing the photopeaks selected were specific to this detector. Other 2x2 NaI(Tl) detectors will differ in detector resolution and will thus require that the ROIs be manually selected to encompass the photopeaks. In addition, the peak area was determined by subtracting the continuum under the peak of the ROI caused by a superimposed

continuum, using a linear interpolation between the peak boundaries to estimate the continuum counts to be subtracted. This approach is well known and outlined by Knoll [21], and yields sufficient accuracy for this data analysis.

Summation peak events were also taken into consideration when acquiring data using the PMMA slab phantoms. When two or more gamma-rays are coincidently incident on the detector, a count is recorded in the pulse-height spectrum at a value equal to the sum of the two coincident gamma-rays [21]. This is common for a nuclide that emits multiple gammas during its decay. These events are not a separate gamma-ray in a nuclide's decay scheme, but the coincident detection of two (or more) true gamma-rays. If enough of these events occur, then a sum coincidence peak is observed in the spectrum centered about an energy equal to the sum of the two incident gamma-rays. Summations can occur for two full energy gamma-rays or between Compton scattered gamma-rays coincident with a full energy gamma-ray. This is purely a property of the incident event rate, detector size and response, and does not occur in computational modeling. Thus, for each single count in the sum coincidence peak, these counts must be redistributed back to the contributing peaks to attempt to preserve the true number of integral counts in the ROI.

3.3 MCNP Detector Model Validation

Benchmark measurements were used to validate the computational detector model by comparing the experimental measurements taken using the PMMA slab phantom for the six gamma-ray sources with its simulated Monte Carlo model. The detector was modeled using Los Alamos N-Particle Transport Code MCNP-5 [1]. The detector model response was simulated at each incremental thickness of PMMA, thus replicating the slab phantom benchmark experiments. Consequently, the detector response was determined for each of the six isotopes employed in the benchmark measurements to ensure that the detector model was validated over a broad range of gamma-ray energies. The integrated pulse-height region for each ROI in the benchmark measurements were compared with the respective Monte Carlo slab phantom model, from which a detector response efficiency (scaling) factor was calculated for each nuclide over all PMMA thicknesses. Consequently, validation of the computational detector model is essential in reproducing an accurate detector response.

3.4 Anthropomorphic MIRD Phantoms and Biokinetics

The Medical Internal Radiation Dose (MIRD)-based anthropomorphic phantoms [2] and a child phantom (constructed using BodyBuilder [22]) were employed as the computational human models into which radionuclides were distributed to represent inhaled contamination. The MIRD phantoms are based on the Reference Male and Female body types, and are based on the mathematical phantoms initially developed at Oak Ridge National Laboratory [2]. The MCNP-coded versions of the Reference Male and Female used in this work were originally created at Pacific Northwest National Laboratory, based on the MIRD phantoms [23] and the ICRP 23 recommendations [24]. The development of the adipose phantoms by Simpkins and Hertel was an extension of these models [25], and resulted in three adult phantoms: Adipose Male, Adipose Female, and Post-Menopausal Adipose Female. These phantoms have been modified recently at the Georgia Institute of Technology by Burns, with the addition of a 2-mm layer of skin tissue to the phantoms [26]. Thus, a total of six phantoms - five adult (two reference, three adipose) and an androgynous 10-year old child phantom - were simulated.

The count-rates due to inhaled radionuclides distributed biokinetically in the body were simulated using MCNP anthropomorphic phantom models. The MCNP detector model, after validation by the slab phantom benchmark experiment, was used to simulate the detector response at various locations on the surface of the anthropomorphic phantoms. The validated detector model was placed in various locations about the phantom, with an objective of identifying which detector location would yield optimal counts per unit inhaled dose of nuclide.

Four locations were selected for study: anterior neck, anterior and posterior right upper torso, and lateral left thigh. All four locations were employed using the Reference Male

phantom, though the anterior upper-right torso position was omitted from the remainder of the phantoms due to adipose/breast tissue attenuation at this location with the Reference Female, Adipose Male, Adipose Female and Post-Menopausal Adipose Female phantoms. With a validated detector model strategically placed about these phantoms, the detector response due to inhaled contamination was derived.

Each of the phantoms was simulated with inhaled contamination for five radionuclides, listed in Table 3.4.1. These sources (^{241}Am, ^{60}Co, ^{137}Cs, ^{131}I, ^{192}Ir) were selected as the nuclides of "greatest concern" in the employment of an RDD [6]. With a computational ROI analysis similar to that of the aforementioned slab phantom, the energies and intensities for primary photopeaks under analysis for the nuclides employed in the anthropomorphic phantoms were RadToolbox [20] and are summarized in Table 3.4.1.

Table 3.4.1 Photopeak Gamma Energies Investigated for Anthropomorphic Phantom Radionuclide Sources

Nuclide	Peak Energy (keV)	Intensity
^{241}Am	59.537	0.357
^{60}Co	1173.237	0.998
	1332.501	0.999
^{137}Cs	661.657	0.898
^{131}I	364.480	0.812
^{192}Ir	316.500	0.829

The radioactive source distribution in the body as a function of post-inhalation time was determined using the Dose and Risk Calculation software (DCAL) [4], a code developed at Oak Ridge National Laboratory by Eckerman *et al.* The DCAL software implements the ICRP Publication 66 respiratory biokinetics to determine the retention factors for a given radionuclide

inhalation class in the body as a function of time [27]. As will be discussed the next section, the data from DCAL can be used in conjunction with the MCNP count-rates from the contaminated MIRD phantoms to determine the detector count-rate due to inhaled contamination for each radionuclide after a given post-inhalation time.

3.5 Triage Clinical Decision Levels and Protocols

Simulations were performed for the anthropomorphic phantoms with appropriately distributed radionuclide contamination as a function of bodily retention per unit time. The count-rate per unit activity inhaled was determined to ascertain the count-rate corresponding to the action/screening-level dose. These data will be used as criteria for determining whether further medical attention is required. The threshold action screening level for triage activity used in this phase of the work was set to a committed effective dose of 250-mSv [3].

From the four detector positions modeled, the detector location yielding the highest count-rate per 250-mSv intake for each nuclide was selected for screening. A procedure sheet was developed for each phantom-radionuclide pairing to instruct first responders in use of the detector for triaging, as well as how to determine count-rate decision levels for various time periods following the initial inhalation during the radiological event.

CHAPTER 4: COMPUTATIONAL MODELS

The basis of assessing inhaled contamination relies on computer simulation of the detector response for the inhaled contamination distributed in the body as a function of time. All photon transport calculations were simulated using MCNP-5 [1]. A summary of the computational models to simulate the detector response for both the PMMA slab phantoms and the MIRD phantoms is presented in this chapter.

4.1 2x2 NaI(Tl) Detector Model

In order to ensure an accurate detector response, the 802-2x2 NaI(Tl) detector was modeled in detail. A pulse-height tally (MCNP F8) was performed over the active region of the detector crystal to determine the pulse-height spectrum. Since actual measurements were accumulated as 1022-channel pulse-height spectra, the MCNP pulse-height spectra were similarly binned and tallied into 1022 channels spanning a total energy range of 3.248-MeV in 3.18-keV increments per channel (refer to §3.1). The dimensions and physical characteristics of the detector are outlined in the sample MCNP input file in Appendix A and the detector material properties are presented in Table 4.1.1. A VisEd [28] rendering of the detector model is given in Figure 4.1.1.

Table 4.1.1 Detector Material Specifications

Detector Component	Weight Percent Composition	Thickness (cm)	Density (g/cm^3)
Detector casing [16]	100.00% Al	0.20	2.94
Aluminum-oxide powder coating [29]	52.93% Al 47.07% O	0.16	0.55
Compressed foam [30],[31]	14.37% H 85.63% C	0.19	0.93
Saint Gobain NaI(Tl) Crystal [17]	15.33% Na 84.67% I	5.08×5.08	3.667
Photomultiplier Tube Low Density Glass [32], [31]	53.26% O 46.74% Si	0.30	0.94

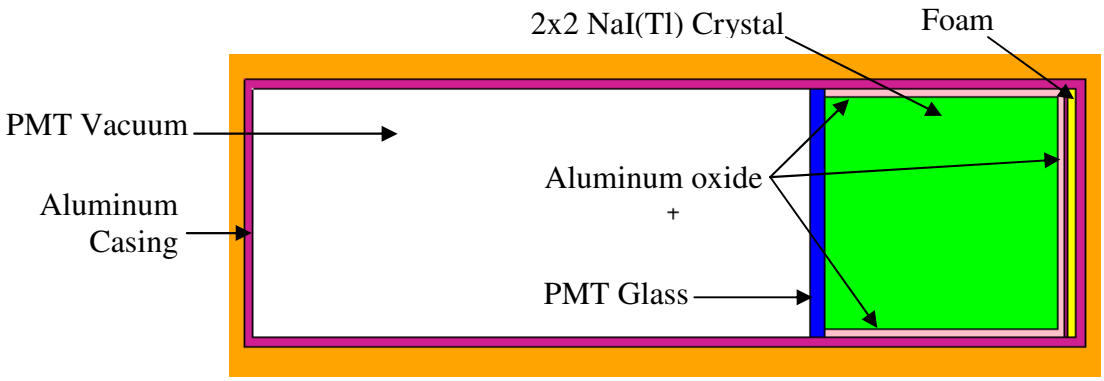

Figure 4.1.1 VisEd Representation of Canberra Model 802-2x2 NaI(Tl) Detector

4.2 Slab Phantom Model

An MCNP model of the PMMA slab phantom for each source was constructed. A point source was defined to simulate each of the gamma-ray sources, and a pulse-height tally was performed over the active volume of the detector crystal to simulate the pulse height spectra for each radionuclide. A separate slab phantom model was constructed for each PMMA thickness – from 0-mm to 90-mm (with the aforementioned exception of ^{241}Am and ^{133}Ba, taken to 60-mm). The material characteristics of the slab phantom are summarized in Table 4.2.1 and a sample detector and slab MCNP input file is given in Appendix A.

Table 4.2.1 Slab Phantom Material Specifications

Slab Phantom Component	Weight Percent Composition	Thickness (cm)	Density (g/cm^3)
PMMA Slabs & Source Holder [14]	8.06% H 59.99% C 31.95% O	0.6 (increments)	1.19
Virtual Water [19]	0.64% H 63.99% C 2.53% N 25.14% O 0.39% Cl 7.31% Ca	10	1.03
Polyester Source [15]	8.06% H 60.02% C 31.92% O	0.4 Ø	1.00
Surrounding Air [32]	75.58% N 23.14% O 1.28% Ar	n/a	0.001293

A VisEd [28] representation of the slab model with the detector is depicted in Figures 4.2.1 and 4.2.2, while the source collision interactions are portrayed in Figure 4.2.3, where the dots represent collisions by the source particles.

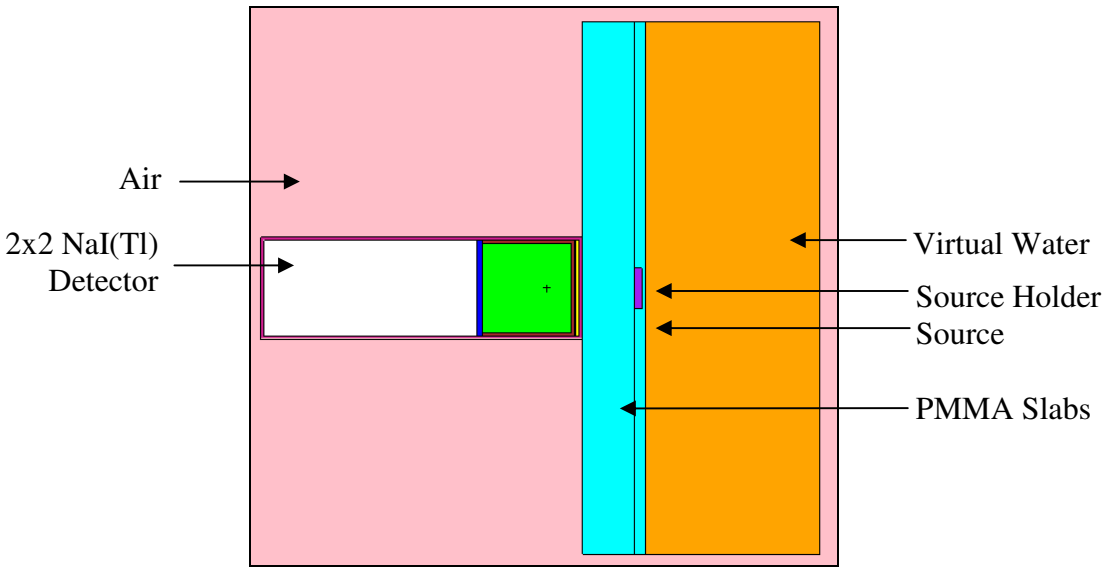

Figure 4.2.1 VisEd Representation of PMMA Slab Phantom Model

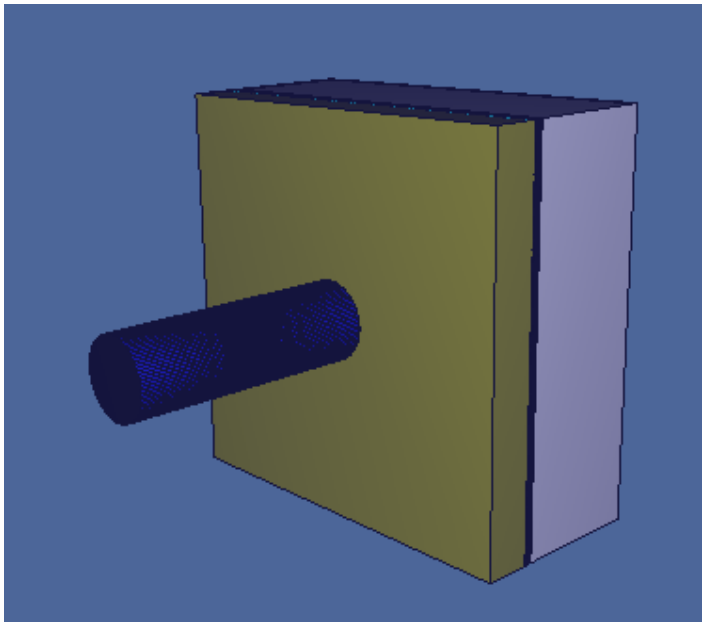

Figure 4.2.2 3-D VisEd Representation of PMMA Slab Phantom Model

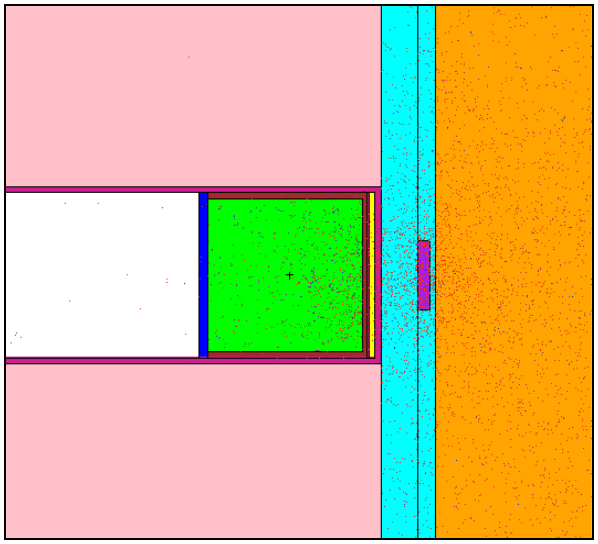

Figure 4.2.3 VisEd Representation of Source Particle Collision Interactions with Detector

The scaling factors for all PMMA thicknesses were determined for each radionuclide. The scaling factors are the ratios of the simulated MCNP count rates with the detector counts in the relevant peak ROIs of the benchmark measurements. The purpose of simulating multiple PMMA thicknesses for each nuclide was to verify that the detector scaling factor was relatively constant regardless of PMMA thicknesses; that is, it did not vary with thickness. This consequently validates the detector model for each radionuclide regardless of source-detector geometry. The average ratio for each radionuclide was used as a detector-reading scaling factor applicable to other source-detector geometries.

The energies and intensities for the nuclides employed in the source definitions in the PMMA simulations were obtained from RadToolbox [20] and are summarized in Table 4.2.1.

Table 4.2.1 Slab Phantom Source Gamma Energy-Intensity Data

^{241}Am		^{133}Ba		^{60}Co		^{22}Na	
Energy (keV)	**Emission Intensity**	**Energy (keV)**	**Emission Intensity**	**Energy (keV)**	**Emission Intensity**	**Energy (keV)**	**Emission Intensity**
13.760	0.025	30.625	0.341	1173.237	0.9985	511	1.798
13.944	0.219	30.973	0.631	1332.501	0.9998	1274.54	0.999
16.835	0.058	34.987	0.122				
17.061	0.022	80.997	0.338	^{137}Cs		^{54}Mn	
17.750	0.188	276.397	0.071	**Energy (keV)**	**Emission Intensity**	**Energy (keV)**	**Emission Intensity**
17.992	0.020	302.851	0.184	661.657	0.898	834.848	0.99976
20.785	0.046	356.005	0.622				
26.345	0.024	383.851	0.089				
59.537	0.357	30.625	0.341				

Since the MCNP tallies are normalized to emissions per source particle, the tally output was multiplied by the exact source activity of the sources employed in the benchmark measurements and branching ratios in order to replicate laboratory measurements. The branching ratio is the number of particles emitted per decay, where four isotopes (^{241}Am, ^{133}Ba, ^{60}Co, ^{22}Na) emit multiple gamma rays for each particle decay. Therefore, the sum of the branching ratios for each of the radionuclides must be considered. The assay activities of the sources employed in the benchmark measurements and the summed branching ratios for the ROIs are summarized in Table 4.2.2.

Table 4.2.2 Source Assay Activity

Isotope	Assay Date	Initial Activity (μCi)	Half-Life (y)	Experiment Activity (μCi)	Measurement Date (MM/DD/YY)	Branching Ratio
^{241}Am	12/09/05	7.50	432	7.48	12/10/07	0.9592
^{133}Ba	12/09/05	5.20	10.7	6.53	01/11/08	2.3966
^{60}Co	12/09/05	5.10	5.27	4.02	09/29/07	0.8528
^{137}Cs	12/09/05	4.90	30.0	4.70	09/30/07	1.9988
^{54}Mn	12/09/05	5.00	0.86	1.15	10/03/07	0.9997
^{22}Na	12/09/05	5.00	2.60	3.09	09/29/07	2.7974

In the unsmoothed MCNP pulse-height tally, all photoelectric interactions result in a delta function at the photon energy rather than a resolution-broadened photopeak. Thus, the Gaussian Energy Broadening function [1] in MCNP was used to simulate the detector resolution, based on the full-width-at-half-maximum (FWHM) data, though exact resolution matching is very time consuming. In principle, the use of the unsmoothed counts at the full gamma-ray energy would also accomplish the same purpose, as would smoothing to the monoenergetic output using alternative software. The parameters required for the GEB function (*a, b,* and *c*) were calculated based on the measured detector response, and iteratively fit [33] to Equation 4.2.1 to obtain the GEB parameters.

$$FWHM = a + b\sqrt{E + cE^2} \qquad \text{[Equation 4.2.1]}$$

In this expression,

E = Energy (MeV)

$FWHM$ =full-width-at-half-maximum value of photopeak (MeV)

The detector resolution calculated from the benchmark measurements for each of the six radionuclides is plot in Figure 4.2.3 with the computational resolution using the GEB fit parameters. The parameters and usage of the GEB function may be found in the example MCNP input file in Appendix A, as well as in Figure 4.2.3. According to the Canberra 802-2x2 NaI(Tl) detector specifications, the crystal has a peak resolution of 8.5% for the 0.662-MeV ^{137}Cs peak [16], where the detector employed in the benchmark data collection had a peak resolution of 7.46%, and the corresponding GEB fit had resolution of 7.31%.

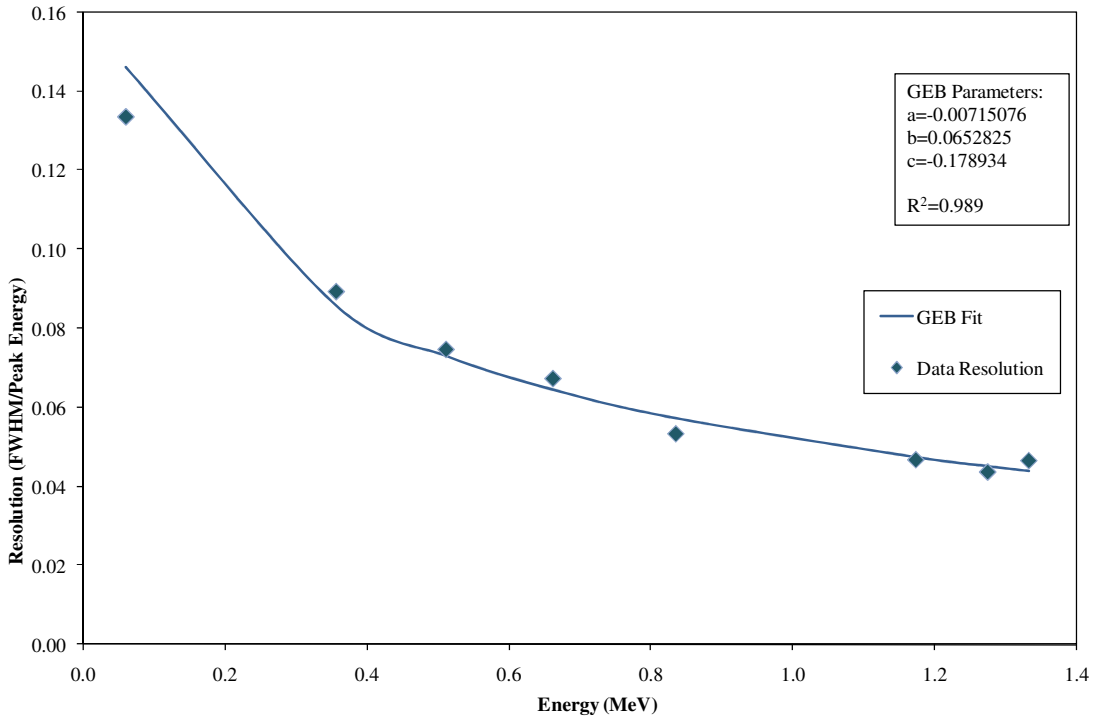

Figure 4.2.3 Detector Resolution and Simulated Resolution using GEB Fit Parameters

To illustrate the effect of the GEB smoothing function, a measured spectrum, an unsmoothed (raw) MCNP tally, and a GEB smoothed MCNP tally are compared in Figure 4.2.4 for ^{137}Cs.

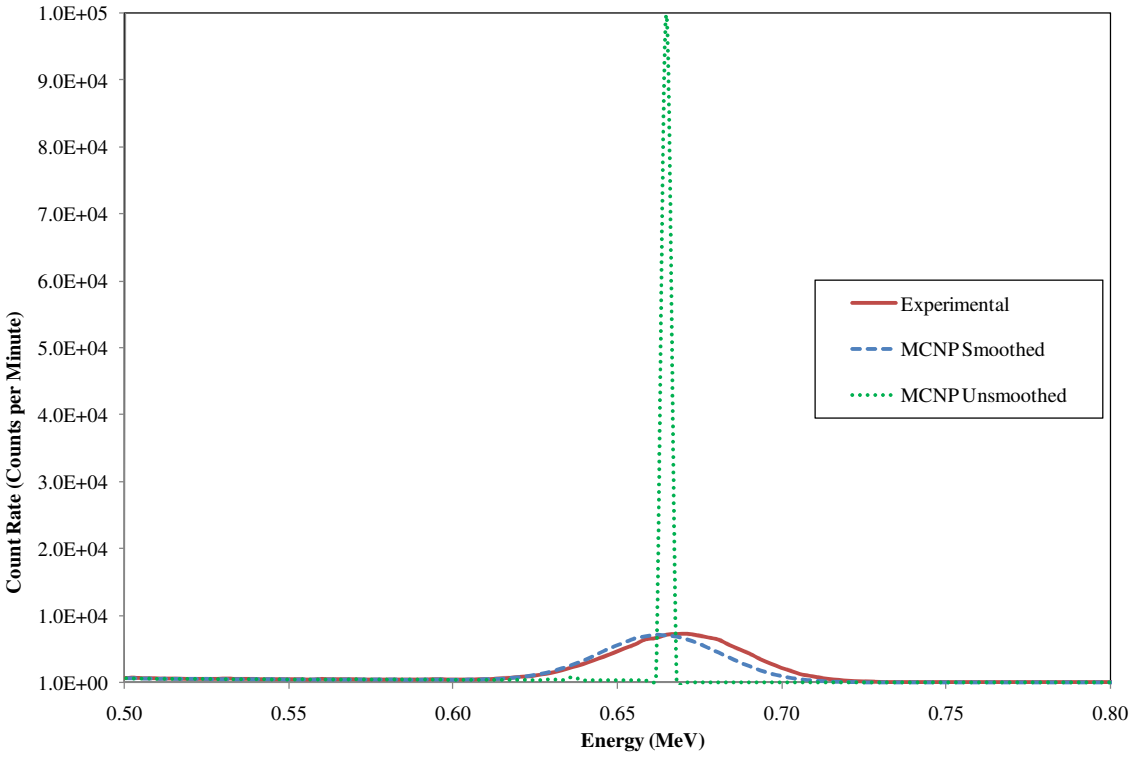

Figure 4.2.4 Comparison of Measured Spectrum for ^{137}Cs with 30-mm PMMA with Corresponding Smoothed and Unsmoothed MCNP Simulated Spectra

As outlined in detail in §3.2, the corresponding integral count rates for the primary photopeaks for each nuclide used in the benchmark measurements were similarly used for the computational simulations. Yet, unlike the experimental data, computational data did not simulate sum-coincidence effects, as shown in Figure 4.2.5. Since summation effects are a property of the detector and incident count-rate, it is not necessary to simulate this effect computationally. In each case, the count-rate due to photoelectric depositions can be determined, whether they are manifested in the ROI photopeak or summation peak. The ROIs employed to determine the integral count rates from the MCNP PMMA slab phantoms are summarized for each nuclide in Table 4.2.3.

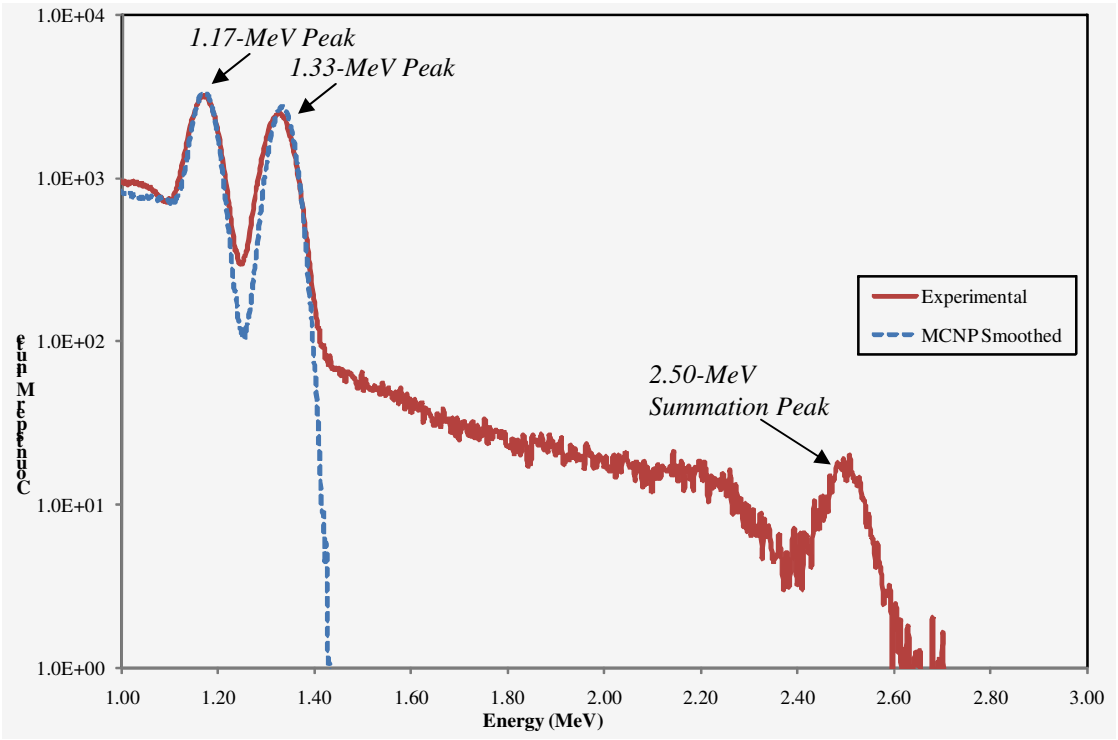

Figure 4.2.5 Comparison of Measured Spectrum for ^{60}Co with Summation Peak for 30-mm PMMA with Corresponding Smoothed MCNP Simulated Spectrum

Table 4.2.3 MCNP Slab Phantom Counting Regions of Interest

Nuclide	Peak Energy (keV)	MCNP Slab Phantom ROI (keV)
^{241}Am	59.5	[35.8, 77.1]
^{133}Ba	276.4, 356.0	[239.1, 401.1]
^{60}Co	1173.2, 1332.5	[1099.8, 1414.3]
^{137}Cs	661.7	[582.1, 725.0]
^{54}Mn	834.8	[772.7, 896.6]
^{22}Na	511.0	[451.9, 563.1]
	1274.5	[1179.2, 1376.2]

The results of the slab phantom benchmark measurements, in combination with the computational models of the slab phantoms, are given as energy-dependent scaling factors. These results are discussed in §5.1.

4.3 MIRD Phantom Models

Upon verification of the detector model using the slab phantoms, Monte Carlo methods were employed to simulate the detector response of the 802-2x2 NaI(Tl) detector to inhaled radionuclide contamination. Six anthropomorphic phantoms were contaminated with five radionuclides identified likely to be employed in an RDD. To determine the position for obtaining an optimal count, the detector was placed at four positions of the body. An MCNP model of each of the anthropomorphic phantoms was constructed with unit sources defined in key organs to simulate inhaled contamination. Like the slab phantom computational model, a pulse-height tally (F8) was performed over the active volume of the detector crystal to simulate the pulse-height spectra for each radionuclide and the same GEB function was used to mimic detector resolution properties. A sample MCNP input file of anthropomorphic phantom model with the detector placed at each of the four locations is given in Appendix B.

4.3.1 Anthropomorphic Phantom Characteristics

These phantoms can be characterized according to their height, body mass, and the adipose tissue mass. The Body Mass Index (BMI) is a useful metric in assessing human body sizes for adults over age 17 [34]. The BMI is calculated by dividing the mass (kg) by the square of the height (m), where a larger BMI is indicative of obesity. The characteristics of each human phantom are given in Table 4.3.1 [25].

Table 4.3.1.1 Anthropomorphic Phantom Physical Characteristics

Phantom	Height (cm)	Mass (kg)	Adipose Tissue Mass (kg)	BMI
Reference Male	179	73.1	11	23
Reference Female	168	56.5	15	20
Adipose Male	179	93.7	22	30
Adipose Female	168	73.9	15	26
Post-Menopausal Adipose Female	168	85.9	27	30
10-year Androgynous Child	140	32.7	n/a	n/a

4.3.2 Anthropomorphic Phantom Source Contaminant Distribution

A uniformly distributed source for each of the five isotopes was generated in key organs to which the radionuclides would migrate. The organs selected were based on the ICRP model for inhaled dose [4]. The compartments containing sources for each of the five radionuclides are summarized in Table 4.3.2.1. Organs also varied slightly between male and female phantoms, where male left and right testes were replaced in the female with left and right ovaries, in addition to tissue added at the breasts. In comparison to the reference phantoms, the three adipose phantoms included additional subcutaneous adipose tissue, as well as adipose tissue additions to the abdomen and thighs.

The energies and intensities for the nuclides employed in the source definitions in the anthropomorphic phantoms were obtained from RadToolbox [20] and are summarized in Table 4.3.3.2.

Table 4.3.2.1 Compartments of Interest for each Anthropomorphic Contaminant Nuclide

Nuclide / *Compartments of Interest*	^{241}Am	^{60}Co	^{137}Cs	^{131}I	^{192}Ir
Blood	X	X	X	X	X
Body Tissue	X	X	X	X	X
Cortical Bone	X				
Kidneys	X				X
Liver	X	X			X
Lower Large Intestines Contents	X	X	X	X	X
Lungs	X	X	X	X	X
Red Marrow	X				
Small Intestines Contents	X	X	X	X	X
Spleen					X
Stomach Contents	X	X	X	X	X
Testes/Ovaries	X				
Trabecular Bone	X				
Thyroid			X		
Upper Large Intestine Contents	X	X	X	X	X
Urinary Bladder Contents	X	X	X	X	X

Table 4.3.3.2 Anthropomorphic Phantom Source Gamma Energy-Intensity Data

^{241}Am		^{192}Ir		^{131}I	
Energy (keV)	**Emission Intensity**	**Energy (keV)**	**Emission Intensity**	**Energy (keV)**	**Emission Intensity**
13.760	0.025	9.442	0.015	29.458	0.014
13.944	0.219	11.071	0.013	29.779	0.026
16.835	0.058	62.999	0.022	80.183	0.026
17.061	0.022	65.122	0.027	284.298	0.061
17.505	0.013	66.831	0.046	364.480	0.812
17.750	0.188	61.486	0.013	636.973	0.0723
17.992	0.020	205.791	0.033	722.893	0.018
20.785	0.046	295.951	0.289	^{60}Co	
26.345	0.024	308.447	0.297		
59.537	0.357	316.500	0.829	**Energy (keV)**	**Emission Intensity**
^{137}Cs		468.060	0.478		
		484.565	0.031	1173.237	0.9985
Energy (keV)	**Emission Intensity**	588.573	0.045		
		604.391	0.082	1332.501	0.9998
661.657	0.898	612.451	0.053		

In the MCNP model, a source-contribution tally modifier (SCX) [1] was implemented in conjunction with the pulse-height tally to determine the source organ contribution for each source particle that reaches the detector. This value yields the detection efficiency for a unit volume source in each organ. The output of the SCX-modified pulse height tally is given as a count-rate per becquerel (Bq). The ROIs selected to give the tally count-rate are listed in Table 4.3.3.3. Three of the radionuclides correspond with the slab phantom measurements and models, but the methodology for ROI selection (encompassing the photopeak) was common to all five radionuclides.

Table 4.3.3.3 MCNP Anthropomorphic Phantom Counting Regions of Interest

Nuclide	MCNP Anthropomorphic Phantom ROI (keV)
^{241}Am	[35.8, 77.1]
^{60}Co	[1099.8, 1414.3]
^{137}Cs	[578.9, 721.8]
^{131}I	[315.3, 432.8]
^{192}Ir	[239.1, 394.7]

4.3.3 Detector Placement on Anthropomorphic Phantoms

The count-rates at four detector locations were simulated and the optimal count-rate location for each of the five radionuclides was chosen for use in triaging. The torso locations over the right lung locations were selected because they resulted in the highest count-rate per Bq inhaled. Additionally, the three-lobed right lung is larger than the two-lobed left lung. Posterior and anterior locations were selected due to attenuation affects of breast tissue and fat. The neck was selected since ^{131}I is a well known thyroid-seeker. Finally, the thigh location was selected, as it represents a large and fleshy muscular region where body tissue seeking nuclides may migrate. A VisEd [28] representation of these detector placement locations is displayed in Figure 4.3.3.1.

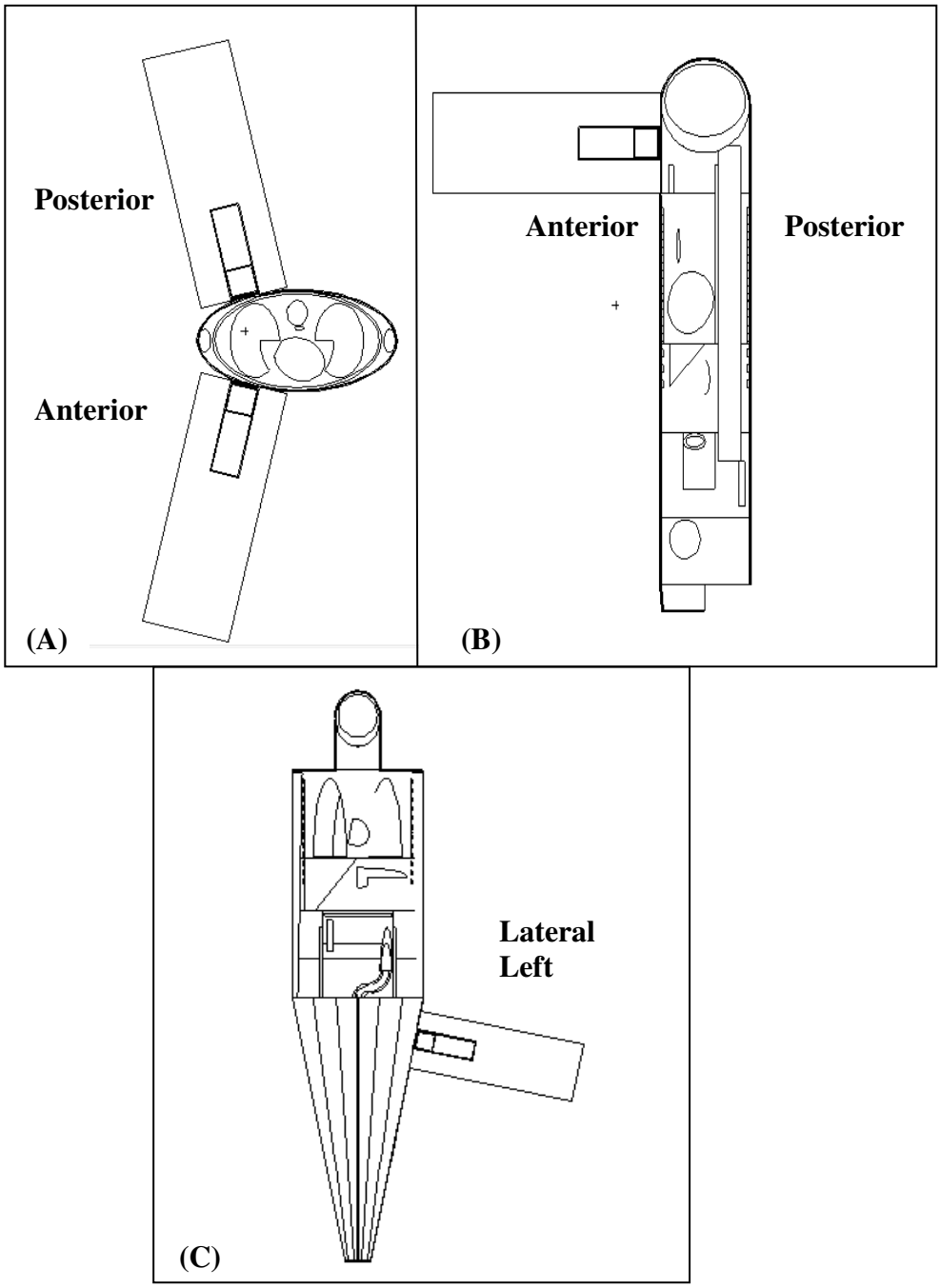

Figure 4.3.3.1 Detector Placement Locations on Anthropomorphic Phantom: (A) Anterior and Posterior Right Upper Torso; (B) Anterior Neck; and (C) Lateral Left Thigh

4.4 DCAL Biokinetic Modeling

Biokinetic modeling is employed to determine the biological movement of a radionuclide through the human body as a function of time. Certain nuclides characteristically accumulate in specific organs based on their metabolism in the body. The DCAL [4] software was used to determine the accumulated amount of radionuclide present in an organ after a given time – thus tracking the biological/metabolic and radiological decay effects. The activity calculation module, ACTACAL, is a component in the DCAL package that calculates the time-dependent activity in various body compartments for a given parent radionuclide. The DCAL software libraries include the ICRP-66 respiratory tract kinetics [27], ICRP-30 gastrointestinal (GI) model [35], ICRP-67 urinary bladder voiding model [36], and ICRP-68 GI absorption fractions and system biokinetics [37]. Radionuclide data, including energies and intensities from the ICRP-30 publication data, are employed in DCAL [35].

For each of the five radionuclides under investigation (^{241}Am, ^{60}Co, ^{137}Cs, ^{131}I, ^{192}Ir), DCAL was executing using ICRP default inhalation classes [38]. For each nuclide run with DCAL, inhalation from an environmental source (vis-à-vis an occupational source) was specified as the intake pathway. A default of 1-micrometer was used as the particle's activity mean aerodynamic diameter (AMAD) [4]. The lung absorption type (slow [S], moderate [M], fast [F]) corresponded to the speed with which the particulate nuclide is absorbed in the lungs [4]. The inhalation classes corresponded to ICRP 72 recommended defaults [38]. The default lung absorption type for ^{137}Cs and ^{131}I is fast, whereas ^{60}Co and ^{241}Am have a moderate speed uptake. Since a default lung absorption type was not specified for ^{192}Ir, a moderate uptake was assumed [15]. A summary of the default inhalation classes is displayed in Table 4.4.1. Additionally,

summarized in this table are the Environmental Inhalation Dose Coefficients for an adult and child. The dose coefficients were obtained from RadToolbox [20], which employs the ICRP 72 values [38]. Inhalation dose coefficients are reported in units of Bq/rem. For the purposes of satisfying the action level criteria of 250-mSv, the dose coefficients can converted to units of Bq per 250-mSv of intake. For each of the five radionuclides, the dose coefficients for an adult and child are also summarized in Table 4.3.1.

Table 4.3.1 Environmental Inhalation Dose Coefficients

Nuclide	Default Lung Absorption Type	Adult Inhalation Coefficient (Bq/250-mSv Intake)	Child Inhalation Coefficient (Bq/250-mSv Intake)
^{241}Am	M	5.95E+03	6.25E+03
^{60}Co	M	2.50E+07	1.67E+07
^{137}Cs	F	5.43E+07	1.25E+08
^{131}I	F	3.38E+07	1.32E+07
^{192}Ir	M	4.81E+07	3.29E+07

The fraction of retention for only the significantly contributing compartments was determined for each of the five radionuclides under investigation over a period of 30 days. Note that the ET1 (anterior nose) and ET2 (posterior nasal passage, mouth, larynx, pharynx) compartments from the ICRP Publication 66 respiratory tract model [27] were subtracted from the retained lung fraction calculated in DCAL. This rationale is based on the premise that should a patient blow their nose prior to screening, most of the contamination from these passages will be removed.

The retention is a function of the biological metabolic processes, as well as the nuclide's half-life. The DCAL results are displayed in Figures 4.4.1 through 4.4.6. Sample DCAL results for ^{137}Cs (Fast) and ^{60}Co (Moderate) with the ET1 and ET2 compartments removed are displayed in Figures 4.4.7 and 4.4.8.

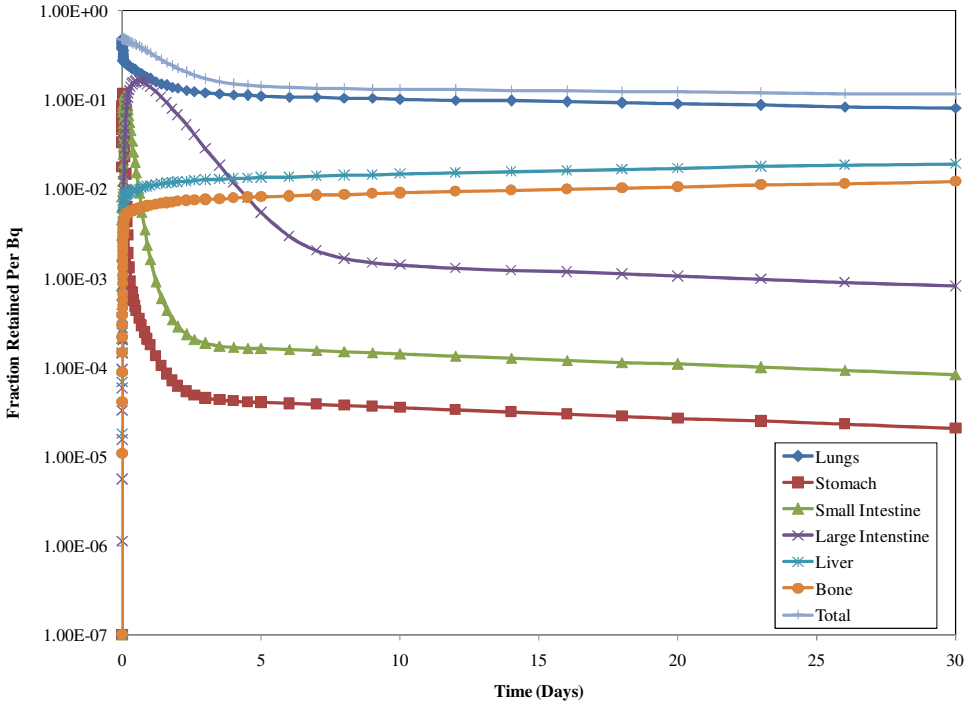

Figure 4.4.1 Retention of ^{241}Am (Moderate) in Major Contributing Compartments over a 30-Day Period

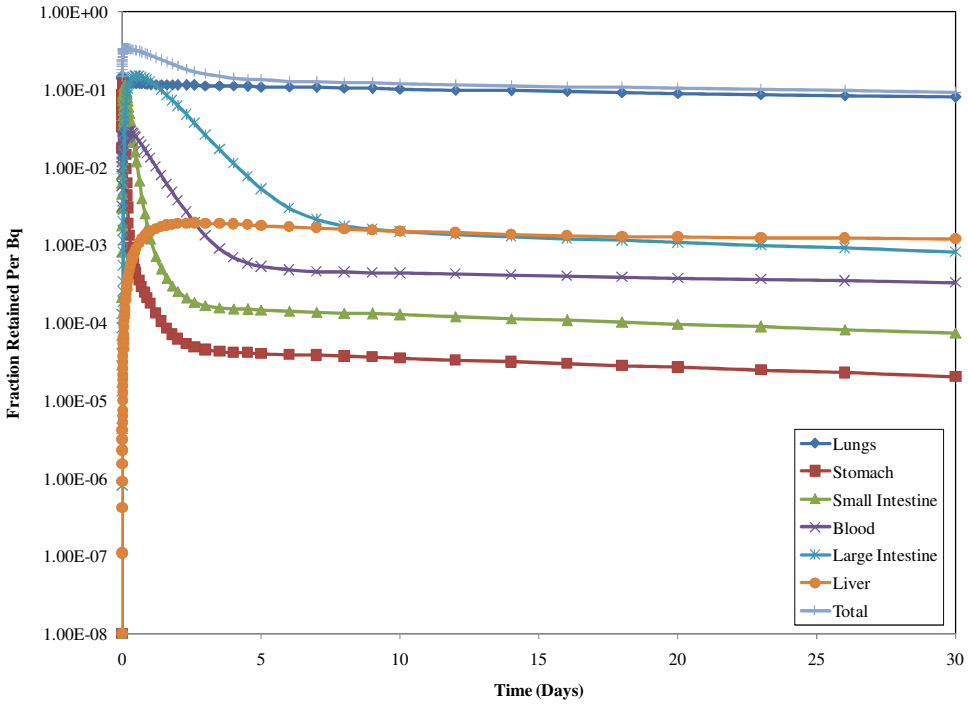

Figure 4.4.2 Retention of ^{60}Co (Moderate) in Major Contributing Compartments over a 30-Day Period

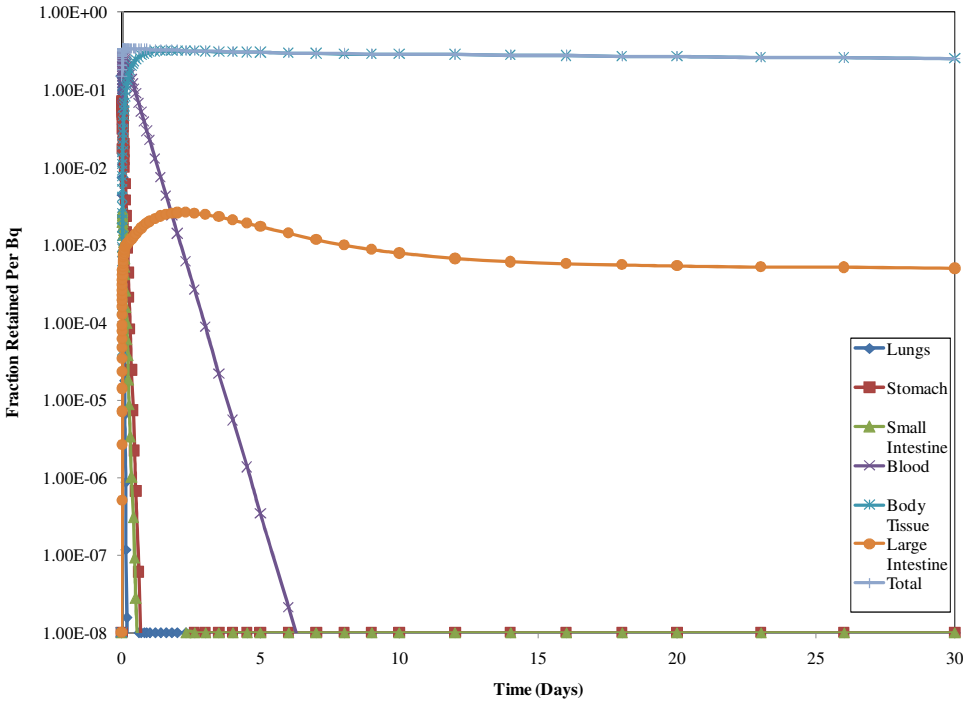

Figure 4.4.3 Retention of ^{137}Cs (Fast) in Major Contributing Compartments over a 30-Day Period

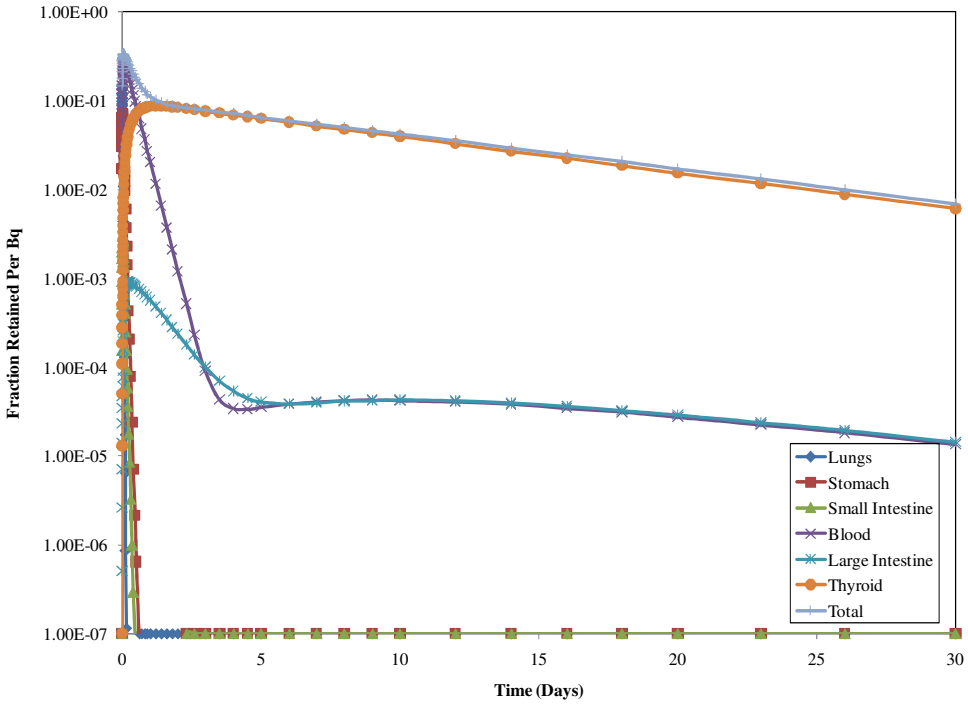

Figure 4.4.4 I Retention of ^{131}I (Fast) in Major Contributing Compartments over a 30-Day Period

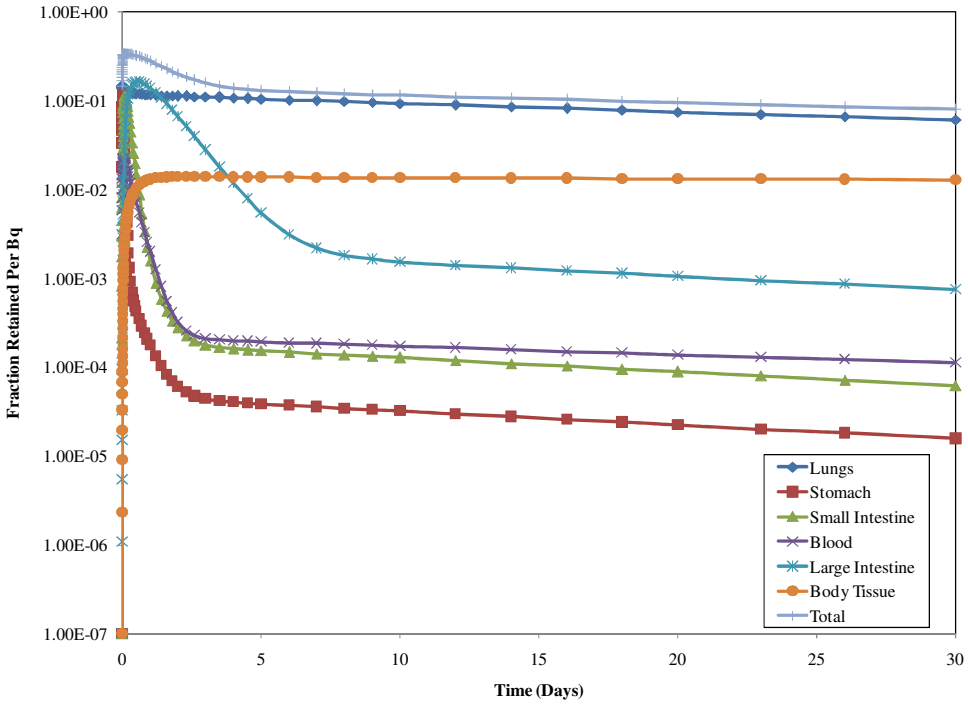

Figure 4.4.5 Retention of ^{192}Ir (Moderate) in Major Contributing Compartments over a 30-Day Period

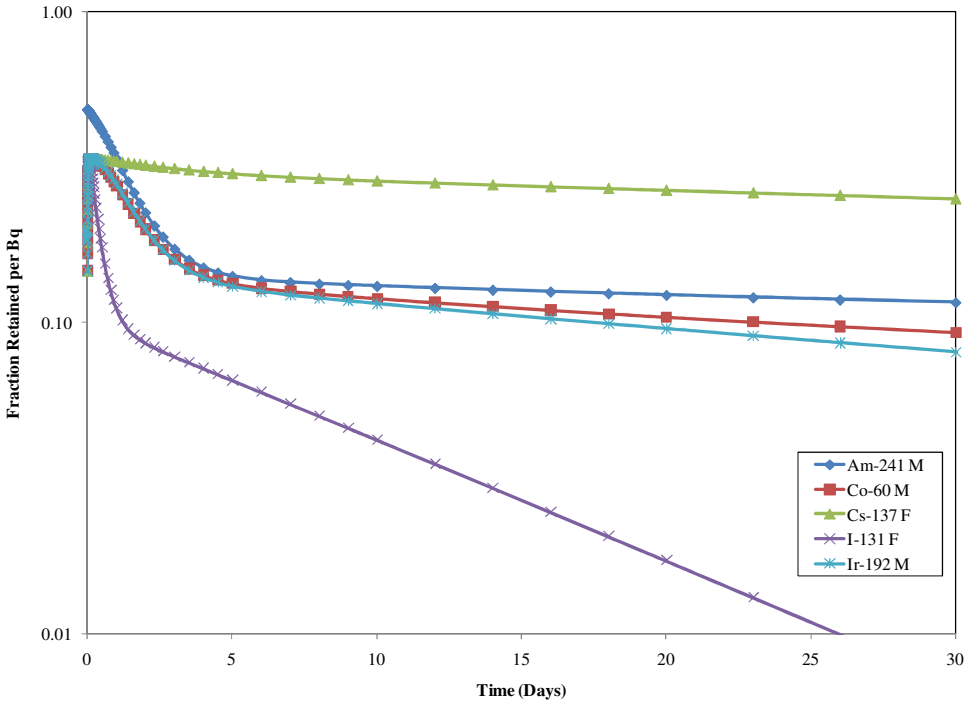

Figure 4.4.6 Comparison of Total Fraction Retention per Bq Inhaled for each Radionuclide

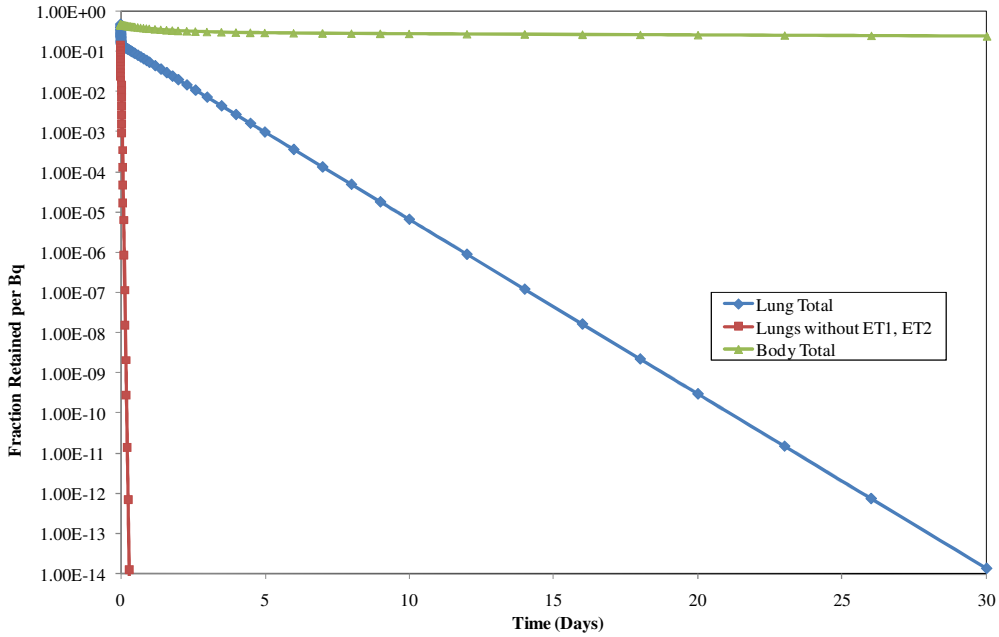

Figure 4.4.7 Comparison of Fraction Retention per Bq for Lung Compartments with ET1 and ET2 Removed for ^{137}Cs (F)

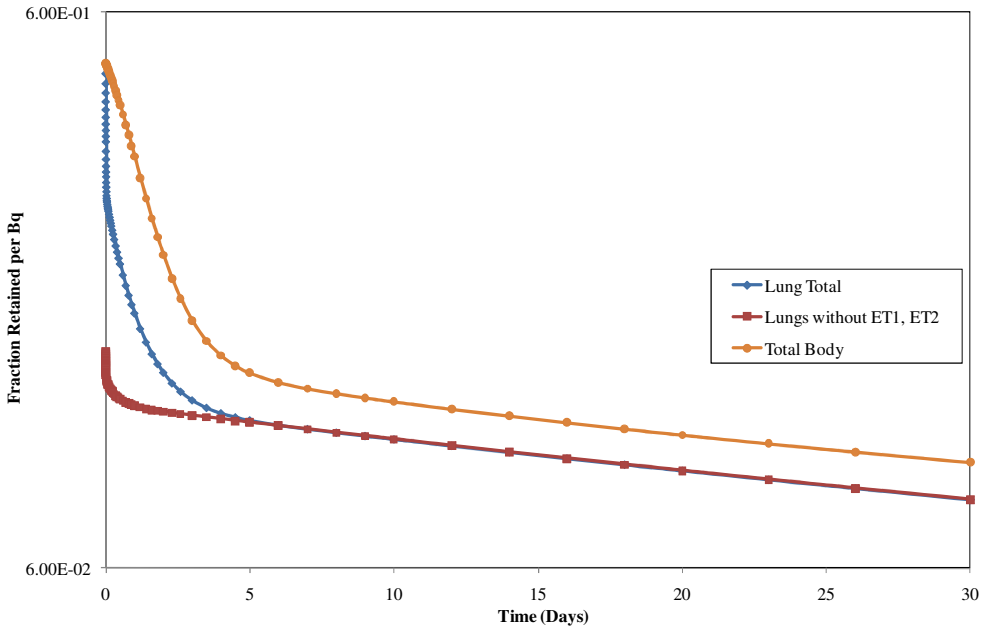

Figure 4.4.8 Comparison of Fraction Retention per Bq for Lung Compartments with ET1 and ET2 Removed for ^{60}Co (M)

The DCAL results indicate that a majority of the inhaled contamination is exhaled and the remainder travels through the GI and pulmonary systems. From the five radionuclides, ^{137}Cs has the highest retention rate over the 30-day span, where ^{131}I decays more rapidly with the lowest retention rate, fastest metabolic uptake, and short half-life. The organs that retain the greatest fraction for each nuclide were listed in Table 4.3.2.1. Certain nuclides tend to accumulate in specific compartments, as is the case seen with ^{131}I accumulating in the thyroid gland. In the case of ^{137}Cs, a significant majority of the contamination is retained in the body tissue, which includes breast, adipose, and muscle tissue.

The understanding of biological and radiological interactions is integral in determining dose due to inhaled contamination. Summing the contributions from each source organ from the MCNP pulse height tally, in conjunction with the biokinetic modeling - which contributes the fractional organ contribution as a function of time per Bq of intake - yields a total count rate

from detector per Bq of intake. With the 250-mSv threshold action level for triage screening, the final count rates are thus reported in counts-per-minute per 250-mSv intake. This can be easily reverted to counts-per-minute per Bq of intake should the action level be modified.

CHAPTER 5: RESULTS

5.1 Benchmark Experimental and Computational Spectra

The basis of assessing inhaled contamination in a model of the human body relies on computer simulation of the detector response to the time-dependent movement of inhaled contamination. In order to ensure an accurate detector response, the benchmark measurements were made using a PMMA slab phantom and compared to its MCNP counterpart, thus validating the NaI(Tl) detector model. For each of the six radionuclides outlined in Table 3.2.1, a comparison of the measured and MCNP simulated spectra for 0-mm, 30-mm, and 60-mm attenuating thicknesses of PMMA is presented in Figures 5.1.1 through 5.1.6.

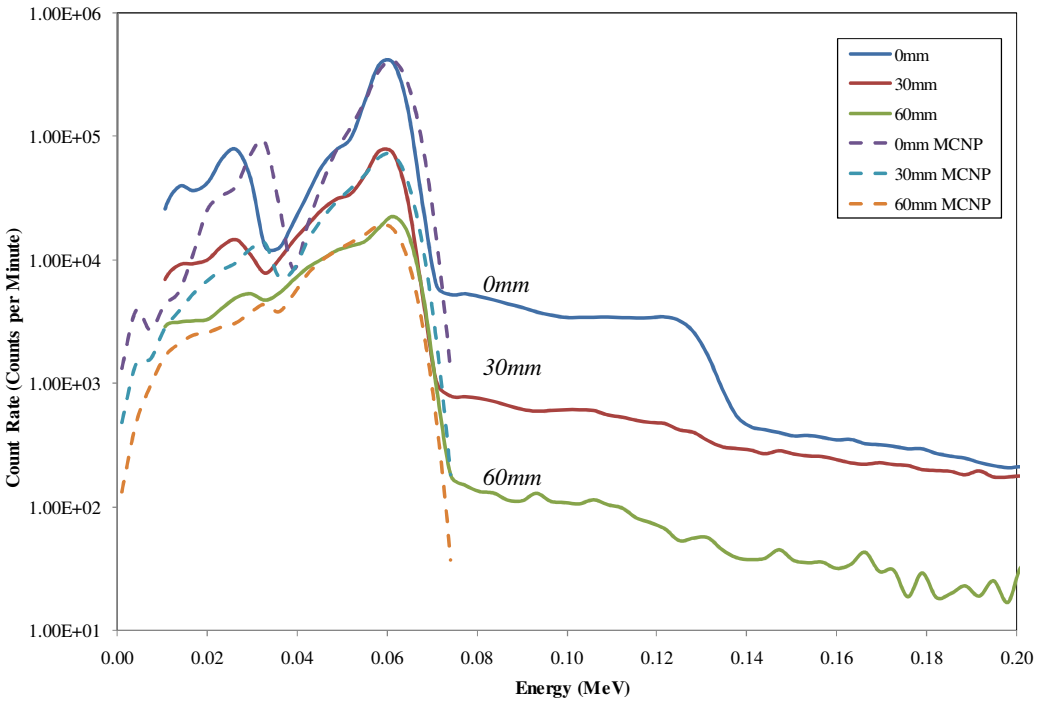

Figure 5.1.1 Measured (Solid) and Simulated (Dashed) Spectra for ^{241}Am with 0-mm, 30-mm, and 60-mm PMMA Attenuation

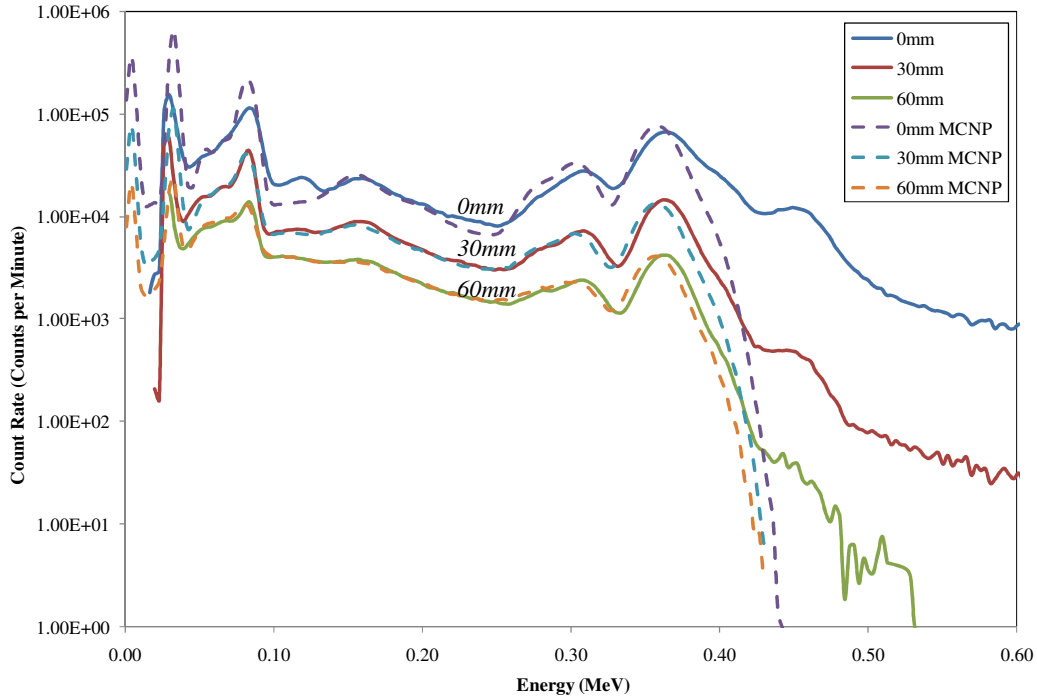

Figure 5.1.2 Measured (Solid) and Simulated (Dashed) Spectra for ^{133}Ba with 0-mm, 30-mm, and 60-mm PMMA Attenuation

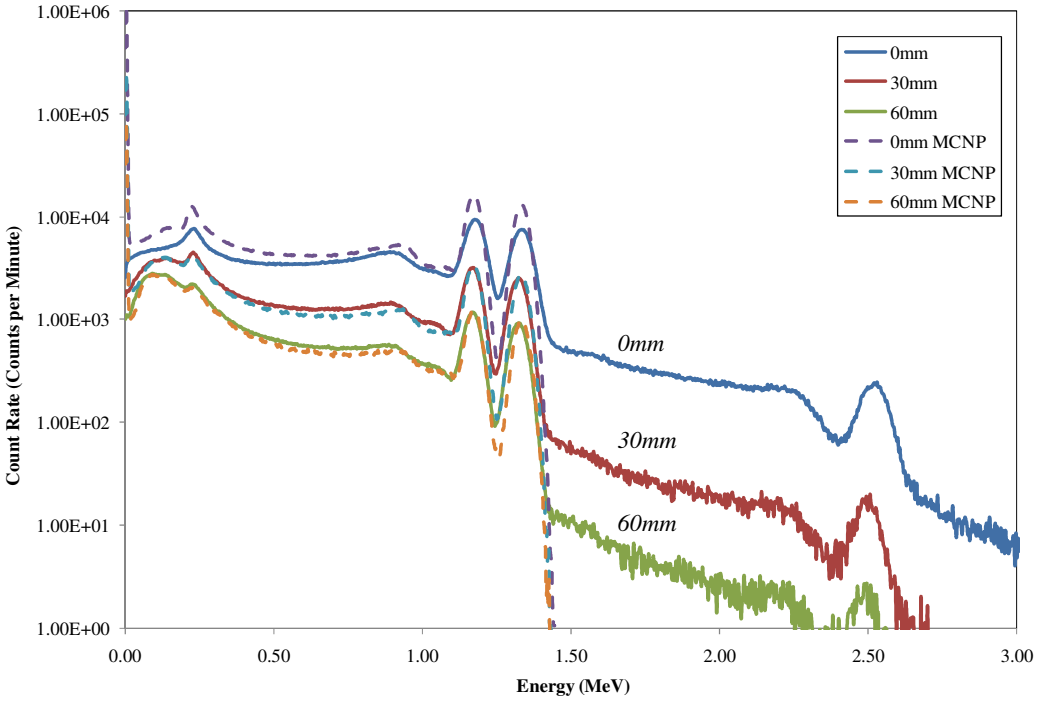

Figure 5.1.3 Measured (Solid) and Simulated (Dashed) Spectra for ^{60}Co with 0-mm, 30-mm, and 60-mm PMMA Attenuation

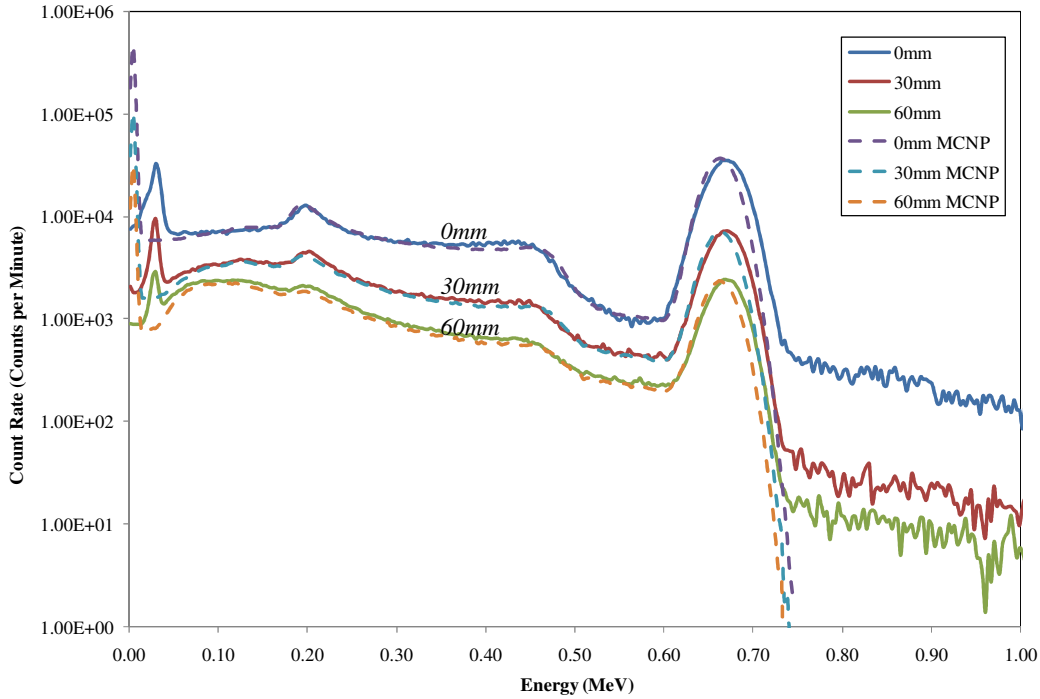

Figure 5.1.4 Measured (Solid) and Simulated (Dashed) Spectra for ^{137}Cs with 0-mm, 30-mm, and 60-mm PMMA Attenuation

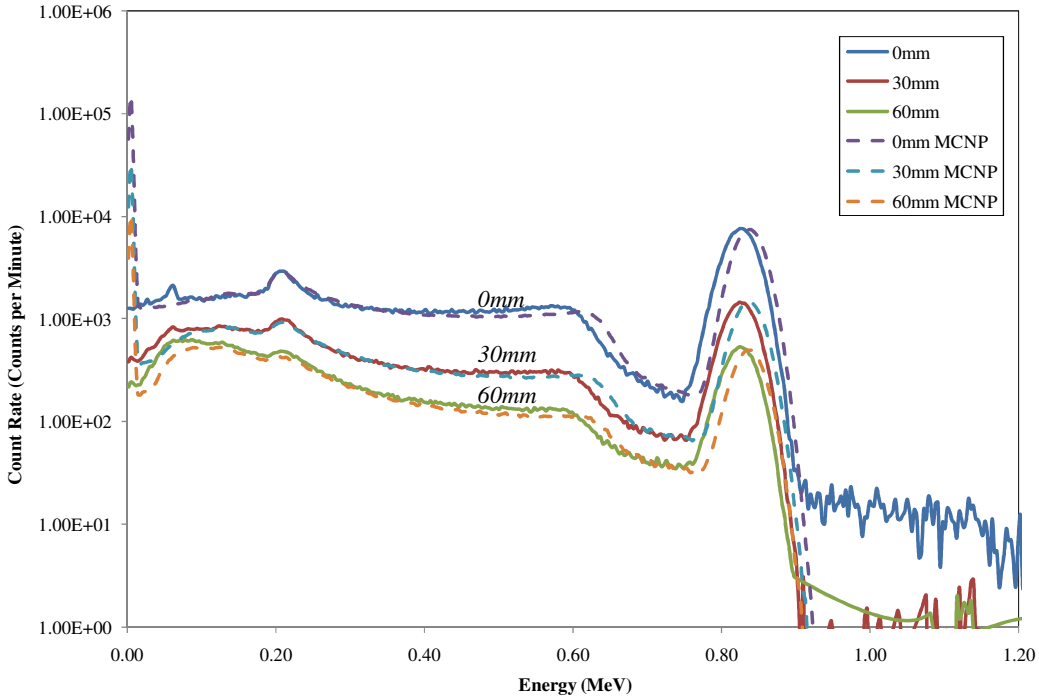

Figure 5.1.5 Measured (Solid) and Simulated (Dashed) Spectra ^{54}Mn with 0-mm, 30-mm, and 60-mm PMMA Attenuation

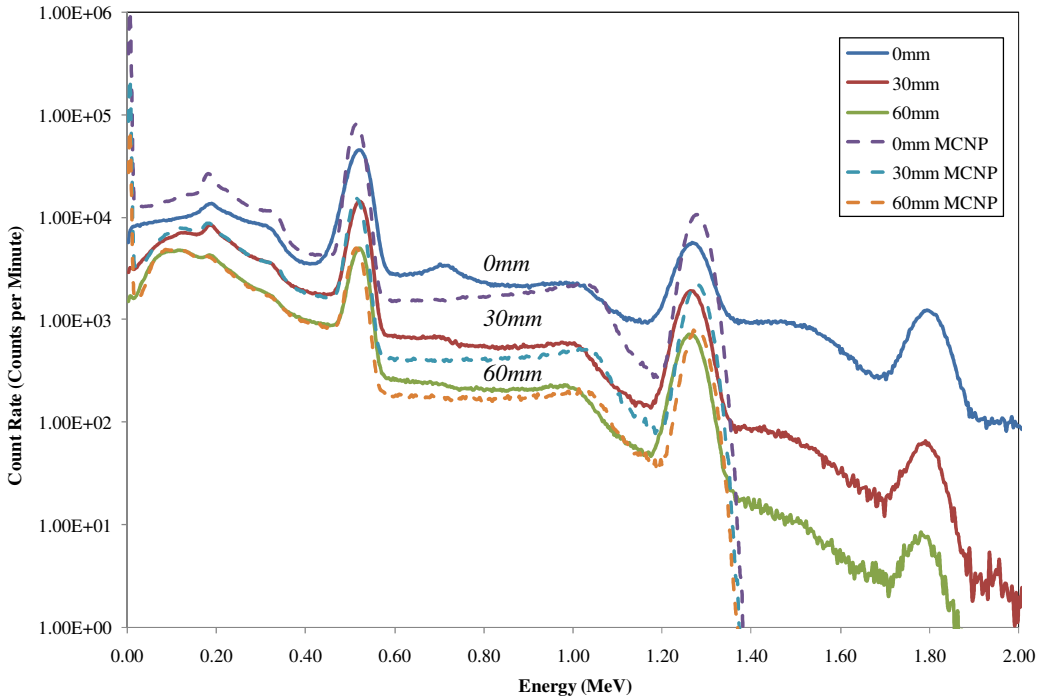

Figure 5.1.6 Measured (Solid) and Simulated (Dashed) Spectra for ^{22}Na with 0-mm, 30-mm, and 60-mm PMMA Attenuation

Summation effects occur in the slab phantom spectra with ^{137}Cs and ^{60}Co. Thus, in order to project the actual counts that occur within the primary peak, the fraction of counts in the peak ROI was plot as a function of the total counts (including the summation events) and empirically fit to a simple-fit function (Figure 5.1.7). Since MCNP does not produce summation events, the count-rates from anthropomorphic phantoms must be translatable back into an accurate detector response – including summation events. As disussed in the next section, count rates beyond the upper limit of the measured data will tend to indicate noticable summation has occurred. This empirical method is further reinforced by requring the traige personnel operating the detector to note if the dead-time of the detector is above a certain limit, indicating a high event rate. This procedure is outlined in the triage summary sheets in Appendix D, which are used to determine if a patient requires further medical attention.

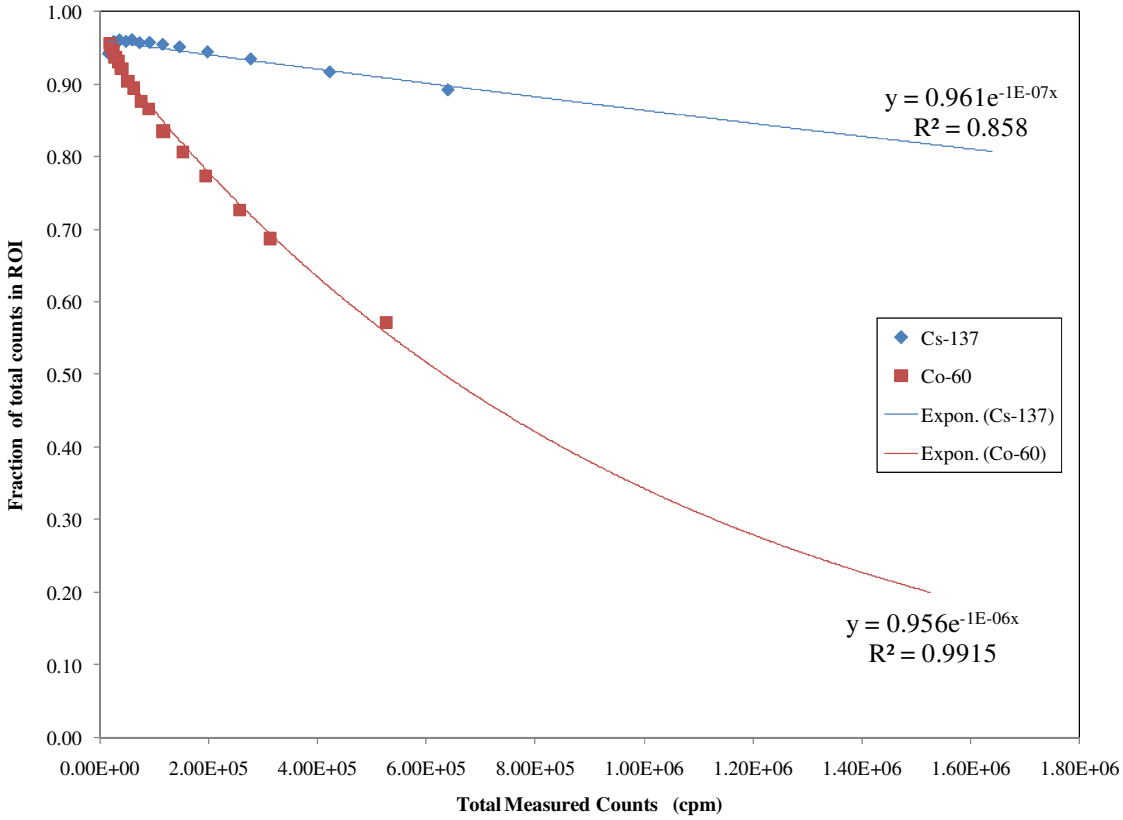

Figure 5.1.7 Fraction of Counts Occurring in Region of Interest (ROI) as a Function of Total Measured Counts (including Summation Events) with Exponential Fit

5.2 Model Validation and Scaling Factors

As described in §3.2, the ROIs selected to encompass the photopeaks for each of the investigated nuclides are given in Table 5.1.1. Additionally, the ROIs for the summation effects due to summation peaks for ^{22}Na, ^{60}Co, and ^{137}Cs are also listed in Table 5.1.1. In order to preserve the true counts of the full energy gamma reaching the detector, it is imperative to redistribute these summed counts back into the photopeak energy region of the measurement for comparison with the simulation results.

Table 5.1.1 Counting Regions of Interest for PMMA Slab Phantom Measurements

Nuclide	Peak Energy (keV)	ROI on MCA (Channels)	ROI (keV)
^{241}Am	59.5	[13, 26]	[32.6, 73.9]
^{133}Ba	276.4, 302.9, 356.0	[81, 132]	[248.6, 410.6]
^{60}Co	1173.2, 1332.5	[348, 393]	[1096.7, 1411.1]
	2505.7 *(Sum Coincidence Peak)*	[753, 831]	[2383.0, 2630.8]
^{137}Cs	661.7	[188, 233]	[588.5, 731.4]
	1323.4 *(Sum Coincidence Peak)*	[382,442]	[1204.7, 1395.2]
^{54}Mn	834.8	[242, 281]	[760.0, 883.9]
^{22}Na	511.0 *(Annihilation Peak)*	[147, 182]	[458.2, 569.4]
	1274.5	[370, 432]	[1166.5, 1363.5]
	1785.5 *(Sum Coincidence Peak)*	[538, 600]	[1700.1, 1897.1]

In order to validate the detector model, the ratio of the counts in the ROI photopeak for both the experimental and computational results must be constant over all thicknesses of PMMA for each of the six radionuclides. For each nuclide, the ratios fluctuate about a mean, and overlap with the mean within reasonable error. The six radionuclides were selected to validate the detector model over a range of energies and PMMA thicknesses from 0-mm to 90-mm (with the exception of ^{133}Ba and ^{241}Am, which were validated up to 60-mm). The results are displayed in Figures 5.2.2 through Figure 5.2.8.

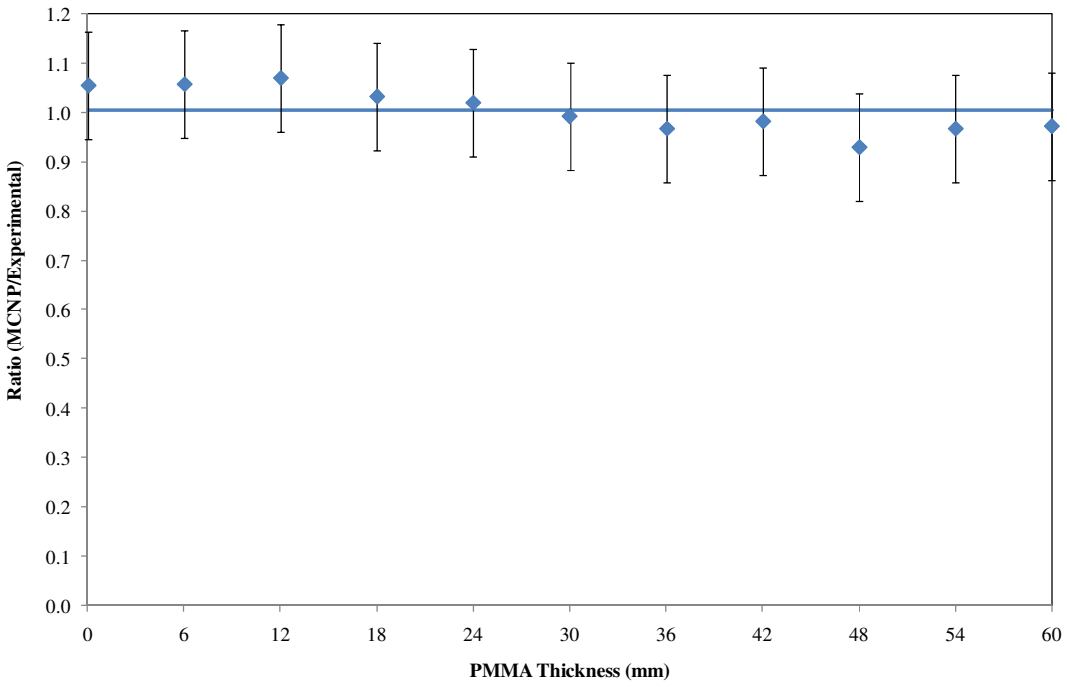

Figure 5.2.1 ^{241}Am Scaling Factor for 59.5-keV Peak ROI

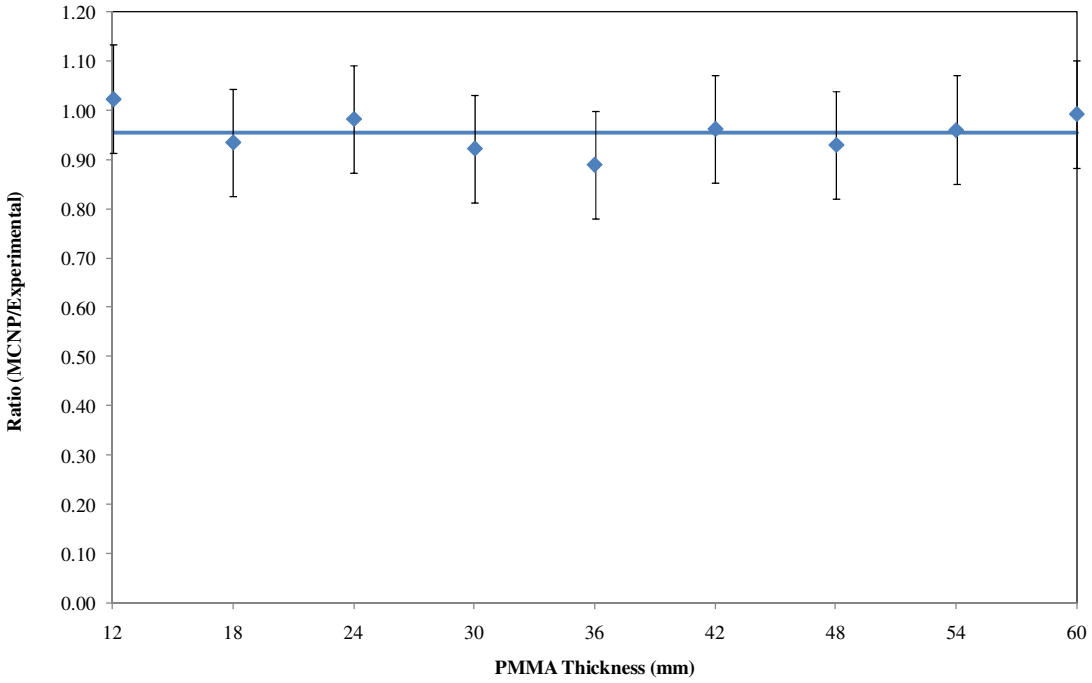

Figure 5.2.2 ^{133}Ba Scaling Factor for Combined 276.4-keV, 302.9-keV and 356.0-keV Peak ROIs

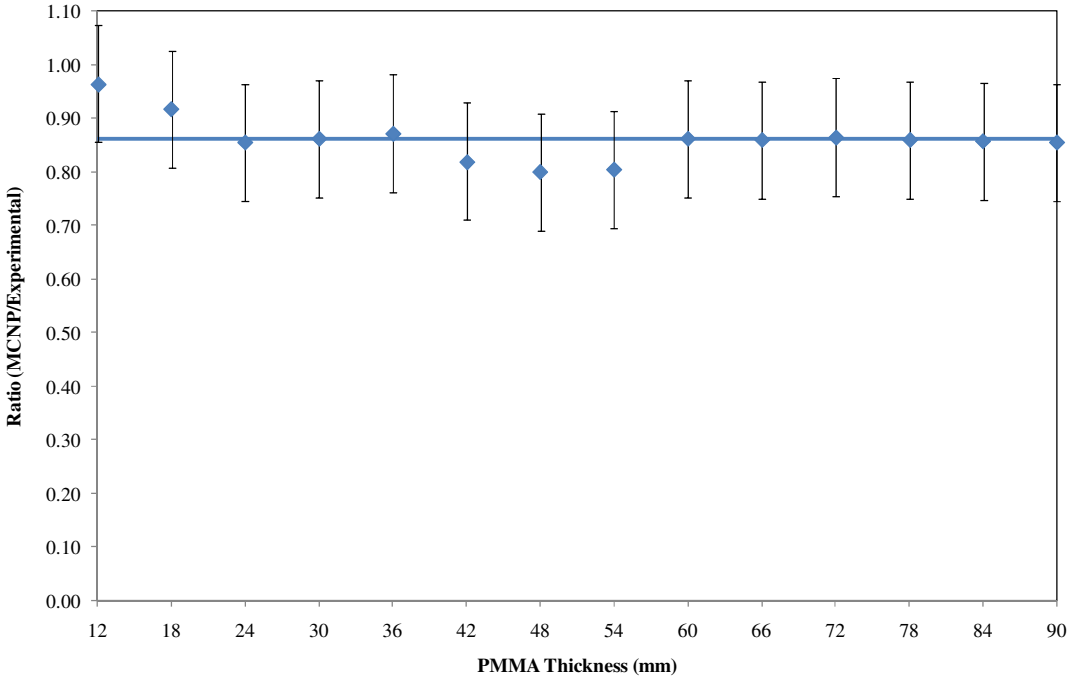

Figure 5.2.3 ^{60}Co Scaling Factor for Combined 1173.2-keV and 1332.5-keV Peak ROIs

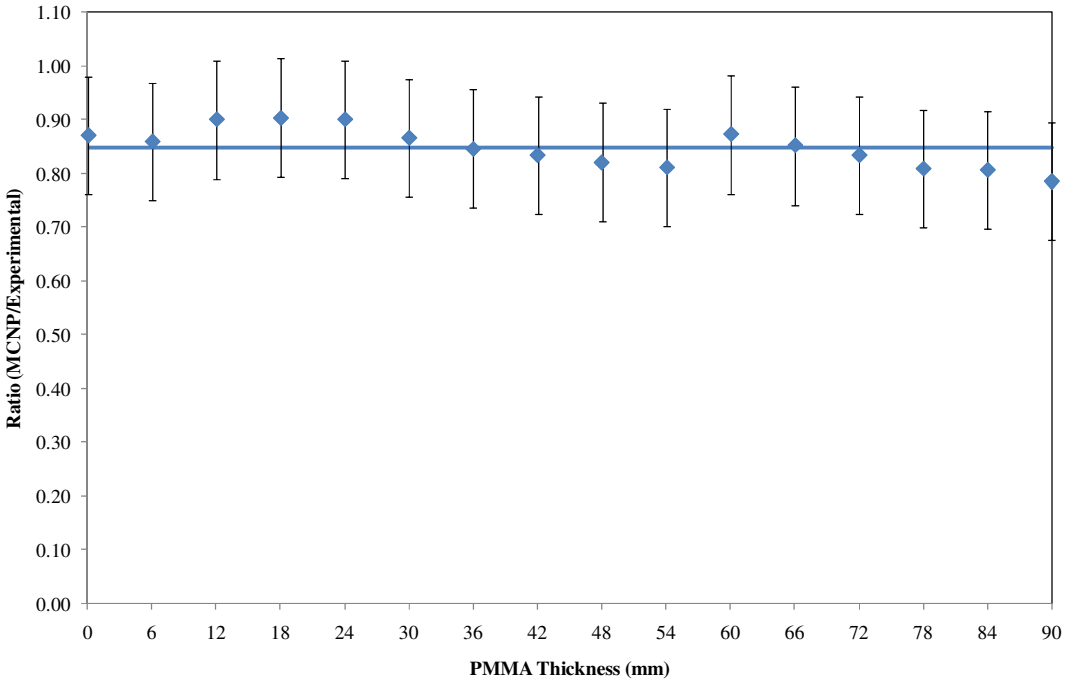

Figure 5.2.4 ^{137}Cs Scaling Factor for 661.7-keV Peak ROI

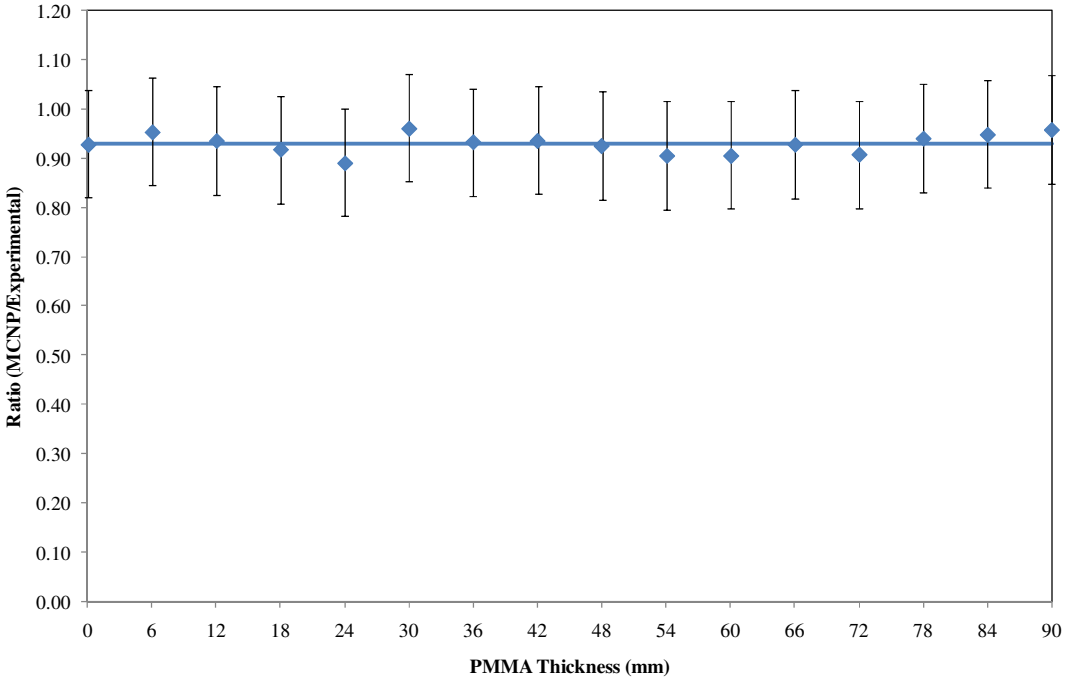

Figure 5.2.5 ^{54}Mn Scaling Factor for 834.8-keV Peak ROI

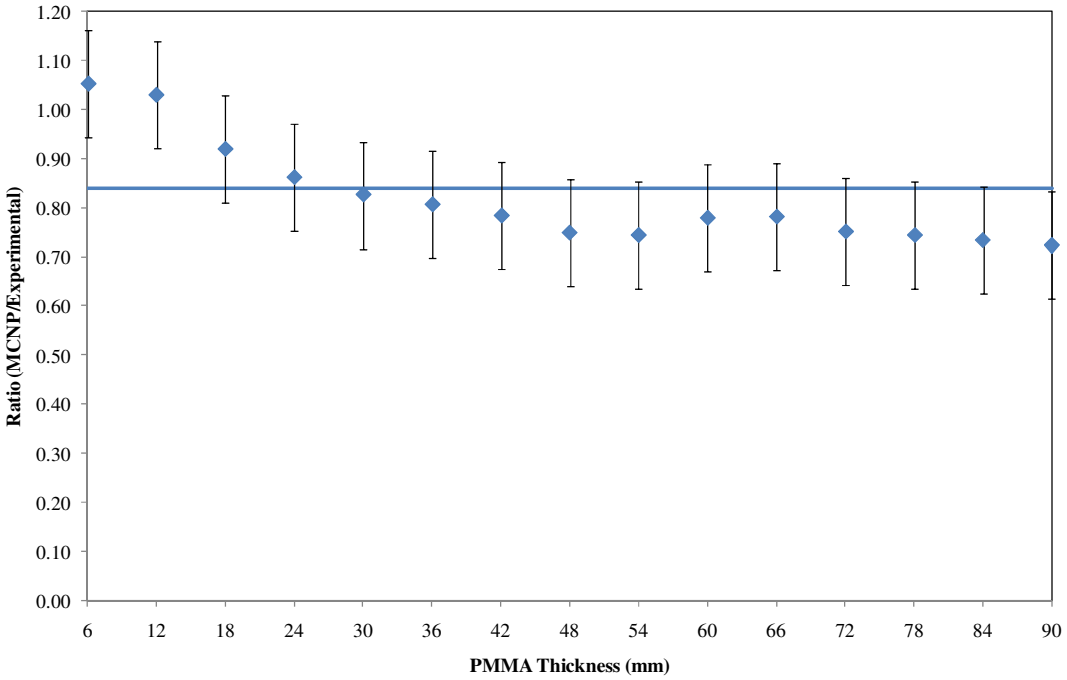

Figure 5.2.6 ^{22}Na Scaling Factor for 511-keV Peak ROI

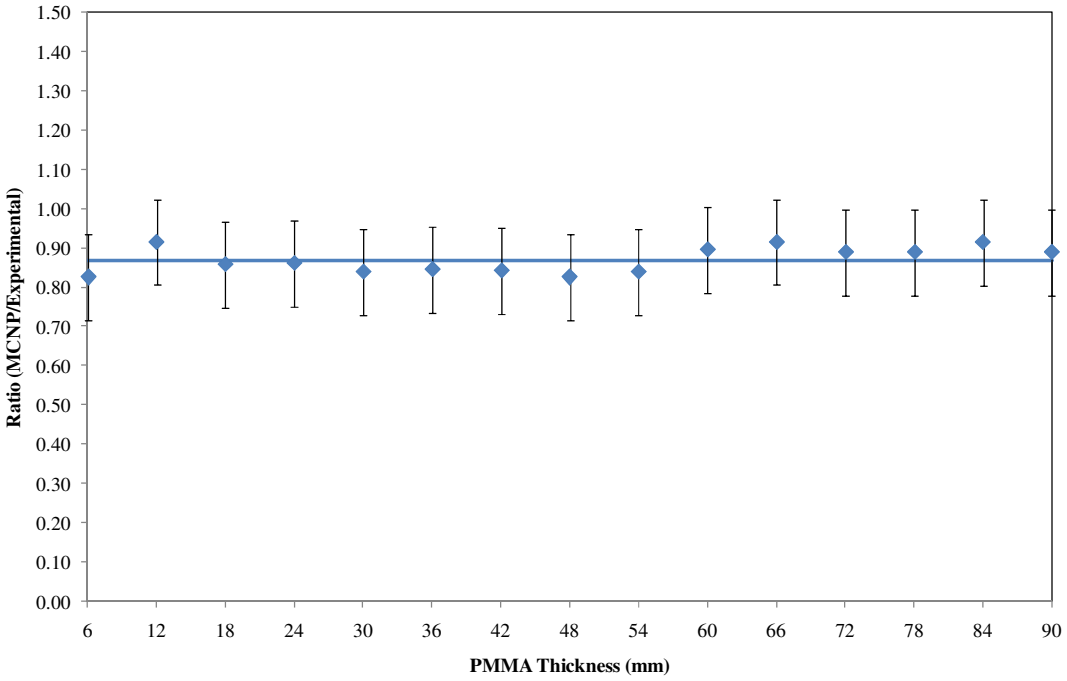

Figure 5.2.7 ^{22}Na Scaling Factor for 1274.5-keV Peak ROI

The mean value about which the ratios fluctuate is referred to as the scaling factor, which quantifies the detector efficiency characteristics. These scaling factors vary for different individual nuclides, thus indicating an energy-dependent response from the detector. The error bars tend to overlap with the mean, and the overall error of all the nuclides fall within 1.35× the standard deviation of the mean. Sources of error contributing to the scaling factor error include a predominant 3.3% error in the checked source activity, statistical counting error from gross and background counts (<0.11% data error), and the pulse-height tally bin error (<0.001%). Once the scaling factor is applied to MCNP data, the MCNP output closely resembles the experimental data. An example for ^{137}Cs is shown in Figure 5.2.8.

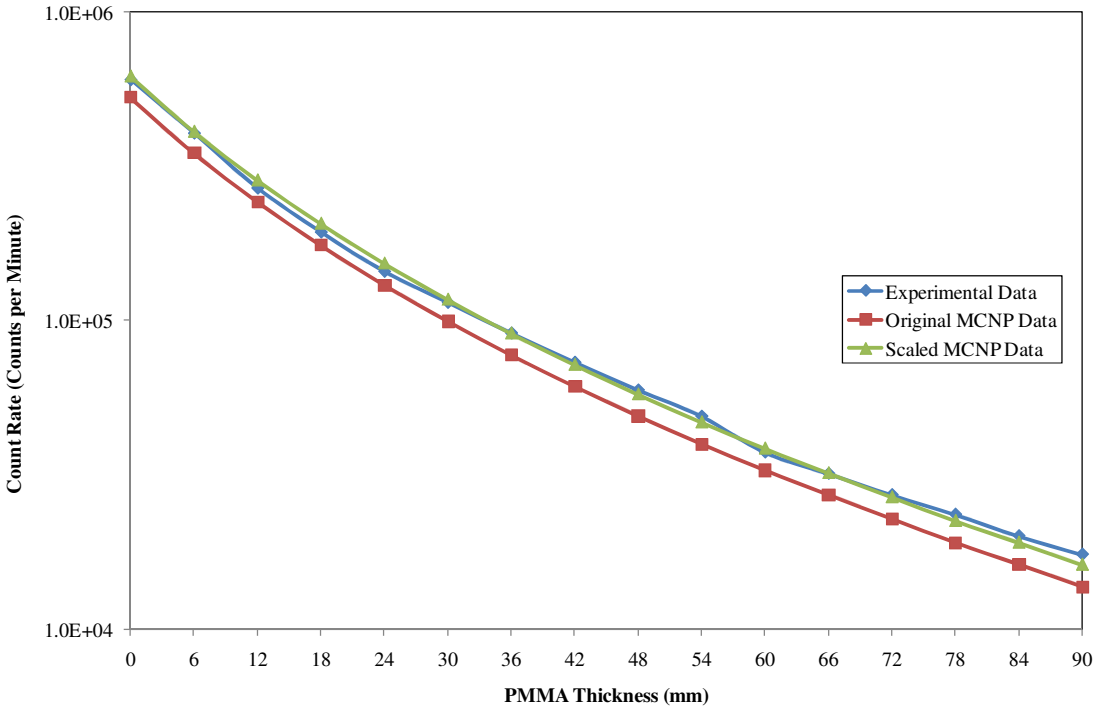

Figure 5.2.8 ^{137}Cs Slab Phantom Comparison of MCNP to Experimental Count Rates after Application of Scaling Factor

Statistical outliers for very small thicknesses of PMMA, such as 0-mm with ^{22}Na and 0-mm and 6-mm for ^{133}Ba and ^{60}Co, were eliminated using Grubbs' test method, which eliminates values that do not fall within the 95% confidence interval of a Gaussian distribution [39]. These outliers may be caused by contamination by gamma-ray sources in the surroundings, as well as a high activity source that would an increase in summation events and inflating the scaling factor. It is permissible to eliminate these outliers at such low thicknesses considering the anteriposterior thickness of the MIRD Reference Man has a mass thickness of 4.26-g/cm^2 [2]. Comparatively, PMMA has a density of 1.19-g/cm^3, which corresponds to an equivalent PMMA thickness of 35.8-mm. Thus, weighting the data toward more realistic attenuation effects is warranted. As a point of comparison, the Reference Male phantom has a chest wall mass thickness of 2.18-g/cm^2, or 21-mm [2]. In the event of assessing a highly contaminated individual, it may even be recommended to not position the detector directly in against the patient, in order to mitigate these effects due to high-incident events.

From the six isotopes used to determine the energy-dependent response of the detector, three are directly applicable to the nuclides of interest used to contaminate the anthropomorphic phantoms. However, two nuclides used in the phantom simulations, ^{131}I and ^{192}Ir, were not included in the benchmark experiments. Therefore, their scaling factors were extrapolated via an energy-dependent linear interpolation based on the benchmark radionuclide scaling factors. Their ROIs were determined based on running a simulation with the slab phantom (with 0-mm thickness), and the respective ^{192}Ir or ^{131}I source replaced. Since the ROIs are to be arbitrarily selected to encompass the peak, any slight variance between the detector and simulated ROIs should be inconsequential. The scaling factors employed with the anthropomorphic phantoms are summarized in Table 5.2.1.

Table 5.2.1 Scaling Factors Employed for Anthropomorphic Phantom Nuclide Contaminants

Nuclide	Peak ROI Energy (keV)	Scaling Factor (MCNP/Experimental)
^{241}Am	59.5	1.00±0.03
^{60}Co	1173.2, 1332.5	0.86±0.03
^{137}Cs	661.7	0.85±0.03
^{131}I	364.5	0.9±0.1
^{192}Ir	316.5	0.96±0.06

Upon simulating the appropriate measurements and obtaining a constant-averaged scaling factor from the detector response, the detector model was validated for use with the anthropomorphic phantoms.

5.3 MIRD Phantom Results

Upon verification of the detector model, six anthropomorphic phantoms were modeled with nuclides distributed throughout select organs for each of the five sources under consideration. After simulation, the data were combined with the time-dependent biokinetic modeling to determine the threshold count-rate values expected for individuals with a committed effective dose due to 250-mSv of contamination.

In the MCNP model of the anthropomorphic phantoms, the SCX tally modifier was employed to determine the source organ contribution for each source particle that reaches the detector. The data resulting from the employment of the SCX tally modifier for the Reference Male contaminated with ^{241}Am is depicted in Figure 5.3.1. In the case of ^{241}Am, this figure shows that the body tissue and bones are the major source organs contributing to the detector counts, as americium is a known bone-seeker.

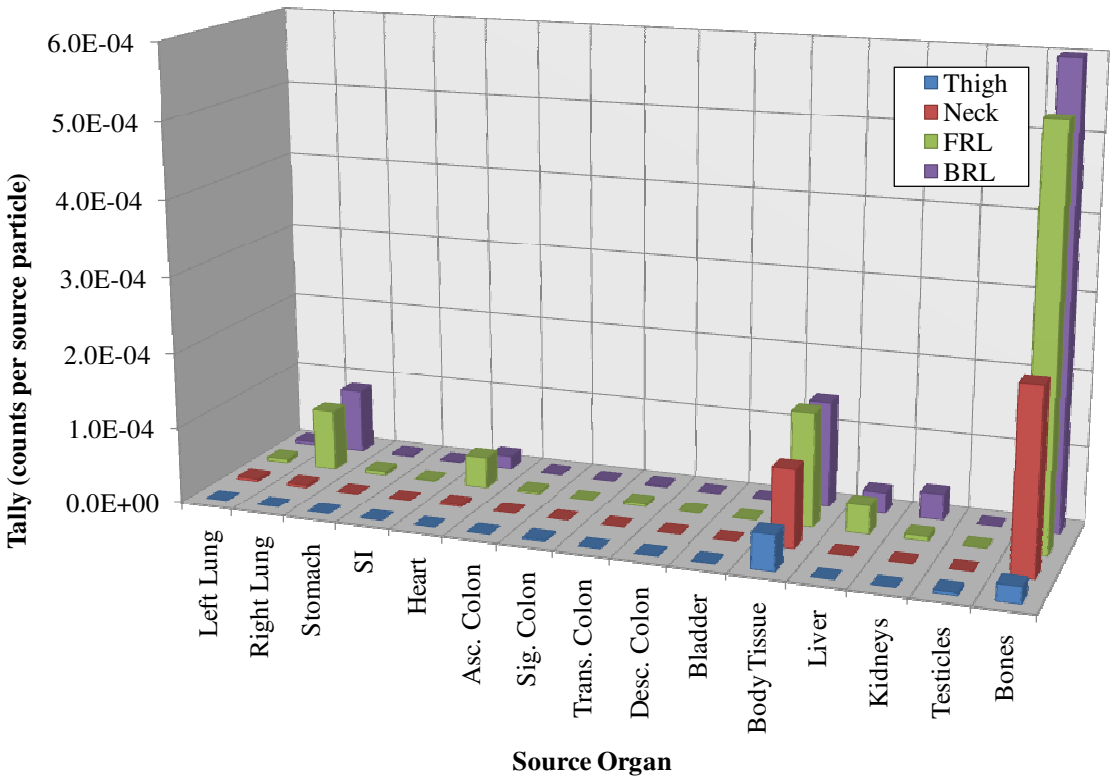

Figure 5.3.1 Male Phantom SCX Source Organ Contribution for ^{241}Am (Number of Particles Tallied per Source Particle in Each Organ)

Once the SCX tally data for each source compartment at each detector location was folded with the DCAL biokinetic data, the resulting output was given in counts per Bq of intake activity. Applying the dose conversion factors at the 250-mSv action level yields a final result in count-rate (cpm) per 250-mSv intake. Each detector location was tallied for each of ^{241}Am, ^{60}Co, ^{137}Cs, ^{131}I, and ^{192}Ir. A sample of the final count-rates for ^{137}Cs and ^{131}I (with optimal locations highlighted) are given in Tables 5.3.1 and 5.3.2. The data for all phantoms and nuclide combinations are provided in Appendix C.

Table 5.3.1 Count-Rate per 250-mSv Intake for Reference Male Contaminated with ^{137}Cs

Reference Male: ^{137}Cs F				
Days	**Posterior Right Lung (cpm per 250-mSv Intake)**	**Anterior Right Lung (cpm per 250-mSv Intake)**	**Anterior Neck (cpm per 250-mSv Intake)**	**Lateral Left Thigh (cpm per 250-mSv Intake)**
0.0	3.58E+04	3.38E+04	5.05E+03	4.81E+01
0.2	1.37E+05	1.48E+05	9.42E+04	5.02E+04
0.5	2.14E+05	2.27E+05	1.56E+05	8.28E+04
1.0	2.55E+05	2.70E+05	1.89E+05	1.00E+05
2.0	2.62E+05	2.76E+05	1.94E+05	1.03E+05
3.0	2.57E+05	2.71E+05	1.90E+05	1.01E+05
4.0	2.52E+05	2.66E+05	1.87E+05	9.94E+04
5.0	2.48E+05	2.62E+05	1.84E+05	9.78E+04
6.0	2.45E+05	2.58E+05	1.82E+05	9.66E+04
7.0	2.42E+05	2.56E+05	1.80E+05	9.55E+04
8.0	2.40E+05	2.53E+05	1.78E+05	9.46E+04
9.0	2.38E+05	2.51E+05	1.76E+05	9.38E+04
10.0	2.36E+05	2.49E+05	1.75E+05	9.30E+04

Table 5.3.2 Count-Rate per 250-mSv Intake for Reference Male Contaminated with ^{131}I

Reference Male: ^{131}I F				
Days	**Posterior Right Lung (cpm per 250-mSv Intake)**	**Anterior Right Lung (cpm per 250-mSv Intake)**	**Anterior Neck (cpm per 250-mSv Intake)**	**Lateral Left Thigh (cpm per 250-mSv Intake)**
0.0	3.58E+04	3.38E+04	4.56E+03	2.21E+01
0.2	2.24E+04	2.76E+04	5.43E+04	5.50E+03
0.5	1.04E+04	1.38E+04	6.91E+04	2.44E+03
1.0	3.85E+03	6.19E+03	7.50E+04	7.36E+02
2.0	2.24E+03	4.14E+03	7.12E+04	3.90E+02
3.0	2.43E+03	4.17E+03	6.52E+04	5.11E+02
4.0	2.64E+03	4.24E+03	5.97E+04	6.23E+02
5.0	2.78E+03	4.26E+03	5.46E+04	7.06E+02
6.0	2.85E+03	4.22E+03	4.99E+04	7.63E+02
7.0	2.88E+03	4.13E+03	4.56E+04	7.99E+02
8.0	2.86E+03	4.02E+03	4.17E+04	8.17E+02
9.0	2.81E+03	3.88E+03	3.81E+04	8.22E+02
10.0	2.74E+03	3.72E+03	3.48E+04	8.16E+02

The error contribution from the phantom tally outputs is quite small, on the order of 0.01%. The predominant source of error stems from the scaling factors, listed previously in Table 5.2.1. These errors range from approximately 3.5% for the directly computed factors employed in the benchmark validation measurements, to as much as 11% for the interpolated scaling factors.

The optimal location for detector placement in the event of a minimum of 250-mSv of uptake is dependent on the nuclide inhaled. A summary of the optimal detector position for each phantom-nuclide combination based on the highest yielding count-rates is summarized in Table 5.3.3. Overall, the location yielding a sufficient, if not optimal, detectable count-rate is the posterior right lung. As will be discussed, this was the case for all nuclides, with the exception of ^{131}I, where the neck location had proven optimal or very close to optimal for all phantoms, as ^{131}I is a thyroid-seeker.

With the optimal locations for the detector identified in Table 5.3.3, a graphical comparison of the count-rates at these optimal locations for each phantom is given in Figures 5.3.2 through 5.3.6.

Table 5.3.3 Optimal Detector Location for each Phantom-Nuclide Combination

Phantom	Nuclide	Anterior Right Torso	Posterior Right Torso	Anterior Neck	Lateral Left Thigh
Reference Male	^{241}Am		X		
	^{60}Co	*	X		
	^{137}Cs	X	*		
	^{131}I			X	
	^{192}Ir	*	X		
Reference Female	^{241}Am		X		
	^{60}Co		X		
	^{137}Cs		X	*	
	^{131}I			X	
	^{192}Ir		X		
Adipose Male	^{241}Am		X		
	^{60}Co		X		
	^{137}Cs		*	X	
	^{131}I			X	
	^{192}Ir		X		
Adipose Female	^{241}Am		X		
	^{60}Co		X		
	^{137}Cs		X	*	*
	^{131}I			X	
	^{192}Ir		X		
Post Menopausal Adipose Female	^{241}Am		X		
	^{60}Co		X		
	^{137}Cs		X	*	
	^{131}I			X	
	^{192}Ir		X		
Child	^{241}Am		X		
	^{60}Co		X		
	^{137}Cs		X		
	^{131}I			X	
	^{192}Ir		X		

(X) indicates optimal detector location
(*) indicates location count-rate notably close to optimal location

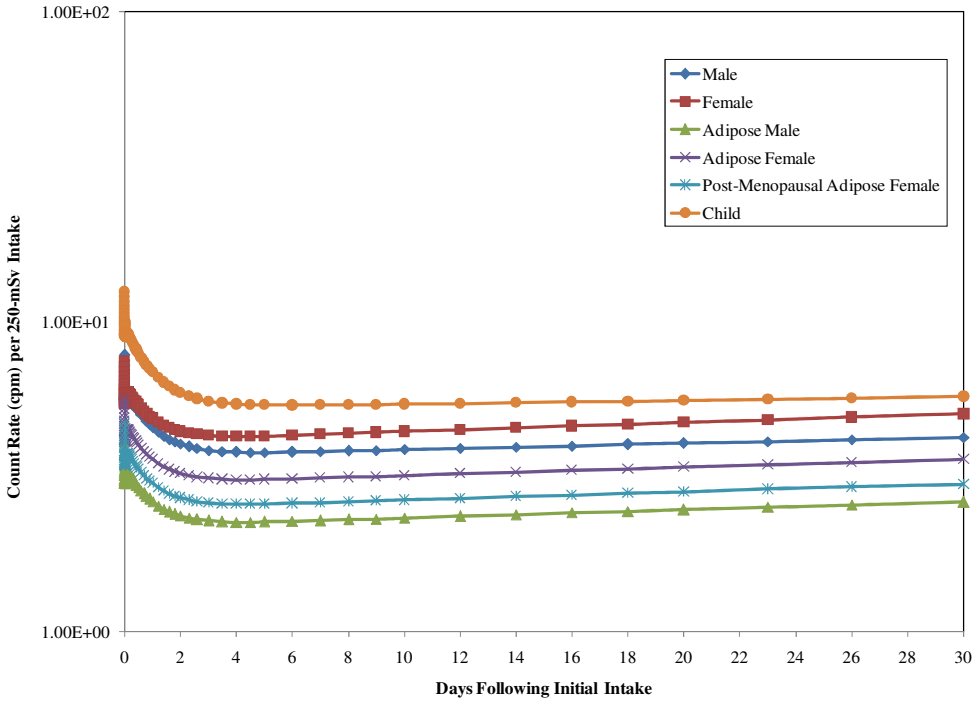

Figure 5.3.2 Comparison of Count-Rate per Phantom for ^{241}Am at Posterior Right Lung Position

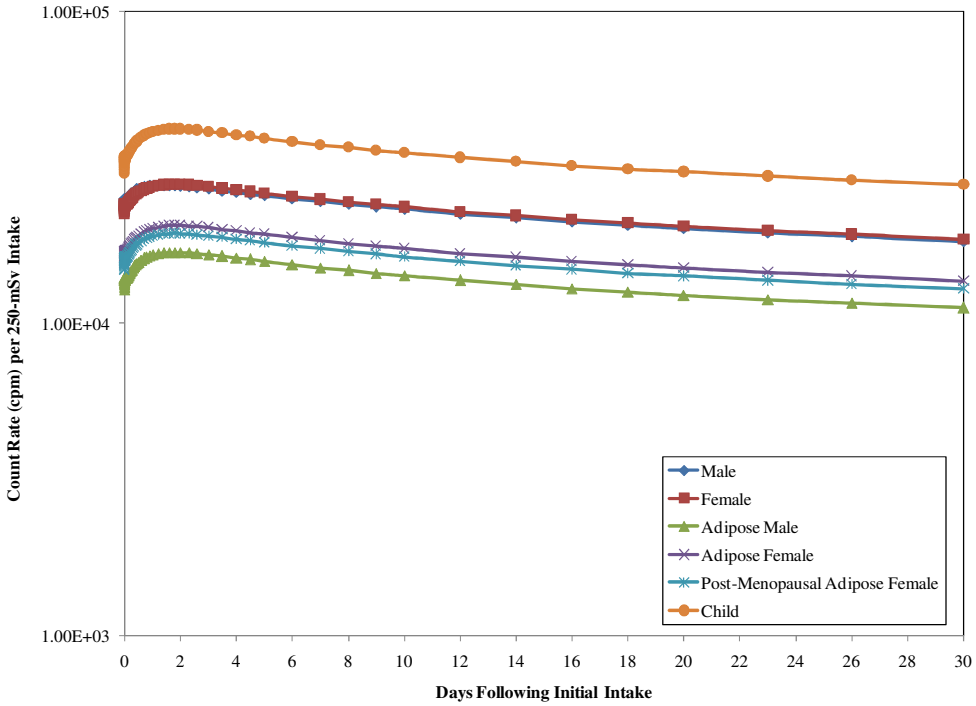

Figure 5.3.3 Comparison of Count-Rate per Phantom for ^{60}Co at Posterior Right Lung Position

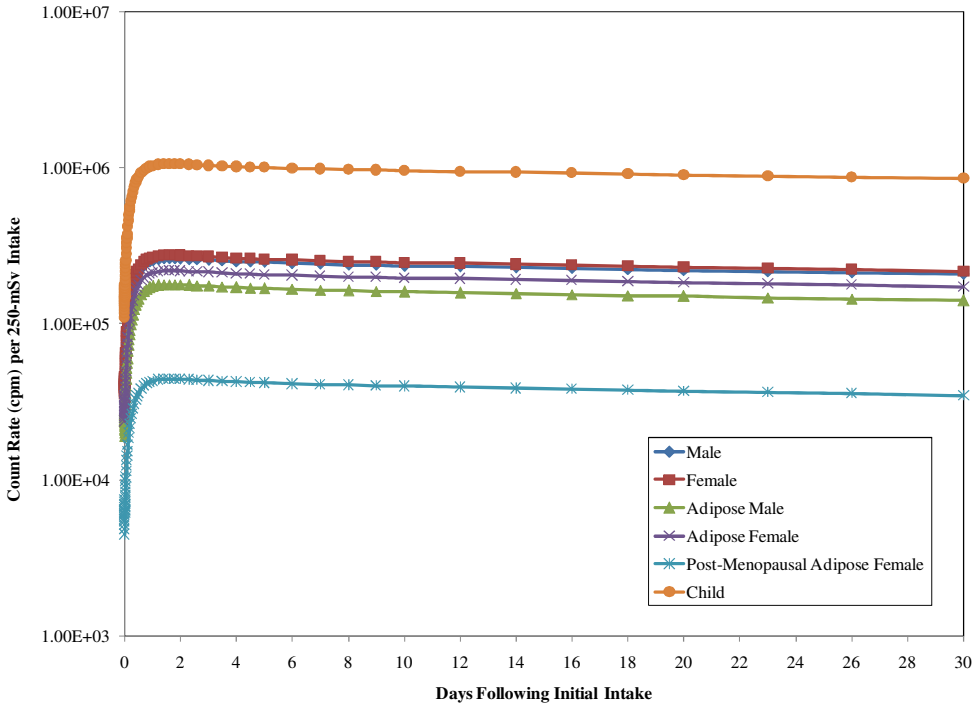

Figure 5.3.4 Comparison of Count-Rate per Phantom for ^{137}Cs at Posterior Right Lung Position

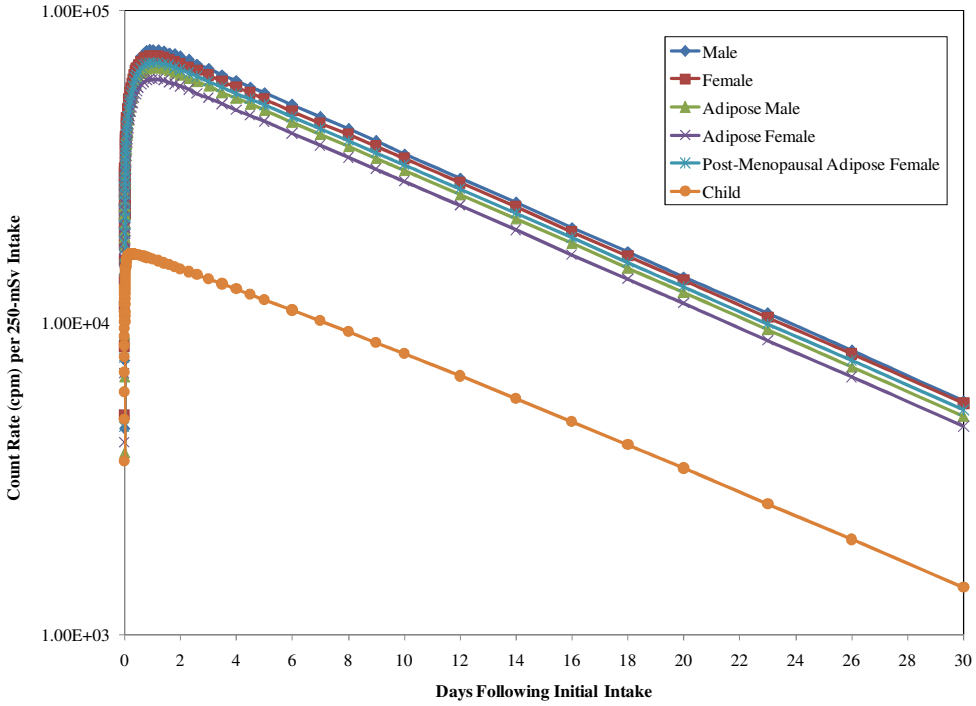

Figure 5.3.5 Comparison of Count-Rate per Phantom for ^{131}I at Anterior Neck Position

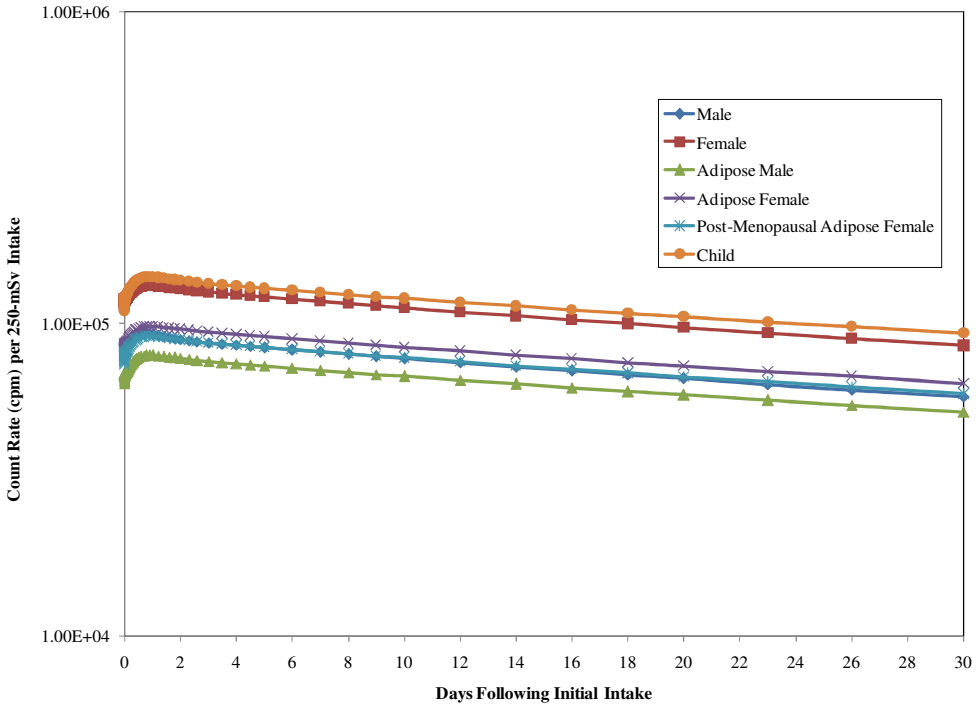

Figure 5.3.6 Comparison of Count-Rate per Phantom for ^{192}Ir at Posterior Right Lung Position

Although body type plays a prominent role in determining detector response and count-rate, it must also be noted that the contaminant nuclide under consideration also contributes to the subsequent detector response by its mode of accumulation in the body. For phantoms with the detector optimally located at the posterior right torso position, the child phantom tended to yield the highest count rate, due to a thin chest wall and comparatively less attenuation. Conversely, the adipose phantoms tended to yield lower count rates, due to increased attenuation by a larger chest wall, breast tissue and fat. The lateral left thigh location was not optimal for any of the detector locations, though was close for the Adipose Female. Although the thigh represents a large form of muscle tissue, and even though many of the source counts for the fast absorption nuclides originate from the body tissue (as will be discussed), the thigh was still not found to be the optimal location for detection. The neck was determined to be the optimal

location for the detection of ^{131}I, though employing the posterior right torso position would also yield sufficient counts for assaying contamination. The neck location was optimal in this case, as iodine is readily metabolized by the thyroid gland.

The lowest count-rate from all the sampled nuclides originates from ^{241}Am. The easily attenuated low-energy gamma-rays (59.5-keV) permit only a small fraction of the gamma-rays to reach the detector, thus resulting in a count-rate per 250-mSv intake of many orders of magnitude lower than the other nuclides. As will be discussed in §5.4, none of the count-rates for ^{241}Am are detectable above the background threshold. Additionally, as seen in Table 4.3.1, the inhalation dose coefficient for ^{241}Am is approximately four orders of magnitude lower than those of the other nuclides, so ^{241}Am requires a low-activity intake to deliver a considerable dose. In the absence of the ability to detect low activities of ^{241}Am, it is quite possible that a considerable dose can be delivered by the time the detector can definitively detect an adequate count-rate above the background detection limit. Consequently, ^{241}Am is considered undetectable by the 2x2-NaI(Tl) detector for inhaled contamination.

The sources of the counts that are being tallied by the detector at each detector location are presented in Figures 5.3.7 through 5.3.10, displaying the count-rate per contributing source organ at three days after inhalation. Note that the FRL and BRL acronyms refer to the anterior and posterior torso locations, respectively.

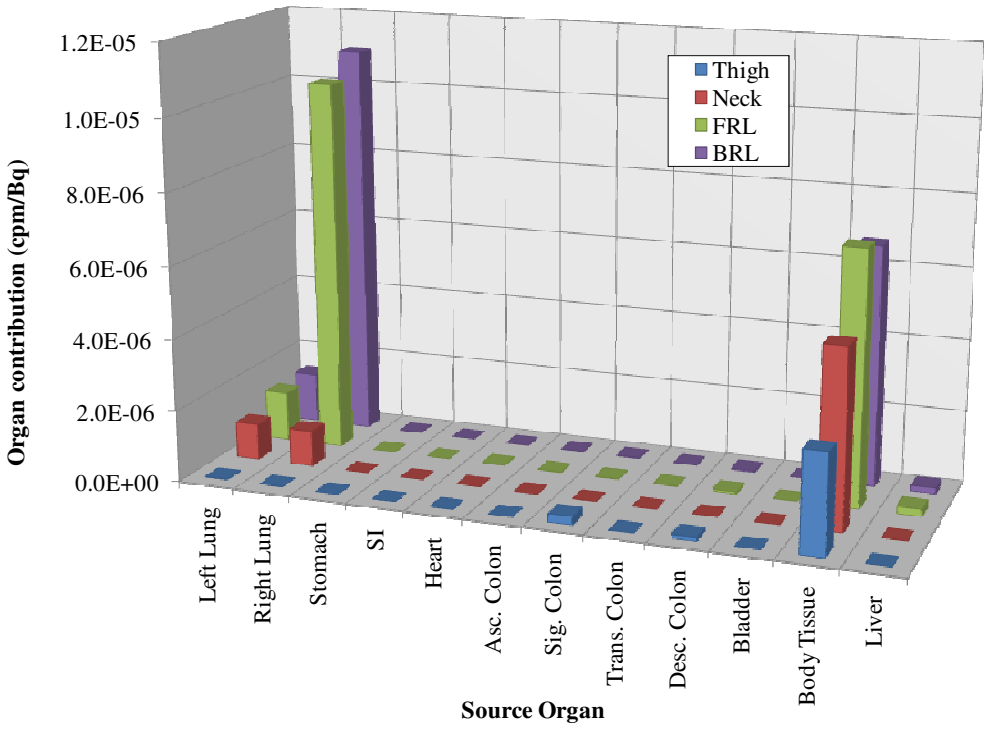

Figure 5.3.7 Reference Male ^{60}Co Count-Rate per Source Organ at 3 Days

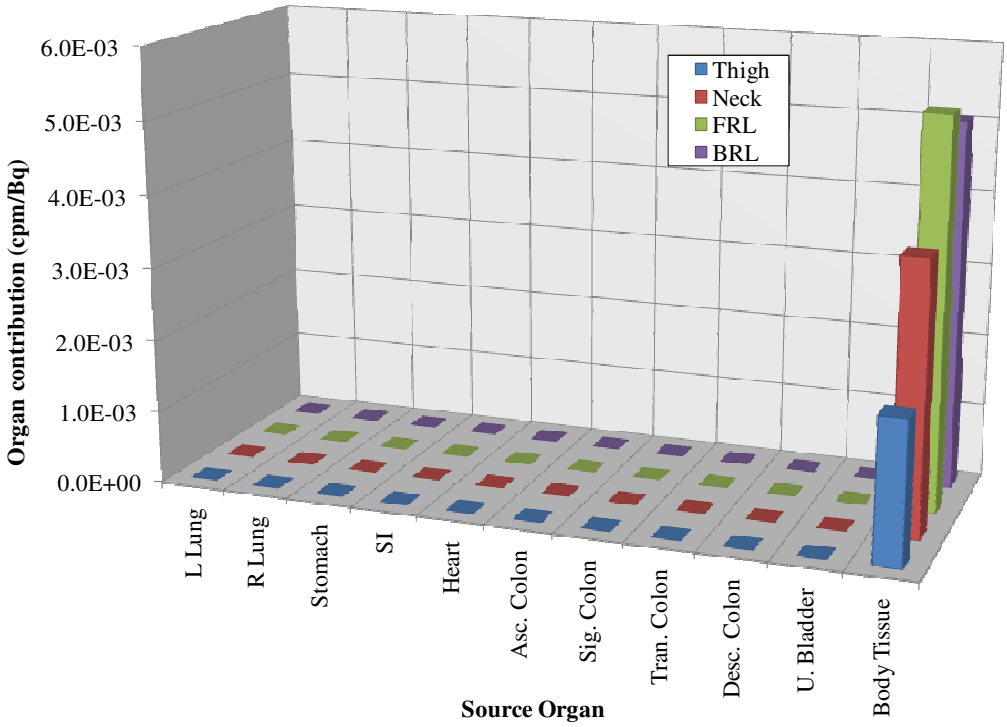

Figure 5.3.8 Reference Male ^{137}Cs Count-Rate per Source Organ at 3 Days

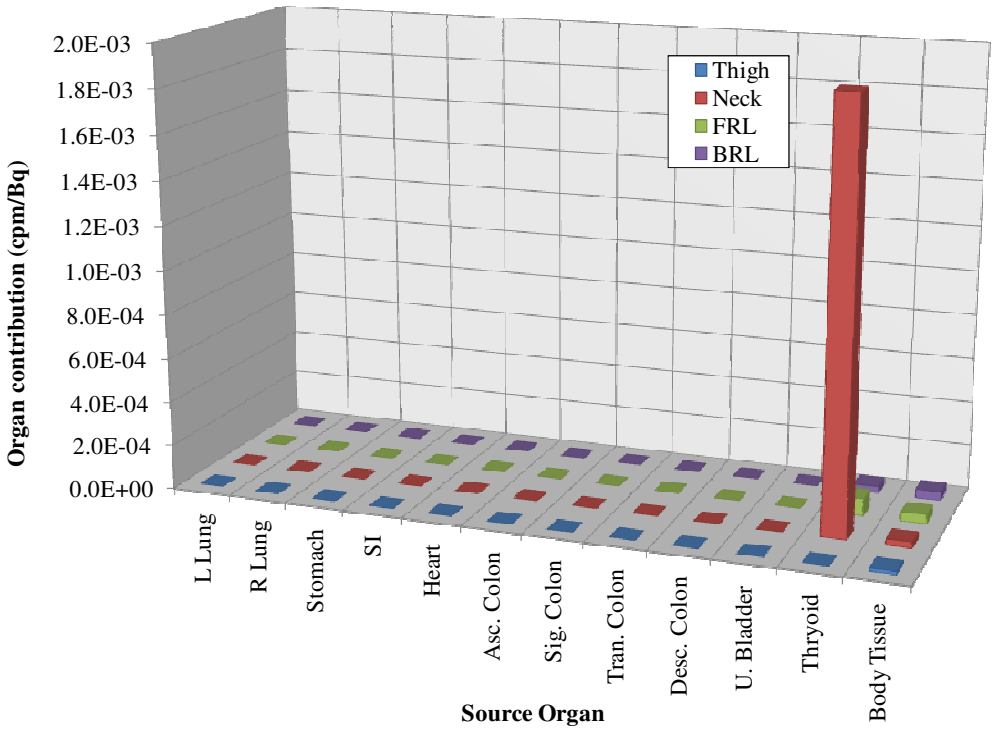

Figure 5.3.9 Reference Male ^{131}I Count-Rate per Source Organ at 3 Days

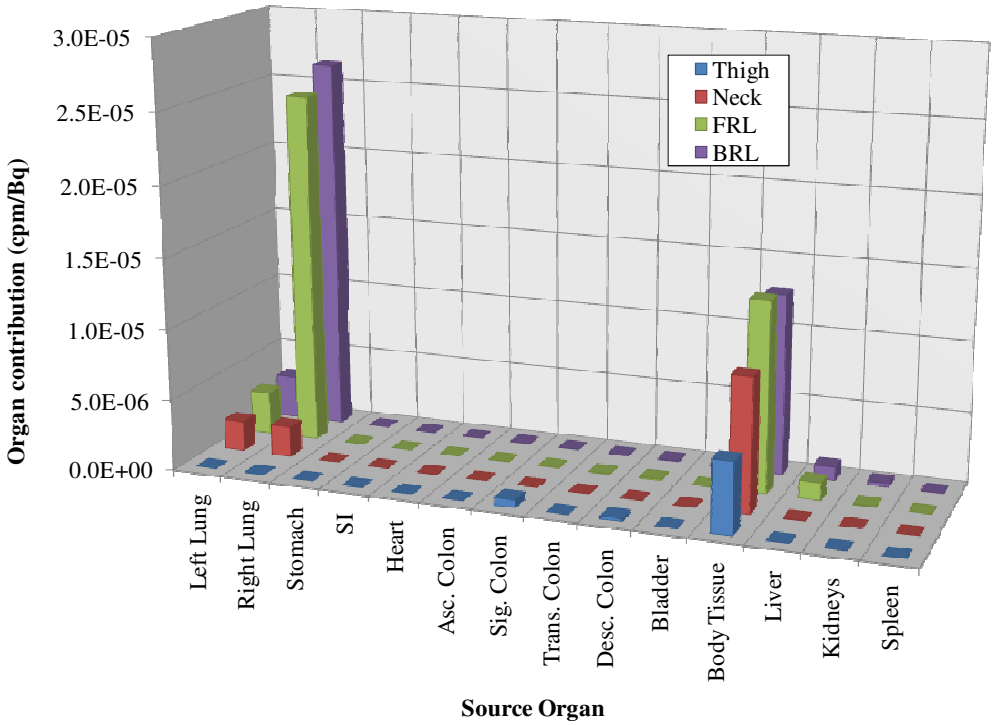

Figure 5.3.10 Reference Male ^{192}Ir Count-Rate per Source Organ at 3 Days

The behavior of ^{137}Cs shows count-rates closely distributed when comparing the phantoms in Figure 5.3.4. The optimal detector location for ^{137}Cs occurs when placed over the lung location, even though the source of these counts results from contaminant movement through the body tissue, not lung retention (fast absorption type), as seen in Figure 5.3.8. In the cases of ^{192}Ir and ^{60}Co, both nuclides have moderate lung absorption types. As seen in Figures 5.3.7 and 5.3.10 (for ^{60}Co and ^{192}Ir, respectively), both tend to receive most of their counts due to contributions from where these nuclides tend to accumulate: the lungs, body tissue, and liver. In the case of detecting ^{131}I with the detector, its optimal counting location is when placed over the anterior neck, where source counts originate from the thyroid (Figure 5.3.9). Yet, the child phantom yields the lowest count rate (Figure 5.3.5) because ^{131}I is rapidly taken up by the thyroid gland and proceeds at a faster metabolic rate in a child. Additionally, ^{131}I has a short radiological half-life of 8.04 days [20].

For the four detectable nuclides, the majority of the counts tend to originate from either the lungs or body tissue. The two detectable nuclides with moderate lung absorptions, ^{60}Co and ^{192}Ir, have a majority of their counts originating from the lungs. Conversely, the nuclides with fast lung absorptions, ^{131}I and ^{137}Cs, a majority of counts originate from the body tissue (with the exception of the thyroid uptake of ^{131}I). This is due to the fact that the fast uptake nuclides are more rapidly clear the lungs into the body, while the moderate uptake nuclides linger for longer in the lungs. As previously mentioned with ^{137}Cs, even though the lung and neck locations yield optimal count-rates (Table 5.3.3), this is not due to retention in the lungs, but due to counts from the inhaled contaminant having metabolized in the body tissue and emitted gammas over these large areas of tissue.

Unlike the 2x2 NaI(Tl) detector, the Thyroid Uptake Probe study by Scarboro, which also employs a 2x2 NaI(Tl) crystal, was able to limit this "shine" from body tissue due to the presence of the lead collimator [15]. Additionally, the subtraction of the ET1 and ET2 compartments from the DCAL calculation was not applied in Scarboro's study, resulting in a higher lung contribution to the total fraction retained. Therefore, both these reasons contribute to why Scarboro's study determined that the anterior neck was the optimal location for detecting ^{137}Cs .With the exception of the ^{137}Cs case, the Scarboro study yielded results consistent with this study (though lower count-rates) in determining the optimal detector locations to detect inhaled contamination.

5.4 Consideration of Minimum Detectable Activity, Dose, and Decision Levels

5.4.1 Decision Levels

Since radioactivity count-rates tend to fluctuate statistically, a minimum threshold must be established to discern a lower limit of detection with confidence above background levels. The Minimum Detectable Activity (MDA) is used to describe the decision level (DL) for a detector counting system in terms of activity. It serves to determine the smallest signal that can be reliably detected above the threshold activity of a background sample. The DL is a method identifying whether or not a sample is above background levels. The MDA measures the detection capability of the counting system, and determines the minimum activity based on a DL. Measurements taken on a blank sample provide an *a priori* estimate of the DL. This estimate, based on background measurements, does not serve as a decision-making mechanism, but rather describes the detection capability and sensitivity of the system. Thus, a DL must be established to determine the net count-rate of a sample above background with a pre-established confidence interval. This DL takes the form of Equation 5.4.1.1 [40].

$$DL = 1.645\sqrt{R_b(\frac{1}{t_b}+\frac{1}{t_g})} \qquad \text{[Equation 5.4.1.1]}$$

In this equation,

DL = decision level (cpm)

R_b = background count rate (cpm)

t_b = background acquisition time (min)

t_g = sample acquisition time (min)

When calculation of the DL is applied to measurements from an actual sample, this *a posteriori* calculation provides an estimate of the activity above the background rate, and varies according to the nuclide to be detected. As seen in Equation 5.4.1.1, the DL is dependent upon the background counting rates, as well as the background and gross sample acquisition times.

Since the DL is dependent on the background rates, it is consequently dependent on the nuclide and the ROI over which the background spectrum is taken. Using the ROIs given in Table 5.1.1, the nuclide-dependent DL above background can be used to determine if real activity is present. These nuclide-dependent decision levels were determined using Equation 5.4.1.1, and are summarized in Table 5.4.1.1 for one-, five-, and ten-minute sample counting times.

Table 5.4.1.1 Minimum Detectable Decision Levels for Various Counting Times for 2x2-NaI(Tl) Detector

Nuclide	Background Rate in ROI (cpm)	Decision Level (Above Background) for Various Acquisition Times (cpm)		
		1 minute	*5 minutes*	*10 minutes*
^{241}Am	728.2	44.5	20.1	14.4
^{60}Co	969.1	51.4	23.2	16.6
^{137}Cs	542.8	38.4	17.4	12.5
^{131}I	1784.8	69.7	31.5	22.6
^{192}Ir	3701.5	100.4	45.4	32.5

As previously mentioned in §5.3, ^{241}Am has been deemed undetectable by the 2x2-NaI(Tl) detector. The order of magnitude of the resulting count-rates from each of the phantoms (summarized in Appendix D) does not exceed 10-cpm. However, as required in Table 5.4.1.1, a count-rate of at least 44.5-cpm above background is required to justify the presence of true activity within 95% confidence intervals. In addition, as previously emphasized, ^{241}Am has a very high inhalation dose coefficient; by the time this count-rate may be met, a severe dose may already have been delivered. In order to adequately detect ^{241}Am, Table 5.4.1 indicates an assay acquisition time well exceeding 10-minutes. However, this condition is very impractical for triaging purposes.

5.4.2 Consideration of Minimum Detectable Activity

This DL estimation is concerned with whether the observed signal is real within a given confidence interval. The DL applied in the MDA calculation corresponds to determining the threshold for a 5% false alarm rate, a common baseline in detection assessments. Consequently, if the net count-rate falls below a DL, it is safe to assume that no real activity is present. The MDA equation governing a 5% false-negative rate is given in Equation 5.4.2.1 [40].

$$MDA = \frac{3 + 3.29\sqrt{R_b t_g (1 + \frac{t_g}{t_b})}}{K t_g} \qquad \text{[Equation 5.4.2.1]}$$

In this equation,

MDA = minimum detectable activity (Bq or μCi)

K = counting efficiency

To reiterate, the MDA should only be used as a performance indicator for a detection system, whereas the DL indicates the presence of true activity in the system.

5.4.3 Minimum Detectable Dose

The Minimum Detectable Dose (MDD) is a quantity useful for assessing the detection capability for a bioassay system. The MDD is proportional to the MDA, and additionally incorporates biological processes and the half-life, as well as the nuclide retention fraction. The MDD is governed by Equation 5.4.3.1 [40].

$$MDD = \frac{MDA}{Y_{RC} V_{bio} IRF_u(\Delta t)} \times h_{E,50} \qquad \text{[Equation 5.4.3.1]}$$

In this equation,

Y_{RC} = radiochemical yield of nuclide

V_{bio} = biological variability in excretion rates and volumes

IRF_u = intake retention fraction

Δt = time between intake and bioassay measurement

$h_{E,50}$ = 50-year committed effective dose equivalent per unit intake

MDA and MDD values were not directly pertinent to the scope of this work and therefore were not calculated. However, the MDA and MDD values scaffold on the calculated DLs, which are sufficient for the scope of the work addressed herein.

5.5 Triaging Procedure Sheets for First Responders

In order to employ these results in a first-responder scenario, a set of procedure sheets were developed to facilitate triaging decisions using the 2x2-NaI(Tl) detector. Such procedure sheets provide a succinct and portable method of communicating how to properly use the detector to assess inhaled contamination, as well as to identify individuals requiring further medical attention based on the count-rates indicating 250-mSv of contamination. A detector location at the posterior right torso position was selected, as this position yields a sufficient count-rate for all the investigated nuclides. Opting for a single detector location, regardless of the nuclide in question, is convenient as it eliminates operator error in detector placement for different nuclides. A procedure sheet was created for each of the six anthropomorphic phantom body types and contained in each sheet was a summary of all the four detectable nuclides of concern. A sample of the triage procedure sheet for the Reference Male phantom is given in Appendix D.

Each procedure sheet contains five sections instructing the operator in the use of the 2x2-NaI(Tl) detector for triage screening. The first section includes a photograph of the detector, such that an operator is able to identify the instrument. The second section includes basic information on the operation of the detector, as well as how to set-up ROIs depending on the interrogated nuclide. The third section instructs the operator how to take a background measurement using the instrument, and how to determine a count-rate in cpm.

The fourth section instructs the operator on how to obtain a gross count-rate using the posterior right torso position, and how to convert this into a net count-rate by subtracting background. A decision level of 100-cpm was set as the detection threshold for all radionuclides

(based on Table 5.4.4.1), in order to establish a conservative identification of true activity. In addition to detection thresholds, in order to mitigate some of the summation and pile-up effects mentioned in §5.2, an upper dead-time limit for detection was additionally outlined as a secondary method to assess the limitations of the detector system. These dead-time thresholds were obtained by analyzing the resulting dead-time for high count-rates. These dead-time thresholds were based on the highest expected count-rate per nuclide from the Tables in Appendix C. Therefore, dead-time can also be used as an auxiliary indicator of activity incident on the detector, though this quantity is certainly dependent on the individual detector, as well as source-detector geometry.

Finally, the fifth section contains a table of the action levels (net count-rate) for each nuclide. The data has been presented for each detectable nuclide in counts-per-minute corresponding to 250-mSv of contamination as the triage threshold. Procedure sheets were created for each of the six anthropomorphic body types with a summary of all four of the detectable nuclides of concern.

In order to further optimize the triaging procedure using the instructional sheets, Manger's analysis for triage with Geiger-Mueller counters [41] has recommended that it may be prudent to combine all the adult phantoms into a single category. Determining the body type that best suits a triage patient is highly subjective and introduces a strong element of operator error. Discerning a Pre-Menopausal from a Post-Menopausal Adipose Female, for example, is intrusive and time consuming. Thus, such semantics can be avoided if the adults were collected into a single adult class, utilizing the most conservative phantom's data set (Adipose Male) for the posterior lung position. This adds additional elements of safety, as the most conservative triaging thresholds are employed, thus reducing the probability of false negatives for most of the adult

phantoms. Ultimately, the operator is left only to decide if the triage patient is an adult or child. Applying this procedure reduces the need for six triage procedure sheets into a single consolidated sheet containing the conservative adult (Adipose Male) counting thresholds, as well as those of the child. The condensed triage procedure sheet is given in Appendix E.

CHAPTER 6: CONCLUSIONS

The 802-2x2-Na(Tl) detector is capable of assaying individuals having inhaled contamination for triage purposes if exposed to an RDD. The detector is capable of assaying the four of the five nuclides investigated: ^{60}Co, ^{137}Cs, ^{131}I, and ^{192}Ir. However, ^{241}Am did not meet minimum detection thresholds to ensure true count-rates were present for at least 250-mSv of contamination, and consequently cannot be detected by 2x2-NaI(Tl) detectors. The easily attenuated low energy gamma-rays emitted by ^{241}Am, as well as its high dose coefficient, make it difficult to detect.

In the event that the 2x2-NaI(Tl) detector needed to be employed in an emergency scenario by first responders, it is recommended that more time be dedicated to identifying and counting the contaminant, rather than applying demographics to associate the patient with the appropriate phantom body-type. Placing the detector at the posterior right torso position yields sufficient, if not optimal, counts for all the nuclides investigated. Using the most conservative count-rate from the phantoms at this detector location would provide a simple and conservative estimate of contamination, while eliminating human decision-making errors by the operator when attempting to determine body-type or detector location. In this respect, using the most conservative count-rates at the optimal detector location would involve using the posterior right torso position for the Adipose Male. The Child phantom count-rates at the posterior right torso position may be employed for children to satisfy the distinct variation in body type from the adult phantoms.

For a threshold contamination of 250-mSv, a minimum counting time of one-minute is sufficient in discerning true activity above background for each of the four detectable nuclides.

Yet, given the complex nature of the instrument and the calibration required, it is strongly recommended that trained personnel with experience using sodium-iodide detectors conduct the set-up before and conduct supervision during use by first responders. The detector itself is not hand-portable, and requires the set-up of modules, energy calibrations, and ROI determination. Therefore, only with the assistance technical personnel experienced in operating sodium-iodide detectors is the 2x2-NaI(Tl) is feasible for triaging individuals exposed to an RDD. Yet, although the sodium-iodide is amply capable of doing so, it is the recommendation of this study that it is not to be used if given more easily operable detector alternatives. Sensitivity, detector set-up, summation coincident events, and pulse pile-up all become prominent issues best dealt with in a laboratory, rather than a field setting. These detectors are not intuitive, even with operation by experienced personnel. Field conditions will likely complicate the data acquisition and analysis process, as multiple data acquisitions were required to obtain the slab benchmark measurements in a controlled laboratory setting. Recommendations made in the next section for future work will mitigate the complexities when operating a sodium-iodide detector.

CHAPTER 7: FUTURE WORK

Given the concerns mentioned in the previous section, future work must be dedicated towards making the sodium-iodide detector more user-friendly. Thus, it is recommended that an independent software platform be created that is capable of processing background spectra data inputs, and even manual entry of the ROI for the nuclide of interest. Based on such information, assay data can be fed into a graphical-user interface and return a computed result, even of a Boolean "contaminated"/"not contaminated" nature, thus reducing operator error. Although companies such as Canberra offer their own detection software like Genie, it would be advisable to develop an independent graphical interface that may work in conjunction with the data obtained using the manufacturer's software. This is a very feasible solution that would greatly increase the accessibility and usability of this detector instrument.

Further work using the NaI(Tl) detector can be focused on investigating the effects if more than one radionuclide (combination) was to be inhaled by a patient. Sodium-iodide detectors are customizable spectrometers that would be optimal in such a scenario, as a spectrometer is capable of isolating different ROIs, and thus determining each nuclide's contribution with inhalation dose coefficients. Investigating these summed effects of multiple inhaled contaminants would be an additional strong study of interest.

Finally, future work must be focused on developing a method to detect ^{241}Am. The inability to detect this nuclide, in conjunction with its high dose coefficient and ability to deliver a high dose at a low activity, is of imminent concern. Further investigating the capabilities of the sodium-iodide detector using longer counting times or alternative methods is suggested, as well as developing an alternative detection method to reliably detect ^{241}Am, in general, is paramount.

APPENDIX A: MCNP INPUT FILE FOR SLAB PHANTOM

```
NaI 2x2 Model of PMMA Slabs, Virtual Water, and Detector
C Cell Cards
1 4 -3.667          -5          imp:p=1          $ NaI Crystal
2 9 -.55            5 -10       imp:p=1          $Al2O3
3 1 -2.94           10 -11      imp:p=1          $Al Window
4 3 -0.93           11 -9       imp:p=1          $Foam
5 2  -0.94          -3          imp:p=1          $ PMT Glass
6 0           -2 9 10 11 3      imp:p=1          $ PMT Vacuum
7 1  -2.94   -98 -1 2 9 10 11   imp:p=1          $ Al Casing
8 5  -1.19          -6          imp:p=1          $ PMMA in front of source
9 8 -1              -4  6       imp:p=1          $Source
10 5  -1.19     4 -7     imp:p=1                 $ PMMA with source
11 6  -1.03     -8       imp:p=1                 $Virtual water behind source
12 7  -1.293e-3  -98 1 6 7 8     imp:p=1          $ Air Environment
13 0            98              imp:p=0          $Universe

C Surface Cards
1 RCC    0      0     0    -18.41 0     0    2.94    $ Al Casing
2 RCC   -0.2    0     0    -18.01 0     0    2.74    $ PMT Vacuum
9 RCC   -0.2    0     0    -.2    0     0    2.74     $ Foam
11 RCC  -.4     0     0    -.05   0     0    2.74     $ Al Window
10 RCC  -.45    0     0    -5.26  0     0    2.74    $ Al2O3
5 RCC   -.61    0     0    -5.1       0     0    2.55          $ NaI Crystal
3 RCC   -5.71   0     0    -0.3       0     0    2.74          $ 0.3cm PMT Glass
4 RCC   0.8    -1.15  0     0        2.3   0     .2           $ Source
6  RPP   0.0     0.6  -15.3   15.3  -15.2   15.2             $ PMMA in front of source
7  RPP   0.6     1.2  -15.3   15.3  -15.2   15.2             $ PMMA with source
8  RPP   1.2    11.2  -15.3   15.3  -15.2   15.2             $ Virtual water
98 RPP   -50     50   -50     50    -50     50      $ Air Environment

C Data Cards
C
C Material Cards
C
C Al Casing
m1 13027 1
C Low Density Glass
m2 14000 0.3333 8016 0.6667
C Foam + 0.01 g/cc
m3 1001 0.6667 6000 0.3333
C NaI Crystal 2X2
m4 11000.04p 0.5 53000.04p 0.5
C m4 11023 0.5 53127 0.5
C PMMA
m5 6000 0.3333 8016 0.1333 1001 0.5334
C Virtual Water
m6 1001 0.0802 6000 0.6748 7015 0.0214 8016 0.1991 &
   17000 0.0014 20000 0.0231
C Air
m7 8016 -0.2314 7014 -0.7558 18000 -0.0128
C Polyester for Sources
m8 6000 0.333 1001 0.533 8016 0.133
C Al2O3
m9 13027 0.4 8016 0.6
C
C Source Cards
```

```
C
SDEF par=2 rad=d1 pos=0.8 0.0 0.0 axs=0 1 0 vec=0 0 1 erg=d3 ext=d2
SI1 0 0.2
SP1 -21 1
SI2 -1.15 1.15
SP2 -21 0
C
C Cs-137 0.662MeV
SI3 l 0.661645
SP3 0.851
C
C SI3 l 0.834827
C SP3   0.99976
C
C Tally Cards
C
F8:p 1 $ Tally over NaI Crystal
fc8 F8 tally no GEB
F18:p 1
fc18 F8 tally with GEB
C
C Energy Bins
C
E0 0 1e-8 .000876 1020i 3.243776 $1022 Channels
C
C Gaussian Energy Broadening
C
FT18 GEB -0.00715076 0.0652825 -0.178934 $ GEB Values
C
phys:p 4j 1
mode p
print
nps 5e7
```

APPENDIX B: MCNP INPUT FILE FOR ANTHROPOMORPHIC PHANTOM

```
Male With Cs-137
1    1 -.001293    -1 (607:-37:606) (-606:601:35) (600:-35) &
                (-615:37:-43:44:4:-616) (37:-608:609) &
                (37:-608:610) 900 901 902 903
2    2 -0.2958     ((-2 -4 3):(-2 4)) 5                    $ left lung
3    3 -0.9869     -7 51 -6 (-8:32) 84 101 #2 #24 #28 #58 #59
                (113:115) (114:115) #62 #700                $ torso insd ribs/lvrtop-shldr
4    3 -0.9869     -7 8 -32 117 113 114 #15 #16 #17 #18 #19 #20 #700
                (-4:-9:116:118:-119) (-4:-9:116:120:-121)    $torso
5    3 -0.9869     -7 8 -117 51 113 114 #9 #13 #14 #700      $ torso
6    3 -0.9869     -7 50 -51 56 84 96 105 106 113 114 #10 #11 #12
                #27 #32 #43 #44 #47 #700                    $ torso
7    3 -0.9869     -7 97 -50 (83:-86:87:-88) 113 114 #30 #33 #38 #39
                #63 #64 #65 #700                            $ torso abdomen
8    3 -0.9869     -7 37 -97 95 113 114 #31 #33 #38 #65 #66 #700    $ torso abdomen
9    4 -1.4862     8 -9 5 -10                              $ rib
10   4 -1.4862     8 -9 11 -12                             $ rib
11   4 -1.4862     8 -9 13 -14                             $ rib
12   4 -1.4862     8 -9 15 -16                             $ rib
13   4 -1.4862     8 -9 17 -18                             $ rib
14   4 -1.4862     8 -9 19 -20                             $ rib
15   4 -1.4862     8 -9 21 -22                             $ rib
16   4 -1.4862     8 -9 23 -24                             $ rib
17   4 -1.4862     8 -9 25 -26                             $ rib
18   4 -1.4862     8 -9 27 -28                             $ rib
19   4 -1.4862     8 -9 29 -30                             $ rib
20   4 -1.4862     8 -9 31 -32                             $ rib
21   3 -0.9869     ((35 -34):(-33 6 -35)) 102 (84:85)
                #37 #60 #61 #62 #700                        $ head
22   3 -0.9869     -37 38 -39 103 #700                       $ left leg
23   3 -0.9869     -37 38 -40 104 #22 #700                   $ right leg
24   2 -0.2958     ((-41 -4 42):(-41 4)) 5                   $ right lung
25   3 -0.9869     715 -37 43 -44 -4 716 39 40 72 73 #700 #600    $ genitalia
26   3 -0.9869     -47                                     $ brain
27   3 -0.9869     50 -51 -48 -49 #10 #11 #12                $ liver
28   3 -0.9869     (-52 54):(-53 -54 55)                     $ heart
29   3 -0.9869     -56                                     $ stomach
30   3 -0.9869     138 -57 58 -59                          $ Ascending Colon Wall
31   3 -0.9869     (-63 141 65 -61):(-64 142 37 -65)         $ Sigmoid Colon Wall
32   3 -0.9869     -62 139 66 -67 59                       $ Transverse Colon Wall
33   3 -0.9869     -60 140 61 -59 -83                      $ Descending Colon Wall
35   3 -0.9869     -72                                     $ testicle
36   3 -0.9869     -73                                     $ testicle
37   3 -0.9869     -74 75 -76 6 -77                        $ thyroid
38   4 -1.4862     -82 83 37 -78 80 (79:-81)                 $ pelvis
39   4 -1.4862     -84 78 -85 102                          $ spine
40   3 -0.9869     -83 86 -50 88 -87 #30 #32 #33 #63 #64 #65    $ small int.
41   1 -0.001293   -107 606 -4                             $ air
42   1 -0.001293   -108 606 -4                             $ air
43   3 -0.9869     -92 65                                  $ kidney
44   3 -0.9869     -93 -94                                 $ kidney
45   3 -0.9869     -95                                     $ bladder
46   3 -0.9869     -96                                     $ spleen
47   3 -0.9869     -98 99 (-65:100)                        $ pancreas
48   3 -0.9869     -101                                    $ thymus
49   4 -1.4862     47 -102 #60 #61                         $ skull
```

```
50    4 -1.4862     -103 38 -37                                  $ leg bone
51    4 -1.4862     -104 38 -37                                  $ leg bone
52    3 -0.9869     -105 92                                    $ adrenal
53    3 -0.9869     -106 93                                    $ adrenal
54    4 -1.4862     37 -115 -113                                 $ arm bone
55    4 -1.4862     37 -115 -114                                 $ arm bone
56    4 -1.4862     4 9 -32 -116 117 -118 119                        $ scapulae
57    4 -1.4862     4 9 -32 -116 117 -120 121                        $ scapulae
58    4 -1.4862     -4 -122 -123 124                             $ clavicle
59    4 -1.4862     -4 -122 -125 126                             $ clavicle
60    3 -0.9869     -33 128 129 -130 133 -134 -4 #700                $ eye lens
61    3 -0.9869     -33 128 -131 132 133 -134 -4 #700                $ eye lens
62    3 -0.9869     -77 -137 51                                $ esophagus
63    3 -0.9869     -138 58 -59                                $ Ascending Colon Interior
64    3 -0.9869     -139 66 -67                                $ Transverse Colon Interior
65    3 -0.9869     -140 61 -59 -83                              $ Descending Colon Interior
66    3 -0.9869     (-141 65 -61) : (-142 37 -65)                    $ Sigmoid Colon Interior
600   0           -600 35 34 902 : -601 33 -35 606 902 : &             $ Head & Neck
                  -606 6 33 -607 902: -607 7 -6 37 900 901 902 : &   $ Shoulders & Torso
  (((-46 616) (43 -44) (615 -37)):((615 -45)(610 609)(46 -4)(43 -44))): & $ Genitalia
                  -610 40 -37 38 : -609 39 -37 38 903: &              $ Legs
                  -708 608 -609 : -708 608 -610 : &                $ Feet
                  -38 708 -610 40 : -38 708 -609 39
700   5 -1.04       700 35 102 -34 : 701 -33 -35 6 : &                $ Head & Neck
                  706 -6 701 -707 : 707 -7 -6 37 114 113 : &          $ Shoulders & Torso
  (((46 -716)(43 -44)(609 610)(715 -37)):((-715 45)(610 609)(46 -4)(43 -44))): & $ Genitalia
                  -40 710 -37 38 : -39 709 -37 38 : &                $ Legs
                  -38 708 -39 : -38 708 -40                        $ Feet
900   1 -.001293    -900 7 501
901   1 -.001293    -901 7 511
902   1 -.001293    -902 6 33 34 521
903   1 -.001293    -903 39 531
c Detector in box 900 NaI 2x2
c Detector in box 900 NaI 2x2
501 504 -3.667  -505                        $ NaI Crystal
502 509 -.55     505 -507                    $ Al2O3
503 501 -2.94    507 -506                    $ Al Window
504 503 -0.93    506 -509                    $ Foam
505 502 -0.94   -503                        $ PMT Glass
506 0          -502  509  507  506  503         $ PMT Vacuum
507 501 -2.94   -900 -501  502  509  507  506     $ Al Casing
c Detector in box 901
511 504 -3.667  -515                        $ NaI Crystal
512 509 -.55     515 -517                    $ Al2O3
513 501 -2.94    517 -516                    $ Al Window
514 503 -0.93    516 -519                    $ Foam
515 502 -0.94   -513                        $ PMT Glass
516 0          -512  519  517  516  513         $ PMT Vacuum
517 501 -2.94   -901 -511  512  519  517  516     $ Al Casing
c Detector in box 902
521 504 -3.667  -525                        $ NaI Crystal
522 509 -.55     525 -527                    $ Al2O3
523 501 -2.94    527 -526                    $ Al Window
524 503 -0.93    526 -529                    $ Foam
525 502 -0.94   -523                        $ PMT Glass
526 0          -522  529  527  526  523         $ PMT Vacuum
```

```
527 501 -2.94   -902 -521  522  529  527  526     $ Al Casing
c Detector in box 903
531 504 -3.667  -535                          $ NaI Crystal
532 509 -.55     535 -537                      $ Al2O3
533 501 -2.94    537 -536                      $ Al Window
534 503 -0.93    536 -539                      $ Foam
535 502 -0.94   -533                          $ PMT Glass
536 0          -532  539  537  536  533          $ PMT Vacuum
537 501 -2.94   -903 -531  532  539  537  536     $ Al Casing
67    0            1

1     SO  200
2     SQ  23.04 10.24 1 0 0 0 -576 8.5 0 43.5
3     SQ  23.04 10.24 1 0 0 0 -576 2.5 0 43.5
4     PY  0.0
5     PZ  43.5
6     PZ  70
706   PZ  69.8
606   PZ  70.2
7     SQ  1 4.0 0 0 0 0 -400.0 0 0 0
707   SQ  0.002551 0.010412 0 0 0 0 -1 0 0 0
607   SQ  0.002451 0.00961  0 0 0 0 -1 0 0 0
8     SQ  1 3.15 0 0 0 0 -272.25 0 0 0
9     SQ  1 3.01 0 0 0 0 -289.0 0 0 0
10    PZ  44.9
11    PZ  35.1
12    PZ  36.5
13    PZ  37.9
14    PZ  39.3
15    PZ  40.7
16    PZ  42.1
17    PZ  46.3
18    PZ  47.7
19    PZ  49.1
20    PZ  50.5
21    PZ  51.9
22    PZ  53.3
23    PZ  54.7
24    PZ  56.1
25    PZ  57.5
26    PZ  58.9
27    PZ  60.3
28    PZ  61.7
29    PZ  63.1
30    PZ  64.5
31    PZ  65.9
32    PZ  67.3
33    SQ  100 49 0 0 0 0 -4900 0 0 0
701   SQ  0.021626 0.010412 0 0 0 0 -1 0 0 0
601   SQ  0.01929 0.009612 0 0 0 0 -1 0 0 0
34    SQ  7225 3540.25 4900 0 0 0 -354025 0 0 85.5
700   SQ  0.021626 0.010412 0.014516 0 0 0 -1 0 0 85.5
600   SQ  0.01929 0.009612 0.013212 0 0 0 -1 0 0 85.5
35    PZ  85.5
36    PZ  94
37    PZ  0
```

```
38    PZ  -80
708   PZ  -80.215
608   PZ  -80.415
39  601  GQ  5.025 5 0 0 0 -1 -100 0 0 0
709 603  GQ  5.05 5 0 0 0 -1 -100 0 0 0
609 605  GQ  4.963 5 0 0 0 -1 -100 0 0 0
40  600  GQ  5.025 5 0 0 0 1 100 0 0 0
710 602  GQ  5.089 5 0 0 0 1 100 0 0 0
610 604  GQ  4.963 5 0 0 0 1 100 0 0 0
41    SQ  23.04 10.24 1 0 0 0 -576 -8.5 0 43.5
42    SQ  23.04 10.24 1 0 0 0 -576 -2.5 0 43.5
43    P   10 0 1 -100
44    P   10 0 -1 100
45    PZ  -4.8
715   PZ  -4.6
615   PZ  -5.0
46    P   0 10 1 -100
716   P   0 10.2 1 -100
616   P   0 9.8 1 -100
47    SQ  2.25 1 1.91716 0 0 0 -81 0 0 86.5
48    SQ  64 272.25 0 0 0 0 -17424 0 0 0
49    P   9 7 -7.3256 -315
50    PZ  27
51    PZ  43
52    GQ  45.2 59.9 47.9 17.5 -16.2 34.8 -1632.1 1204.8 -4898.2 124295.2
53    SQ  1 1 1 0 0 0 -25 -1 -3 51
54    P   .6943 -.3237 -.6428 -32.506
55    P   5.2193 -2.4336 -0.916 -59.6345
56    SQ  4 7.11 1 0 0 0 -64 8 -4 35
57    SQ  1 1 0 0 0 0 -6.25 -8.5 -2.36 0
58    PZ  14.45
59    PZ  24
60    GQ  4.54 3.53 .096 0 1.16 -0.166 -77.68 -10.08 -.223 323.52
61    PZ  8.72
62    SQ  0 2.25 6.25 0 0 0 -14.0625 0 -2.36 25.5
63    TY  3 0 8.72 5.72 1.57 1.57
64    TY  3 0 0 3 1.57 1.57
65    PX  3
66    PX  -10.5
67    PX  10.5
68    PX  -20
69    PX  20
70    PY  -30
71    PY  -29
72    SQ  11.9025 8.9401 3.8025 0 0 0 -20.115225 1.3 -8 -2.3
73    SQ  11.9025 8.9401 3.8025 0 0 0 -20.115225 -1.3 -8 -2.3
74    C/Z 0 -6 2.2
75    C/Z 0 -6 1
76    PY  -6
77    PZ  75
78    PZ  22
79    PZ  14
80    PY  -3
81    PY  5
82    C/Z 0 -3 12
83    C/Z 0 -3.8 11.3
```

```
84   SQ  6.25 4 0 0 0 0 -25 0 5.5 0
85   PZ  78.5
86   PZ  17
87   PY  2.2
88   PY  -4.86
89   C/Z 0 -11. 0.6350
90   C/Z 0 -11. 0.8636
91   PZ  56.335
92   SQ  1.49 13.44 1 0 0 0 -30.25 6 6 32.5
93   SQ  1.49 13.44 1 0 0 0 -30.25 -6 6 32.5
94   PX  -3
95   SQ  1 2.0557 2.0557 0 0 0 -24.5818 0 -4.5 8
96   SQ  2.94 9 1 0 0 0 -36 11 3 37
97   PZ  12
98   SQ  1 225 25 0 0 0 -225 0 0 37
99   PX  0
100  PZ  37
101  SQ  1.78 64 1 0 0 0 -16 -2 -6 60.5
102  SQ  2.08 1 1.39 0 0 0 -96.04 0 0 85.5
103  GQ  1 1 .0091 0 0 -.2005 -20 0 1.7857 87.75
104  GQ  1 1 .0091 0 0 .2005 20 0 1.7857 87.75
105  SQ  100 900 9 0 0 0 -225 4.5 6.5 38
106  SQ  100 900 9 0 0 0 -225 -4.5 6.5 38
107  SQ  1.39 .5 2 0 0 0 -70 -6.5 -3 50
108  SQ  1.39 .5 2 0 0 0 -70 6.5 -3 50
109  PX  17
110  PX  6
111  PX  -6
112  PX  -17
113  GQ  503.01 135.24 0 0 0 10.206 -19215 0 -202.0788 183257
114  GQ  503.01 135.24 0 0 0 -10.206 19215 0 -202.0788 183257
115  PZ  69
116  SQ  1 3.7589 0 0 0 0 -361 0 0 0
117  PZ  50.9
118  P   0.25 -1 0 0
119  P   0.8 -1 0 0
120  P   -0.25 -1 0 0
121  P   -0.8 -1 0 0
122  TZ  0 11.1 68.25 20 0.7883 0.7883
123  P   0.89415 1 0 11.1
124  P   7.0342 1 0 11.1
125  P   -0.89415 1 0 11.1
126  P   -7.0342 1 0 11.1
C    2 concentric elliptical cylinders and planes to define eye lenses
127  SQ  100 64 0 0 0 0 -6400 0 0 0
128  SQ  88.36 40.96 0 0 0 0 -3619.2256 0 0 0
129  PX  2
130  PX  4
131  PX  -2
132  PX  -4
133  PZ  82.5
134  PZ  84.5
C    segmenting planes for RBM regions in leg and arm bones
135  PZ  -22.8
136  PZ  52.6
C    Esophagus
```

```
137   SQ 0.16 1.0 0 0 0 0 -0.16 0.5 2.5 0                    $ Esophagus Exterior
C     Colon Wall
138   SQ 1 1 0 0 0 0 -3.209 -8.5 -2.36 0                     $ Ascending Colon Interior
139   SQ 0 0.9467 3.8927 0 0 0 -3.6854 0 -2.36 25.5
140   GQ 1.796 2.496 0.0674 0 0.818 -0.066 -30.75 -7.12 -0.602 132.2
141   TY 3 0 8.72 5.72 0.91 0.91                          $ Upper Sigmoid Interior
142   TY 3 0 0 3 0.91 0.91                                $ Lower Sigmoid Interior
C Boxes for Detectors
900 900 BOX 0.39 10.9607 38.36   -17.78 0 0 &
      0 50.8 0      0 0 17.78
901 901 BOX 0.39 -10.9609 38.35  -17.78 0 0 &
      0 -50.8 0     0 0 17.80
902 BOX -8.89 -10 70.01  17.78 0 0  0 -50.8 0   0 0 17.78
903 903 BOX 19.98 -8.89 0  50.8 0 0  0 17.78 0  0 0 -17.78
c
c c
c Detector in Box 900
c c
c
C Surface Cards
501 501 RCC    0    0   0    -18.41 0   0    2.94  $ Al Casing
502 501 RCC   -0.2  0   0    -18.01 0   0    2.74  $ PMT Vacuum
509 501 RCC   -0.2  0   0    -0.2   0   0    2.74  $ Foam 0.2cm
506 501 RCC   -0.4  0   0    -0.05  0   0    2.74  $ Al Window
507 501 RCC   -0.45 0   0    -5.26  0   0    2.74  $ Al2O3 0.16cm
505 501 RCC   -0.61 0   0    -5.1   0   0    2.55  $ NaI Crystal
503 501 RCC   -5.71 0   0    -0.3   0   0    2.74  $ 0.3cm PMT Glass
c
c c
c Detector in Box 901
c c
511 502 RCC    0    0   0    -18.41 0   0    2.94  $ Al Casing
512 502 RCC   -0.2  0   0    -18.01 0   0    2.74  $ PMT Vacuum
519 502 RCC   -0.2  0   0    -0.2   0   0    2.74  $ Foam 0.2cm
516 502 RCC   -0.4  0   0    -0.05  0   0    2.74  $ Al Window
517 502 RCC   -0.45 0   0    -5.26  0   0    2.74  $ Al2O3 0.16cm
515 502 RCC   -0.61 0   0    -5.1   0   0    2.55  $ NaI Crystal
513 502 RCC   -5.71 0   0    -0.3   0   0    2.74  $ 0.3cm PMT Glass
c
c c
c Detector in Box 902
c c
c
521 503 RCC    0    0   0    -18.41 0   0    2.94  $ Al Casing
522 503 RCC   -0.2  0   0    -18.01 0   0    2.74  $ PMT Vacuum
529 503 RCC   -0.2  0   0    -0.2   0   0    2.74  $ Foam 0.2cm
526 503 RCC   -0.4  0   0    -0.05  0   0    2.74  $ Al Window
527 503 RCC   -0.45 0   0    -5.26  0   0    2.74  $ Al2O3 0.16cm
525 503 RCC   -0.61 0   0    -5.1   0   0    2.55  $ NaI Crystal
523 503 RCC   -5.71 0   0    -0.3   0   0    2.74  $ 0.3cm PMT Glass
c c
c Detector in Box 903
c c
c
531 504 RCC    0    0   0    -18.41 0   0    2.94  $ Al Casing
532 504 RCC   -0.2  0   0    -18.01 0   0    2.74  $ PMT Vacuum
```

```
539 504 RCC   -0.2  0   0    -0.2   0   0    2.74  $ Foam 0.2cm
536 504 RCC   -0.4  0   0    -0.05  0   0    2.74  $ Al Window
537 504 RCC   -0.45 0   0    -5.26  0   0    2.74  $ Al2O3 0.16cm
535 504 RCC   -0.61 0   0    -5.1   0   0    2.55  $ NaI Crystal
533 504 RCC   -5.71 0   0    -0.3   0   0    2.74  $ 0.3cm PMT Glass

C Data Cards
tr600 -0.1
tr601 0.1
tr602 -0.15
tr603 0.15
tr604 -0.051
tr605 0.051
tr900 0 -0.2 0 0.973527 0.228573 0 -0.228573 0.973527 0 0 0 1
tr901 0 0.2 0 0.973527 -0.228573 0 0.228573 0.973527 0 0 0 1
tr903 -0.35 0 0 0.979903 0 -0.199474 0 1 0 0.199474 0 0.979903
tr501 -10.5 8.75 47.5 0.229 -0.973 0 -0.973 -0.229 0 0 0 1
tr502 -10.5 -8.75 47.5 0.229 0.973 0 0.973 -0.229 0 0 0 1
tr503 0 -10.03 78.88 0 1 0 1 0 0 0 0 1
tr504 17.55 0 -12.5 -0.979903 0 -0.199474 0 1 0 0.199474 0 0.979903
C VOL   0 9.89817E3 5.12539E4 7.01171E3 4.12839E3 3.75367E4 4.1204E4 &
C      3.96266E4 3.42787E2 3.43057E2 3.41728E2 3.41505E2 3.3914E2 &
C      3.38905E2 3.37704E2 3.38854E2 3.36585E2 3.35548E2 3.34261E2 &
C      3.3525E2 1.09049E4 5.26806E4 5.19336E4 9.87788E3 8.35231E2 &
C      8.24983E3 1.08532E4 3.48665E3 2.39203E3 5.46974E2 4.19631E2 &
C      7.21861E2 5.2306E2 1.1077E2 1.11655E2 1.72154E2 3.63227E3 &
C      5.17342E3 6.31233E3 0 0 8.49751E2 8.55366E2 1.48895E3 1.04544E3 &
C      3.58882E2 1.45325E2 4.77509E3 8.25008E3 8.23095E3 5.80561E1 &
C      5.70516E1 2.81453E3 2.80523E3 5.80932E2 5.89508E2 1.56404E2 &
C      1.56141E2 1.09588E1 1.10836E1 2.31698E2 5.781E2 7.58053E2 &
C      6.152E2 2.15848E2 1.23531E4 1.09131E4 1.6059E4 1.6059E4 &
C      1.6059E4 1.6059E4 23.9241 9.2379 53.9171 10.2532 28.10780 &
C      23.9241 9.2379 53.9171 10.2532 28.1078 23.9241 9.2379 53.9171 &
C      10.2532 28.1078 23.9241 9.2379 53.9171 10.2532 28.1078 0
IMP:P 1 98R 0
C
C Sources
SDEF  PAR=2  ERG=D1  CEL=D2  RAD=fcel=D3  &
     POS=fcel=D4  EXT=fcel=D5  AXS=fcel=D6
SI1 L 0.662 0.0332 0.0318
SP1 0.898 0.0392 0.0213
C Left Lung, Right Lung, Stomach, Small Int., Heart, Ascending Colon,
C Sigmoid Colon, Transvers Colon, Descending Colon, Bladder,
C Body Tissue (3, 4, 5, 6, 7, 8, 21, 22, 23, 25)
SI2 L 2 24 29 40 28 30 31 32 33 45 3 4 5 6 7 8 21 22 23 25
SP2 D 1 1  1  1  1  1  1  1  1  1  1 1 1 1 1 1 1 1  1  1
DS3 S 7 8 9 10 11 12 13 14 15 16 17 18 19 20 21 22 23 24 25 26
DS4 L 8.5 0 43.4   -8.5 0 43.4   8 -4 35   0 -3.8 11.3   -1 -3 51   &
     -8.5 -2.36 14.35   5 0 -0.1   -10.6 -2.36 25.5   8.72 0 8.52  &
     0 -4.5 8   0 0 42.9   0 0 50.8   0 0 42.9   0 0 26.9          &
     0 0 11.9   0 0 -0.1   0 0 69.9   10.5 0 -80.1   -10.5 0 -80.1 &
     0 -8 -4.9
DS5 S 30 31 0 32 0 33 34 35 36 0 37 38 39 40 41 42 43 44 45 46
DS6 L 0 0 1   0 0 1   0 0 0   0 0 1   0 0 0   0 0 1   0 0 1 &
     1 0 0   0 0 1   0 0 0   0 0 1   0 0 1   0 0 1   0 0 1 &
     0 0 1   0 0 1   0 0 1   0 0 1   0 0 1   0 0 1
```

```
SI7  0 7.6
SP7  -21 1
SI8  0 7.6
SP8  -21 1
SI9  0 8.2
SP9  -21 2
SI10 0 11.4
SP10 -21 1
SI11 0 8.2
SP11 -21 2
SI12 0 2.6
SP12 -21 1
SI13 0 7.1
SP13 -21 1
SI14 0 3.85
SP14 -21 1
SI15 0 4
SP15 -21 1
SI16 0 5.2
SP16 -21 2
SI17 0 20.2
SP17 -21 1
SI18 0 20.3
SP18 -21 1
SI19 0 20.3
SP19 -21 1
SI20 0 20.3
SP20 -21 1
SI21 0 20.3
SP21 -21 1
SI22 0 20.3
SP22 -21 1
SI23 0 10.1
SP23 -21 1
SI24 0 11
SP24 -21 1
SI25 0 11
SP25 -21 1
SI26 0 8.1
SP26 -21 1
SI27 0 16.6
SP27 -21 1
SI30 0 24.6
SP30 -21 0
SI31 0 24.6
SP31 -21 0
SI32 0 10.2
SP32 -21 0
SI33 0 9.75
SP33 -21 0
SI34 0 8.92
SP34 -21 0
SI35 0 21.2
SP35 -21 0
SI36 0 16
SP36 -21 0
```

```
SI37 0 27.2
SP37 -21 0
SI38 0 16.6
SP38 -21 0
SI39 0 8.1
SP39 -21 0
SI40 0 16.2
SP40 -21 0
SI41 0 15.2
SP41 -21 0
SI42 0 12.2
SP42 -21 0
SI43 0 24.2
SP43 -21 0
SI44 0 80.2
SP44 -21 0
SI45 0 80.2
SP45 -21 0
SI46 0 5
SP46 -21 0
C
C
C Tally Cards
c Back Right Lung
F8:P 501
E8 0 1e-8 .000876 1020i 3.243776
FT8 SCX 2  GEB -0.00715076 0.0652825 -0.178934
c Front Right Lung
F18:P 511
E18 0 1e-8 .000876 1020i 3.243776
FT18 SCX 2 GEB -0.00715076 0.0652825 -0.178934
c Front Neck Under Chin
F28:P 521
E28 0 1e-8 .000876 1020i 3.243776
FT28 SCX 2 GEB -0.00715076 0.0652825 -0.178934
c Outer Left Leg
F38:P 531
E38 0 1e-8 .000876 1020i 3.243776
FT38 SCX 2 GEB -0.00715076 0.0652825 -0.178934
C
C Material Cards
C       THIS IS THE COMPOSITION FOR AIR
M1    7014 -.7558 8016 -.2314 18000 -.0128
C      THIS IS THE COMPOSITION FOR LUNG TISSUE
M2    1001 -.1021
      6012 -.1001
      7014 -.0280
      8016 -.7596
     11023 -.0019
     15031 -.0008
     16032 -.0023
     17000 -.0027
     19000 -.0020
     20000 -.0001
     26000 -.0004
C       THE COMPOSITION FOR TOTAL BODY MINUS SKELETON AND LUNGS
```

```
M3    1001 -.1047
      6012 -.2302
      7014 -.0234
      8016 -.6321
     11023 -.0013
     12000 -.0002
     15031 -.0024
     16032 -.0022
     17000 -.0014
     19000 -.0021
C     THE COMPOSITION FOR SKELETAL TISSUE
M4    1001 -.0704
      6012 -.2279
      8016 -.4856
      7014 -.0387
     11023 -.0032
     12000 -.0011
     15031 -.0694
     16032 -.0017
     17000 -.0014
     19000 -.0015
     20000 -.0991
c     Adult Tissues (Density = 1.04 g/cc)
M5       1001  -0.10454
         6012  -0.22663
         7014  -0.02490
         8016  -0.63525
        11023  -0.00112
        12000  -0.00013
        14000  -0.00030
        15031  -0.00134
        16032  -0.00204
        17000  -0.00133
        19000  -0.00208
        20000  -0.00024
        26000  -0.00005
        30000  -0.00003
        37085  -0.000007217
        37087  -0.000002783
        40000  -0.00001
c Detectors Materials
C Al Casing
m501 13027 1
C Low Density Glass
m502 14000 0.3333 8000 0.6667
C Foam
m503 1000 0.6667 6000 0.3333
C NaI Crystal 2X2
m504 11000.04p 0.5 53000.04p 0.5
C Al2O3
m509 13027 0.4 8016 0.6
c STOP NPS 1E8 F38 0.01
lost 50
NPS 4E9
RAND GEN=2 SEED=1561615651
PHYS:P 4J 1
```

```
PRINT
MODE P
```

APPENDIX C: COUNT RATE PER 250-mSv INTAKE FOR ANTHROPOMORPHIC PHANTOMS

Notes on the data:

- Back Right Lung - Posterior Upper Right Torso
- Front Right Lung - Anterior Upper Right Torso
- Neck - Anterior Neck
- Thigh - Lateral left Thigh

CONTENTS OF APPENDIX C

Reference Male – Am-241

Reference Male: Am-241 M				
Days	**Back Right Lung (cpm per 250-mSv Intake)**	**Front Right Lung (cpm per 250-mSv Intake)**	**Neck (cpm per 250-mSv Intake)**	**Thigh (cpm per 250-mSv Intake)**
0.0	7.79E+00	7.44E+00	6.59E-01	2.98E-03
0.2	5.68E+00	4.49E+00	6.32E-01	1.48E-01
0.5	5.15E+00	3.86E+00	5.34E-01	1.48E-01
1.0	4.56E+00	3.13E+00	4.23E-01	1.36E-01
2.0	4.02E+00	2.43E+00	3.14E-01	9.13E-02
3.0	3.84E+00	2.18E+00	2.73E-01	6.39E-02
4.0	3.79E+00	2.07E+00	2.56E-01	5.20E-02
5.0	3.78E+00	2.02E+00	2.50E-01	4.75E-02
6.0	3.79E+00	1.99E+00	2.47E-01	4.60E-02
7.0	3.81E+00	1.97E+00	2.45E-01	4.57E-02
8.0	3.82E+00	1.95E+00	2.44E-01	4.58E-02
9.0	3.84E+00	1.93E+00	2.43E-01	4.61E-02
10.0	3.86E+00	1.92E+00	2.42E-01	4.64E-02
20.0	4.04E+00	1.77E+00	2.33E-01	4.97E-02
30.0	4.23E+00	1.66E+00	2.25E-01	5.20E-02

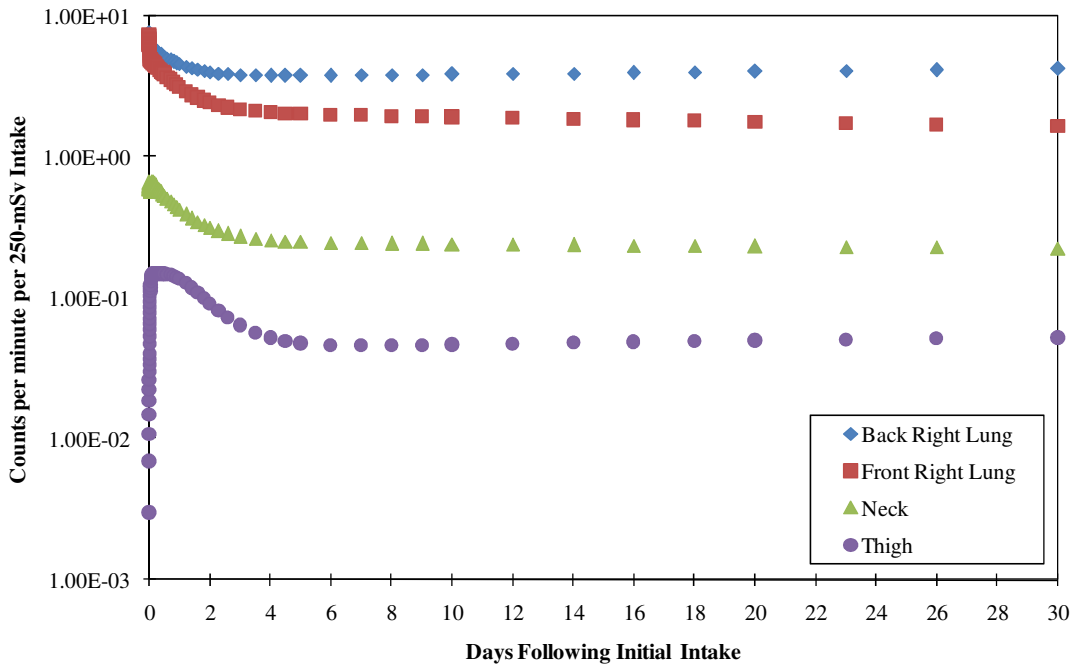

Reference Male – Co-60

Reference Male: ^{60}Co M				
Days	**Back Right Lung (cpm per 250-mSv Intake)**	**Front Right Lung (cpm per 250-mSv Intake)**	**Neck (cpm per 250-mSv Intake)**	**Thigh (cpm per 250-mSv Intake)**
0.0	2.26E+04	2.15E+04	3.76E+03	7.71E+01
0.2	2.58E+04	2.64E+04	5.80E+03	2.33E+03
0.5	2.71E+04	2.76E+04	7.50E+03	3.94E+03
1.0	2.76E+04	2.78E+04	9.09E+03	5.23E+03
2.0	2.76E+04	2.74E+04	1.00E+04	5.14E+03
3.0	2.70E+04	2.67E+04	9.97E+03	4.55E+03
4.0	2.63E+04	2.61E+04	9.69E+03	4.13E+03
5.0	2.57E+04	2.54E+04	9.37E+03	3.86E+03
6.0	2.51E+04	2.48E+04	9.08E+03	3.68E+03
7.0	2.46E+04	2.43E+04	8.82E+03	3.53E+03
8.0	2.41E+04	2.38E+04	8.58E+03	3.41E+03
9.0	2.37E+04	2.33E+04	8.36E+03	3.30E+03
10.0	2.32E+04	2.29E+04	8.16E+03	3.21E+03
20.0	2.02E+04	1.99E+04	6.98E+03	2.70E+03
30.0	1.83E+04	1.81E+04	6.48E+03	2.55E+03

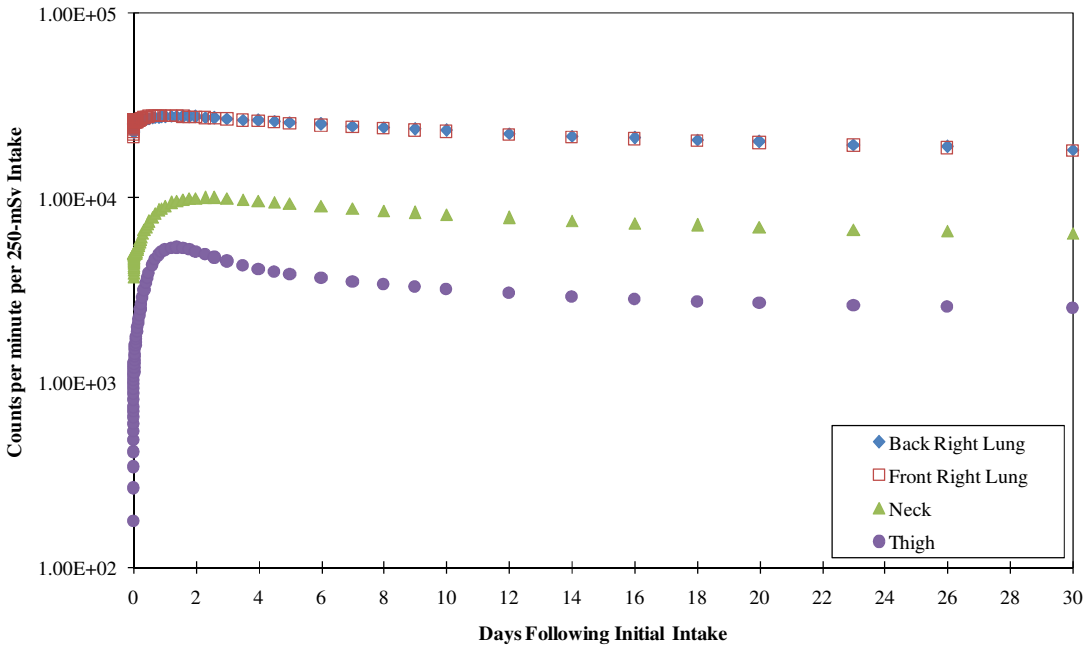

Reference Male – Cs-137

Reference Male: ^{137}Cs F				
Days	**Back Right Lung (cpm per 250-mSv Intake)**	**Front Right Lung (cpm per 250-mSv Intake)**	**Neck (cpm per 250-mSv Intake)**	**Thigh (cpm per 250-mSv Intake)**
0.0	3.58E+04	3.38E+04	5.05E+03	4.81E+01
0.2	1.37E+05	1.48E+05	9.42E+04	5.02E+04
0.5	2.14E+05	2.27E+05	1.56E+05	8.28E+04
1.0	2.55E+05	2.70E+05	1.89E+05	1.00E+05
2.0	2.62E+05	2.76E+05	1.94E+05	1.03E+05
3.0	2.57E+05	2.71E+05	1.90E+05	1.01E+05
4.0	2.52E+05	2.66E+05	1.87E+05	9.94E+04
5.0	2.48E+05	2.62E+05	1.84E+05	9.78E+04
6.0	2.45E+05	2.58E+05	1.82E+05	9.66E+04
7.0	2.42E+05	2.56E+05	1.80E+05	9.55E+04
8.0	2.40E+05	2.53E+05	1.78E+05	9.46E+04
9.0	2.38E+05	2.51E+05	1.76E+05	9.38E+04
10.0	2.36E+05	2.49E+05	1.75E+05	9.30E+04
20.0	2.21E+05	2.33E+05	1.64E+05	8.70E+04
30.0	2.08E+05	2.19E+05	1.54E+05	8.17E+04

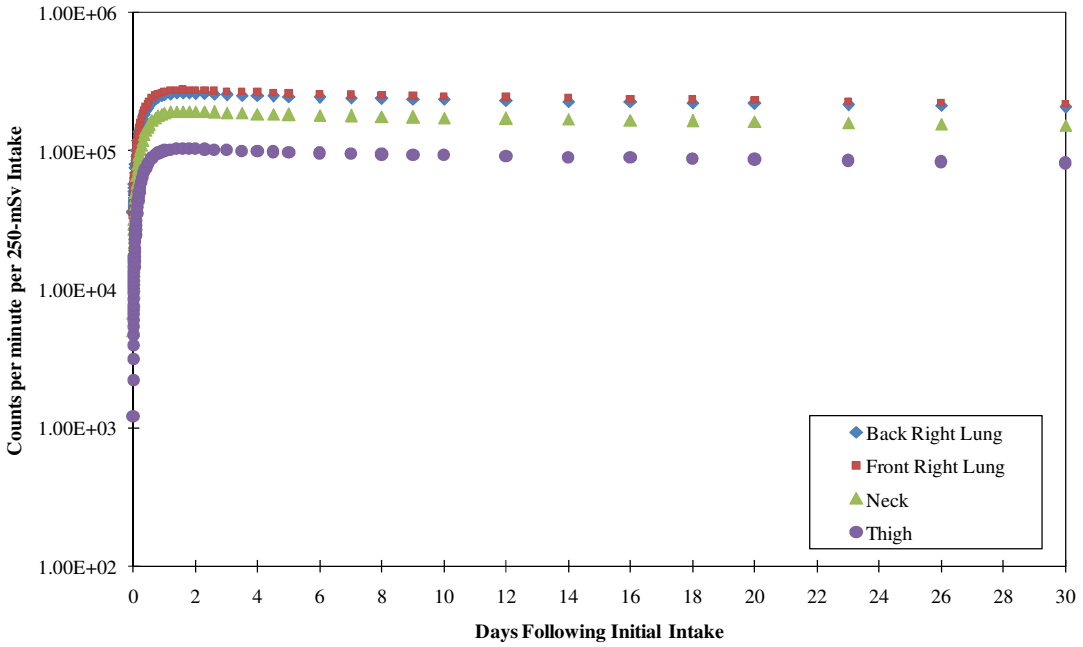

Reference Male – I-131

Reference Male: I-131 F				
Days	**Back Right Lung (cpm per 250-mSv Intake)**	**Front Right Lung (cpm per 250-mSv Intake)**	**Neck (cpm per 250-mSv Intake)**	**Thigh (cpm per 250-mSv Intake)**
0.0	3.58E+04	3.38E+04	4.56E+03	2.21E+01
0.2	2.24E+04	2.76E+04	5.43E+04	5.50E+03
0.5	1.04E+04	1.38E+04	6.91E+04	2.44E+03
1.0	3.85E+03	6.19E+03	7.50E+04	7.36E+02
2.0	2.24E+03	4.14E+03	7.12E+04	3.90E+02
3.0	2.43E+03	4.17E+03	6.52E+04	5.11E+02
4.0	2.64E+03	4.24E+03	5.97E+04	6.23E+02
5.0	2.78E+03	4.26E+03	5.46E+04	7.06E+02
6.0	2.85E+03	4.22E+03	4.99E+04	7.63E+02
7.0	2.88E+03	4.13E+03	4.56E+04	7.99E+02
8.0	2.86E+03	4.02E+03	4.17E+04	8.17E+02
9.0	2.81E+03	3.88E+03	3.81E+04	8.22E+02
10.0	2.74E+03	3.72E+03	3.48E+04	8.16E+02
20.0	1.62E+03	2.03E+03	1.40E+04	5.22E+02
30.0	7.65E+02	9.35E+02	5.62E+03	2.53E+02

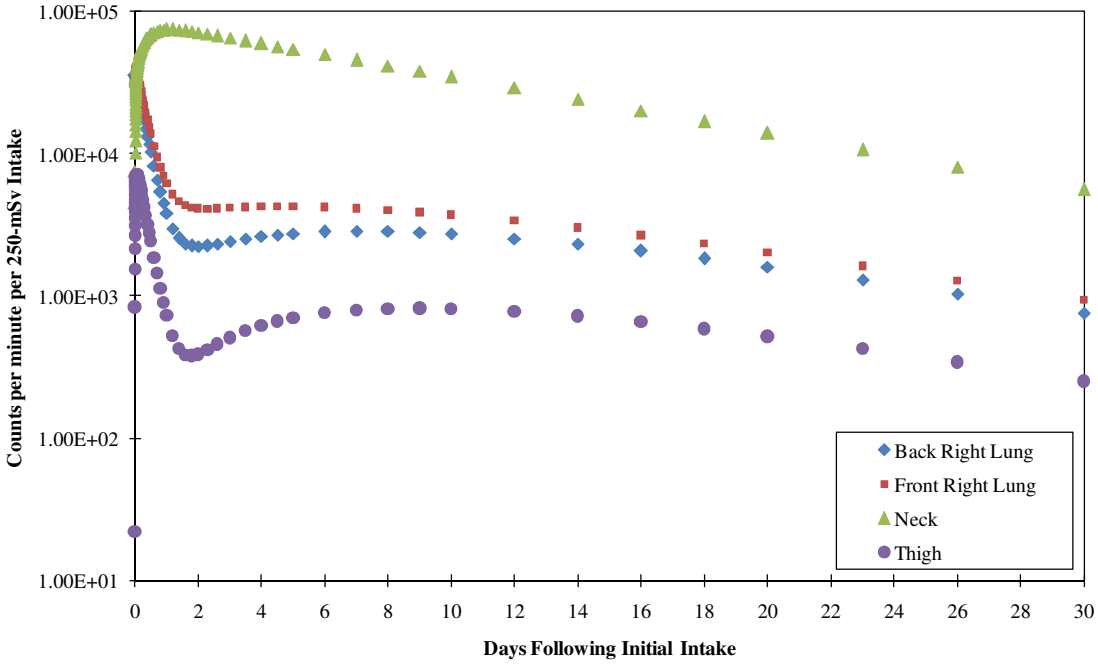

Reference Male – Ir-192

Reference Male: Ir-192 M				
Days	**Back Right Lung (cpm per 250-mSv Intake)**	**Front Right Lung (cpm per 250-mSv Intake)**	**Neck (cpm per 250-mSv Intake)**	**Thigh (cpm per 250-mSv Intake)**
0.0	1.14E+05	1.08E+05	1.67E+04	9.01E+01
0.2	1.30E+05	1.30E+05	2.79E+04	1.04E+04
0.5	1.35E+05	1.36E+05	3.54E+04	1.76E+04
1.0	1.34E+05	1.33E+05	3.95E+04	2.19E+04
2.0	1.29E+05	1.27E+05	4.02E+04	1.96E+04
3.0	1.26E+05	1.24E+05	3.98E+04	1.68E+04
4.0	1.24E+05	1.21E+05	3.93E+04	1.55E+04
5.0	1.21E+05	1.19E+05	3.89E+04	1.49E+04
6.0	1.19E+05	1.17E+05	3.85E+04	1.46E+04
7.0	1.17E+05	1.15E+05	3.82E+04	1.45E+04
8.0	1.15E+05	1.13E+05	3.78E+04	1.44E+04
9.0	1.14E+05	1.12E+05	3.75E+04	1.44E+04
10.0	1.12E+05	1.10E+05	3.72E+04	1.43E+04
20.0	9.65E+04	9.55E+04	3.44E+04	1.39E+04
30.0	8.44E+04	8.39E+04	3.20E+04	1.35E+04

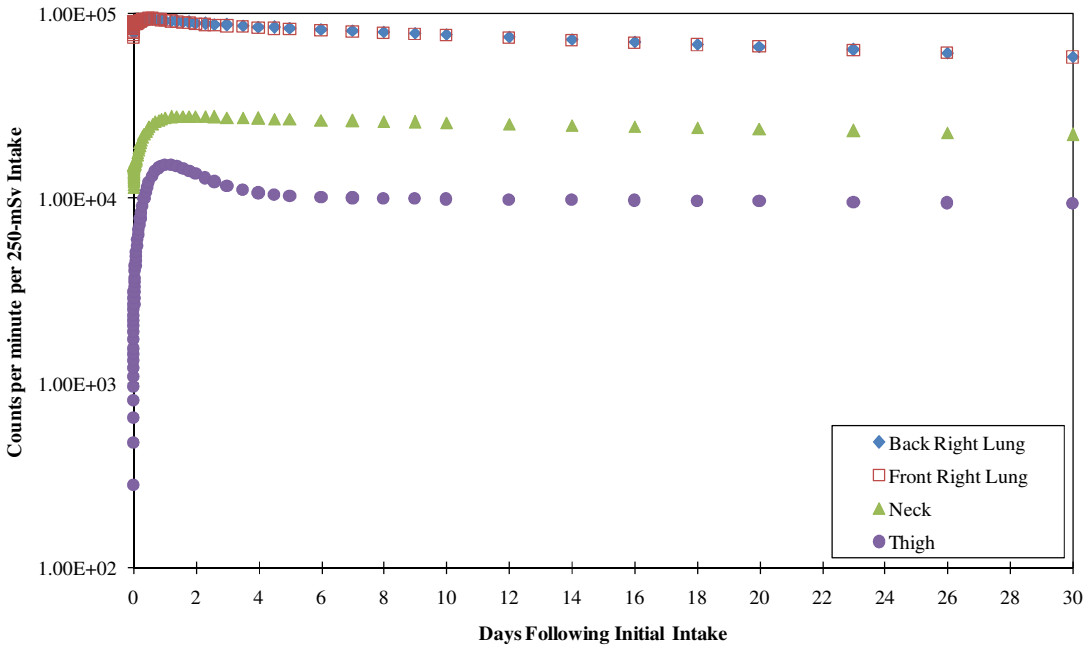

Reference Female – Am-241

Reference Female: Am-241 M			
Days	**Back Right Lung (cpm per 250-mSv Intake)**	**Neck (cpm per 250-mSv Intake**	**Thigh (cpm per 250-mSv Intake)**
0.0	7.42E+00	8.13E-01	4.39E-03
0.2	5.82E+00	8.14E-01	1.56E-01
0.5	5.36E+00	6.87E-01	1.59E-01
1.0	4.87E+00	5.43E-01	1.48E-01
2.0	4.42E+00	4.02E-01	9.97E-02
3.0	4.29E+00	3.49E-01	6.89E-02
4.0	4.26E+00	3.29E-01	5.54E-02
5.0	4.27E+00	3.20E-01	5.02E-02
6.0	4.30E+00	3.16E-01	4.85E-02
7.0	4.32E+00	3.14E-01	4.81E-02
8.0	4.36E+00	3.13E-01	4.82E-02
9.0	4.39E+00	3.11E-01	4.85E-02
10.0	4.42E+00	3.10E-01	4.89E-02
20.0	4.73E+00	3.01E-01	5.22E-02
30.0	5.03E+00	2.92E-01	5.46E-02

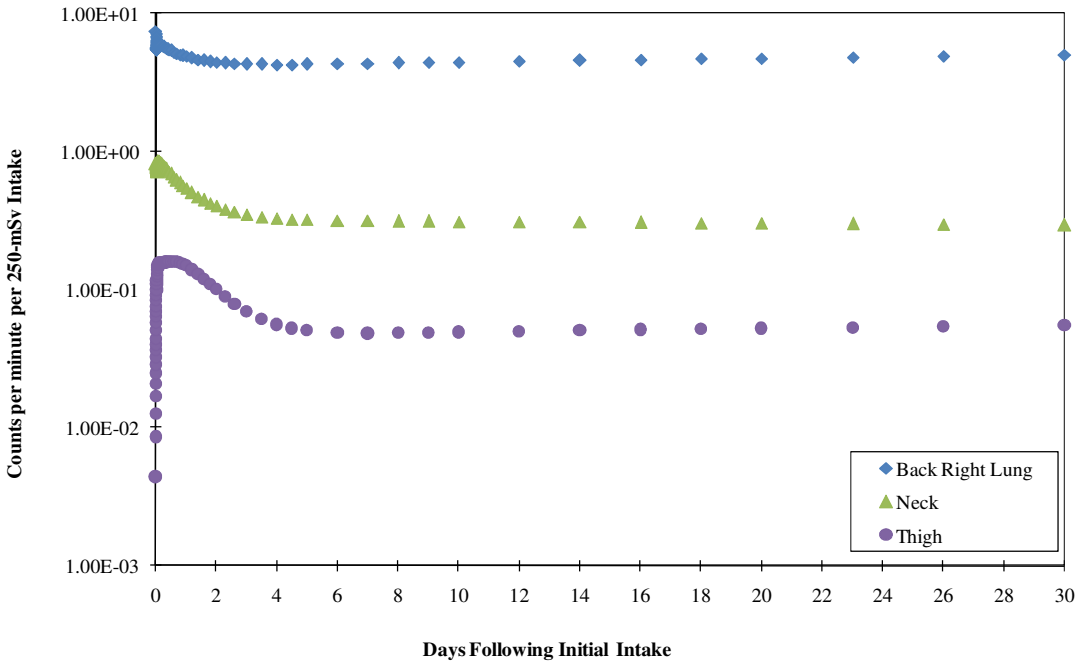

Reference Female – Co-60

Reference Female: ^{60}Co M			
Days	**Back Right Lung (cpm per 250-mSv Intake)**	**Neck (cpm per 250-mSv Intake**	**Thigh (cpm per 250-mSv Intake)**
0.0	2.25E+04	4.04E+03	8.85E+01
0.2	2.48E+04	6.67E+03	2.37E+03
0.5	2.63E+04	8.83E+03	4.03E+03
1.0	2.75E+04	1.09E+04	5.28E+03
2.0	2.79E+04	1.21E+04	5.07E+03
3.0	2.74E+04	1.20E+04	4.42E+03
4.0	2.68E+04	1.17E+04	3.98E+03
5.0	2.62E+04	1.13E+04	3.71E+03
6.0	2.56E+04	1.09E+04	3.52E+03
7.0	2.50E+04	1.06E+04	3.38E+03
8.0	2.45E+04	1.03E+04	3.26E+03
9.0	2.41E+04	1.00E+04	3.16E+03
10.0	2.36E+04	9.81E+03	3.07E+03
20.0	2.05E+04	8.38E+03	2.58E+03
30.0	1.87E+04	7.79E+03	2.44E+03

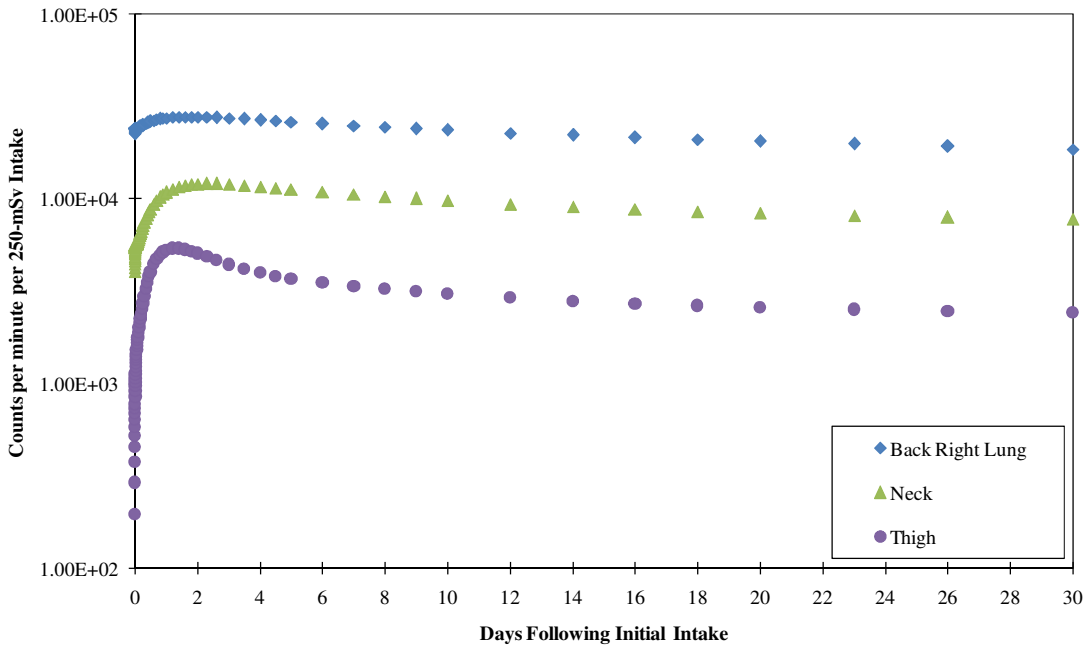

Reference Female – Cs-137

Reference Female: ^{137}Cs F			
Days	**Back Right Lung (cpm per 250-mSv Intake)**	**Neck (cpm per 250-mSv Intake**	**Thigh (cpm per 250-mSv Intake)**
0.0	3.52E+04	5.49E+03	6.38E+01
0.2	1.43E+05	1.20E+05	4.89E+04
0.5	2.24E+05	1.99E+05	8.04E+04
1.0	2.68E+05	2.41E+05	9.74E+04
2.0	2.75E+05	2.48E+05	1.00E+05
3.0	2.69E+05	2.43E+05	9.82E+04
4.0	2.64E+05	2.38E+05	9.64E+04
5.0	2.60E+05	2.35E+05	9.49E+04
6.0	2.57E+05	2.32E+05	9.37E+04
7.0	2.54E+05	2.29E+05	9.27E+04
8.0	2.52E+05	2.27E+05	9.18E+04
9.0	2.50E+05	2.25E+05	9.10E+04
10.0	2.48E+05	2.24E+05	9.03E+04
20.0	2.32E+05	2.09E+05	8.44E+04
30.0	2.18E+05	1.97E+05	7.92E+04

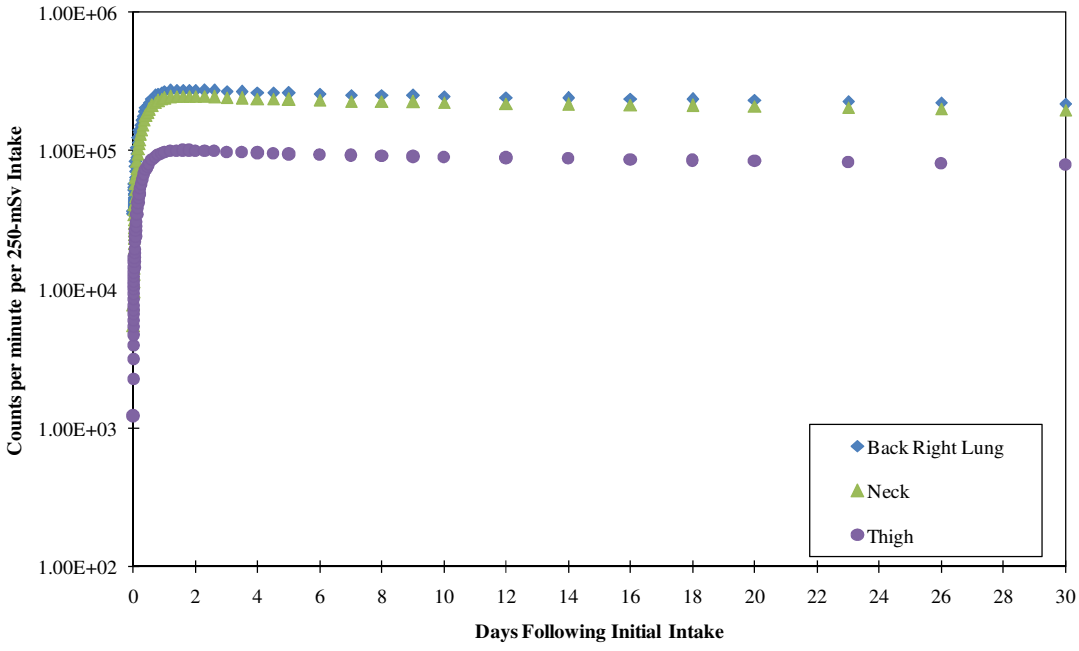

Reference Female – I-131

Reference Female: I-131 F			
Days	**Back Right Lung (cpm per 250-mSv Intake)**	**Neck (cpm per 250-mSv Intake**	**Thigh (cpm per 250-mSv Intake)**
0.0	3.51E+04	5.05E+03	2.27E+00
0.2	2.27E+04	5.47E+04	1.80E+02
0.5	1.12E+04	6.68E+04	8.11E+01
1.0	4.80E+03	7.14E+04	2.35E+01
2.0	3.19E+03	6.76E+04	1.00E+01
3.0	3.32E+03	6.21E+04	1.25E+01
4.0	3.46E+03	5.69E+04	1.51E+01
5.0	3.54E+03	5.21E+04	1.71E+01
6.0	3.56E+03	4.77E+04	1.85E+01
7.0	3.53E+03	4.37E+04	1.93E+01
8.0	3.46E+03	4.00E+04	1.97E+01
9.0	3.37E+03	3.66E+04	1.98E+01
10.0	3.25E+03	3.35E+04	1.97E+01
20.0	1.84E+03	1.37E+04	1.26E+01
30.0	8.56E+02	5.50E+03	6.08E+00

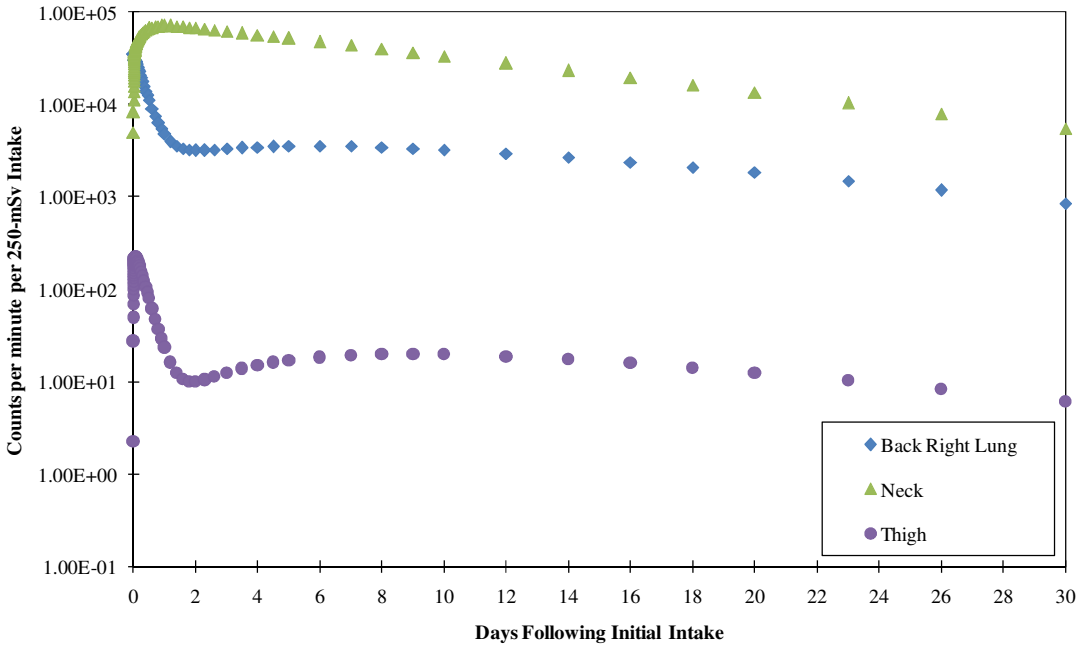

Reference Female – Ir-192

Reference Female: Ir-192 M			
Days	**Back Right Lung (cpm per 250-mSv Intake)**	**Neck (cpm per 250-mSv Intake**	**Thigh (cpm per 250-mSv Intake)**
0.0	1.13E+05	1.85E+04	1.26E+02
0.2	1.25E+05	3.36E+04	1.04E+04
0.5	1.31E+05	4.35E+04	1.80E+04
1.0	1.32E+05	4.90E+04	2.24E+04
2.0	1.29E+05	5.01E+04	1.97E+04
3.0	1.27E+05	4.96E+04	1.66E+04
4.0	1.24E+05	4.91E+04	1.51E+04
5.0	1.22E+05	4.86E+04	1.45E+04
6.0	1.20E+05	4.81E+04	1.42E+04
7.0	1.18E+05	4.77E+04	1.41E+04
8.0	1.16E+05	4.73E+04	1.40E+04
9.0	1.14E+05	4.69E+04	1.39E+04
10.0	1.13E+05	4.66E+04	1.39E+04
20.0	9.74E+04	4.34E+04	1.35E+04
30.0	8.53E+04	4.06E+04	1.31E+04

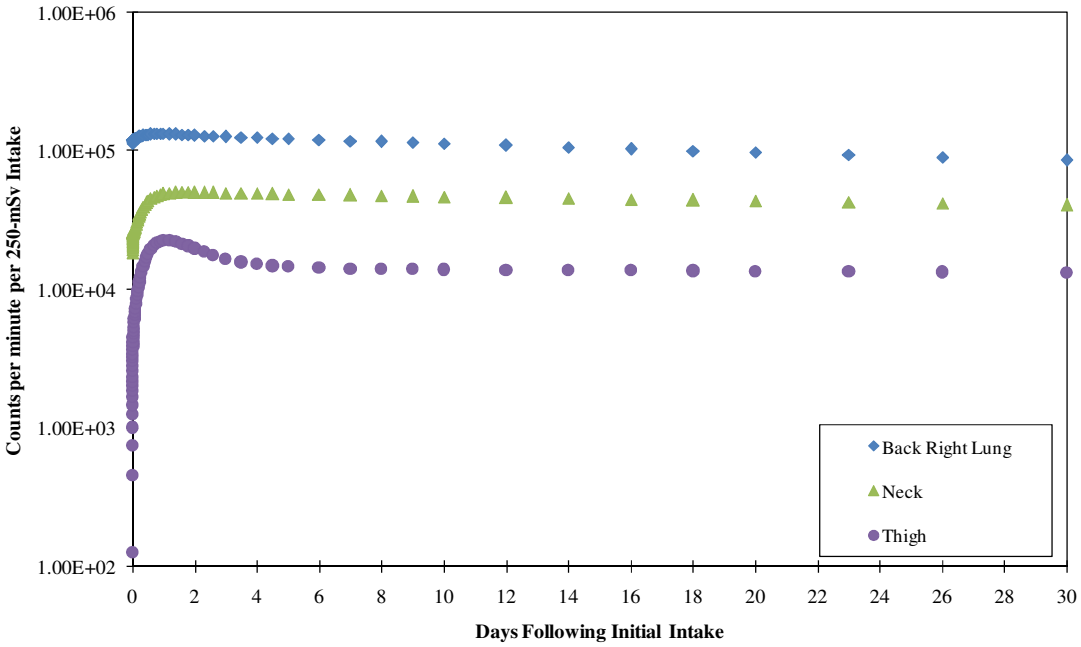

Adipose Male – Am-241

Adipose Male: Am-241 M			
Days	**Back Right Lung (cpm per 250-mSv Intake)**	**Neck (cpm per 250-mSv Intake**	**Thigh (cpm per 250-mSv Intake)**
0.0	4.09E+00	6.12E-01	1.57E-03
0.2	3.19E+00	6.52E-01	1.44E-01
0.5	2.92E+00	5.50E-01	1.46E-01
1.0	2.62E+00	4.34E-01	1.35E-01
2.0	2.36E+00	3.20E-01	9.07E-02
3.0	2.27E+00	2.77E-01	6.27E-02
4.0	2.25E+00	2.60E-01	5.05E-02
5.0	2.25E+00	2.54E-01	4.59E-02
6.0	2.26E+00	2.51E-01	4.43E-02
7.0	2.28E+00	2.49E-01	4.40E-02
8.0	2.29E+00	2.48E-01	4.41E-02
9.0	2.31E+00	2.47E-01	4.44E-02
10.0	2.32E+00	2.46E-01	4.47E-02
20.0	2.47E+00	2.40E-01	4.79E-02
30.0	2.61E+00	2.34E-01	5.02E-02

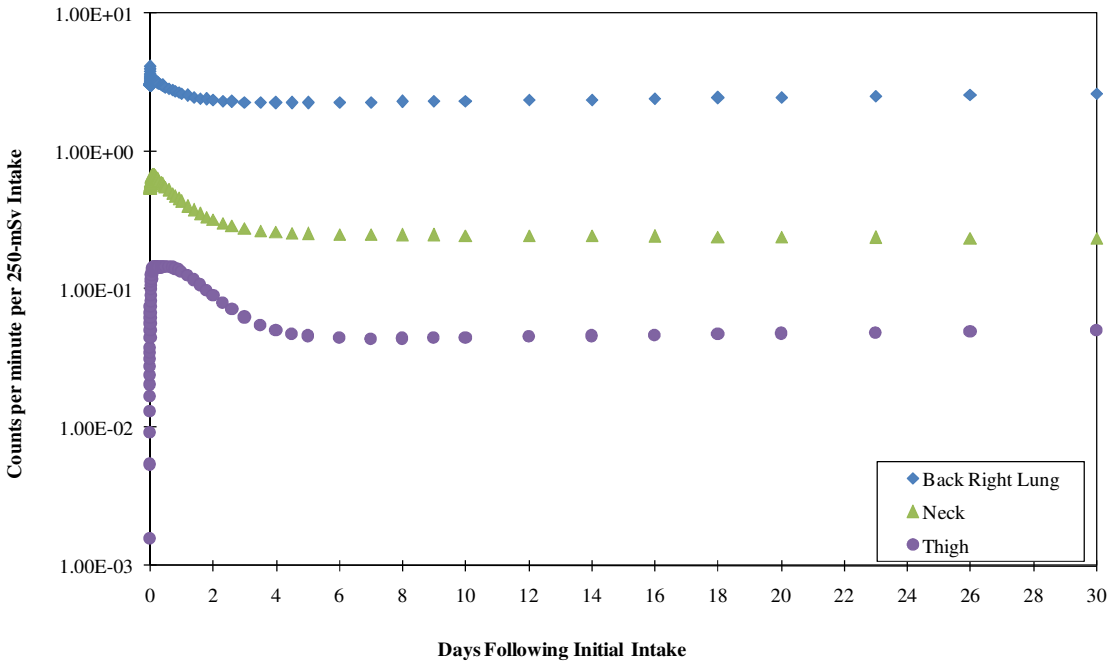

Adipose Male – Co-60

Adipose Male: ^{60}Co M			
Days	**Back Right Lung (cpm per 250-mSv Intake)**	**Neck (cpm per 250-mSv Intake**	**Thigh (cpm per 250-mSv Intake)**
0.0	1.28E+04	3.18E+03	6.62E+01
0.2	1.46E+04	5.26E+03	2.09E+03
0.5	1.57E+04	7.11E+03	3.52E+03
1.0	1.66E+04	8.87E+03	4.67E+03
2.0	1.69E+04	9.95E+03	4.61E+03
3.0	1.66E+04	9.91E+03	4.09E+03
4.0	1.62E+04	9.63E+03	3.73E+03
5.0	1.58E+04	9.31E+03	3.49E+03
6.0	1.55E+04	9.01E+03	3.32E+03
7.0	1.51E+04	8.74E+03	3.19E+03
8.0	1.48E+04	8.49E+03	3.07E+03
9.0	1.45E+04	8.27E+03	2.98E+03
10.0	1.42E+04	8.08E+03	2.89E+03
20.0	1.23E+04	6.89E+03	2.44E+03
30.0	1.12E+04	6.41E+03	2.31E+03

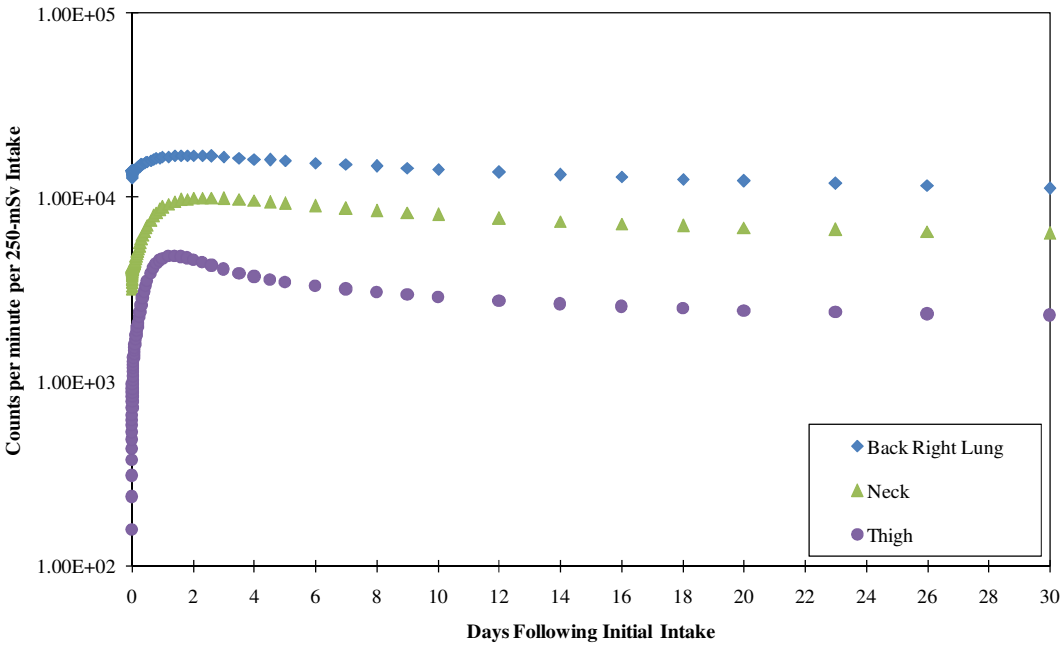

Adipose Male – Cs-137

Adipose Male: ^{137}Cs F			
Days	**Back Right Lung (cpm per 250-mSv Intake)**	**Neck (cpm per 250-mSv Intake**	**Thigh (cpm per 250-mSv Intake)**
0.0	2.37E+04	4.47E+03	4.68E+01
0.2	1.12E+05	1.02E+05	9.49E+04
0.5	1.78E+05	1.70E+05	1.58E+05
1.0	2.13E+05	2.06E+05	1.92E+05
2.0	2.19E+05	2.12E+05	1.98E+05
3.0	2.15E+05	2.08E+05	1.94E+05
4.0	2.11E+05	2.04E+05	1.90E+05
5.0	2.07E+05	2.01E+05	1.87E+05
6.0	2.05E+05	1.98E+05	1.85E+05
7.0	2.03E+05	1.96E+05	1.83E+05
8.0	2.01E+05	1.94E+05	1.81E+05
9.0	1.99E+05	1.92E+05	1.80E+05
10.0	1.97E+05	1.91E+05	1.78E+05
20.0	1.85E+05	1.79E+05	1.67E+05
30.0	1.74E+05	1.68E+05	1.57E+05

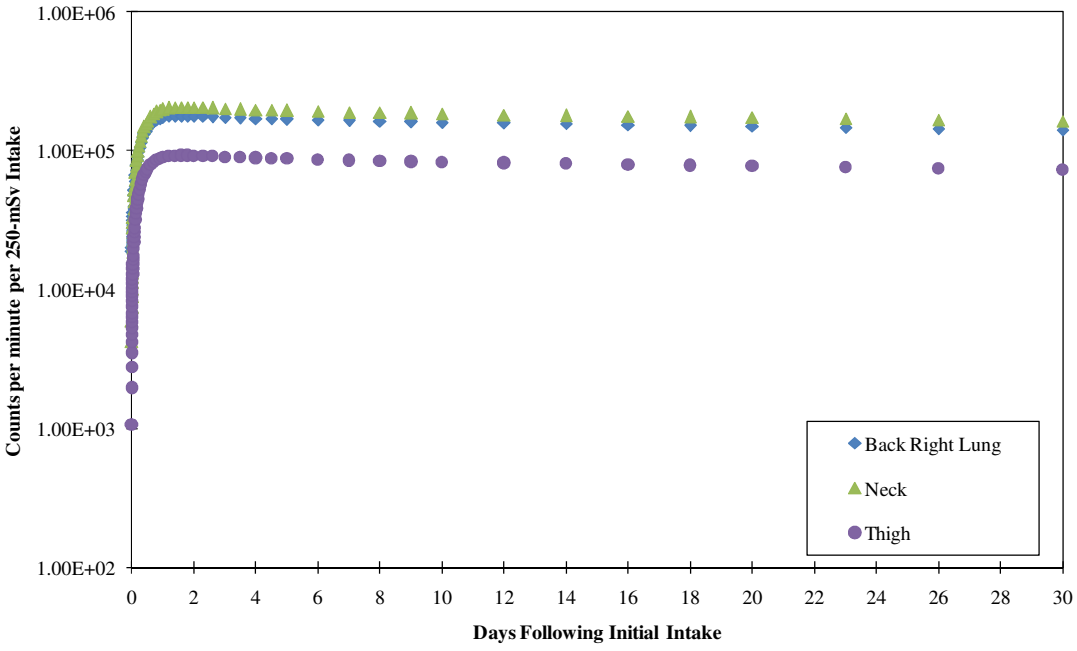

Adipose Male – I-131

Adipose Male: I-131 F			
Days	**Back Right Lung (cpm per 250-mSv Intake)**	**Neck (cpm per 250-mSv Intake**	**Thigh (cpm per 250-mSv Intake)**
0.0	1.86E+04	3.84E+03	2.22E+01
0.2	1.35E+04	4.90E+04	4.92E+03
0.5	6.51E+03	6.11E+04	2.18E+03
1.0	2.69E+03	6.58E+04	6.58E+02
2.0	1.75E+03	6.24E+04	3.49E+02
3.0	1.87E+03	5.73E+04	4.56E+02
4.0	1.98E+03	5.25E+04	5.57E+02
5.0	2.05E+03	4.80E+04	6.31E+02
6.0	2.08E+03	4.40E+04	6.82E+02
7.0	2.08E+03	4.02E+04	7.14E+02
8.0	2.05E+03	3.68E+04	7.30E+02
9.0	2.01E+03	3.37E+04	7.34E+02
10.0	1.95E+03	3.08E+04	7.29E+02
20.0	1.12E+03	1.25E+04	4.66E+02
30.0	5.27E+02	5.02E+03	2.26E+02

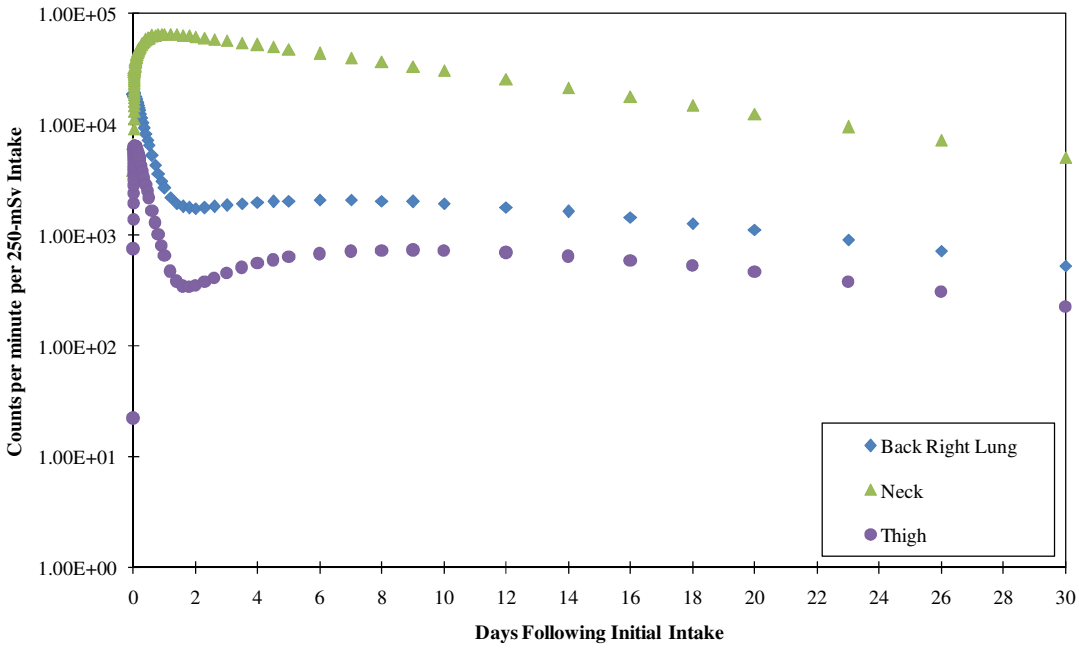

Adipose Male – Ir-192

Adipose Male: Ir-192 M			
Days	**Back Right Lung (cpm per 250-mSv Intake)**	**Neck (cpm per 250-mSv Intake**	**Thigh (cpm per 250-mSv Intake)**
0.0	6.46E+04	1.47E+04	9.18E+01
0.2	7.32E+04	2.69E+04	9.62E+03
0.5	7.80E+04	3.53E+04	1.61E+04
1.0	7.93E+04	4.00E+04	2.00E+04
2.0	7.76E+04	4.10E+04	1.79E+04
3.0	7.59E+04	4.06E+04	1.54E+04
4.0	7.46E+04	4.02E+04	1.42E+04
5.0	7.33E+04	3.98E+04	1.36E+04
6.0	7.22E+04	3.95E+04	1.34E+04
7.0	7.10E+04	3.91E+04	1.33E+04
8.0	7.00E+04	3.88E+04	1.32E+04
9.0	6.89E+04	3.85E+04	1.31E+04
10.0	6.79E+04	3.82E+04	1.31E+04
20.0	5.91E+04	3.56E+04	1.27E+04
30.0	5.21E+04	3.34E+04	1.23E+04

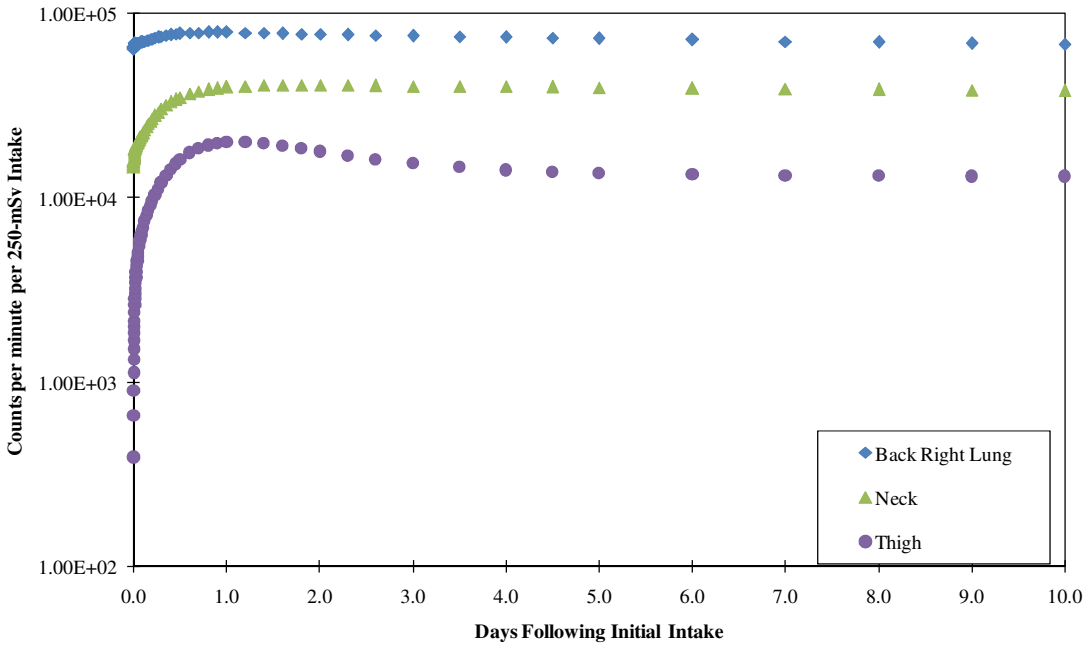

Adipose Female – Am-241

Adipose Female: Am-241 M			
Days	**Back Right Lung (cpm per 250-mSv Intake)**	**Neck (cpm per 250-mSv Intake**	**Thigh (cpm per 250-mSv Intake)**
0.0	5.63E+00	7.52E-01	3.62E-03
0.2	4.37E+00	7.62E-01	3.54E-01
0.5	4.00E+00	6.43E-01	3.17E-01
1.0	3.60E+00	5.08E-01	2.63E-01
2.0	3.23E+00	3.75E-01	1.80E-01
3.0	3.12E+00	3.26E-01	1.39E-01
4.0	3.09E+00	3.06E-01	1.23E-01
5.0	3.09E+00	2.98E-01	1.17E-01
6.0	3.11E+00	2.95E-01	1.15E-01
7.0	3.13E+00	2.93E-01	1.15E-01
8.0	3.15E+00	2.91E-01	1.16E-01
9.0	3.17E+00	2.90E-01	1.17E-01
10.0	3.19E+00	2.89E-01	1.18E-01
20.0	3.39E+00	2.80E-01	1.27E-01
30.0	3.59E+00	2.73E-01	1.33E-01

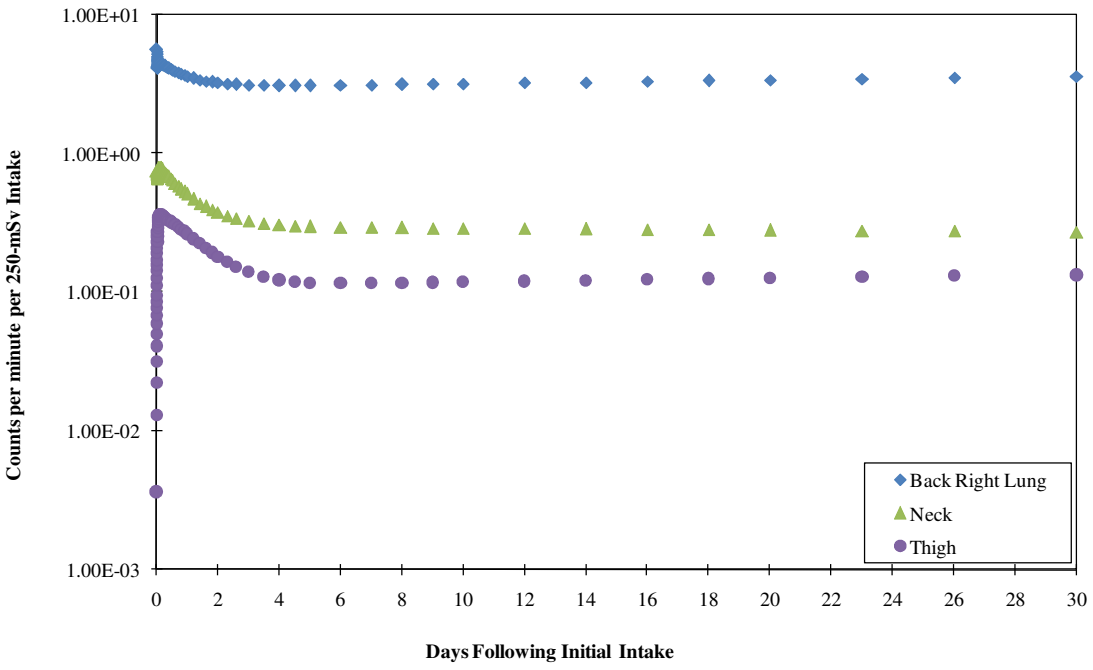

Adipose Female – Co-60

Adipose Female: ^{60}Co M			
Days	**Back Right Lung (cpm per 250-mSv Intake)**	**Neck (cpm per 250-mSv Intake**	**Thigh (cpm per 250-mSv Intake)**
0.0	1.56E+04	3.34E+03	6.93E+01
0.2	1.78E+04	5.57E+03	3.06E+03
0.5	1.91E+04	7.46E+03	5.43E+03
1.0	2.02E+04	9.25E+03	7.50E+03
2.0	2.06E+04	1.03E+04	8.13E+03
3.0	2.03E+04	1.03E+04	7.70E+03
4.0	1.98E+04	1.00E+04	7.25E+03
5.0	1.93E+04	9.67E+03	6.88E+03
6.0	1.89E+04	9.36E+03	6.59E+03
7.0	1.85E+04	9.08E+03	6.34E+03
8.0	1.81E+04	8.82E+03	6.13E+03
9.0	1.77E+04	8.59E+03	5.94E+03
10.0	1.74E+04	8.39E+03	5.77E+03
20.0	1.51E+04	7.16E+03	4.87E+03
30.0	1.37E+04	6.66E+03	4.61E+03

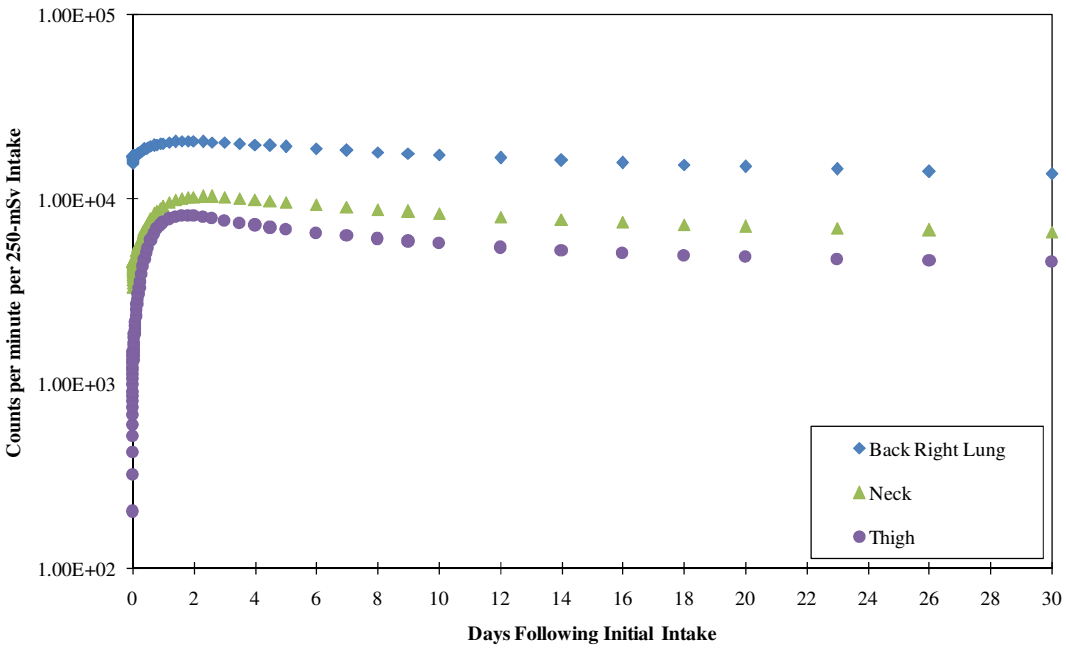

Adipose Female – Cs-137

Adipose Female: ^{137}Cs F			
Days	**Back Right Lung (cpm per 250-mSv Intake)**	**Neck (cpm per 250-mSv Intake**	**Thigh (cpm per 250-mSv Intake)**
0.0	2.37E+04	4.47E+03	4.68E+01
0.2	1.12E+05	1.02E+05	9.49E+04
0.5	1.78E+05	1.70E+05	1.58E+05
1.0	2.13E+05	2.06E+05	1.92E+05
2.0	2.19E+05	2.12E+05	1.98E+05
3.0	2.15E+05	2.08E+05	1.94E+05
4.0	2.11E+05	2.04E+05	1.90E+05
5.0	2.07E+05	2.01E+05	1.87E+05
6.0	2.05E+05	1.98E+05	1.85E+05
7.0	2.03E+05	1.96E+05	1.83E+05
8.0	2.01E+05	1.94E+05	1.81E+05
9.0	1.99E+05	1.92E+05	1.80E+05
10.0	1.97E+05	1.91E+05	1.78E+05
20.0	1.85E+05	1.79E+05	1.67E+05
30.0	1.74E+05	1.68E+05	1.57E+05

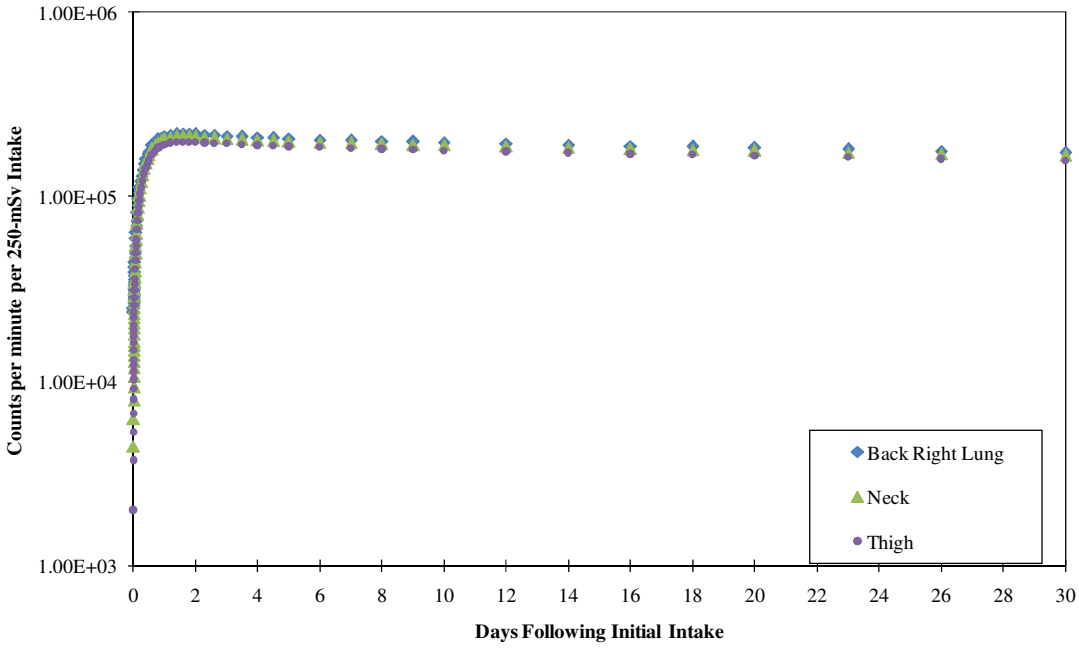

Adipose Female – I-131

Adipose Female: I-131 F			
Days	**Back Right Lung (cpm per 250-mSv Intake)**	**Neck (cpm per 250-mSv Intake**	**Thigh (cpm per 250-mSv Intake)**
0.0	2.35E+04	4.13E+03	2.46E+01
0.2	1.54E+04	4.58E+04	3.56E+03
0.5	7.60E+03	5.64E+04	1.59E+03
1.0	3.29E+03	6.04E+04	4.75E+02
2.0	2.20E+03	5.72E+04	2.41E+02
3.0	2.28E+03	5.25E+04	3.13E+02
4.0	2.37E+03	4.81E+04	3.82E+02
5.0	2.42E+03	4.41E+04	4.32E+02
6.0	2.43E+03	4.04E+04	4.67E+02
7.0	2.40E+03	3.70E+04	4.88E+02
8.0	2.35E+03	3.38E+04	5.00E+02
9.0	2.29E+03	3.09E+04	5.02E+02
10.0	2.21E+03	2.83E+04	4.99E+02
20.0	1.24E+03	1.15E+04	3.19E+02
30.0	5.78E+02	4.64E+03	1.54E+02

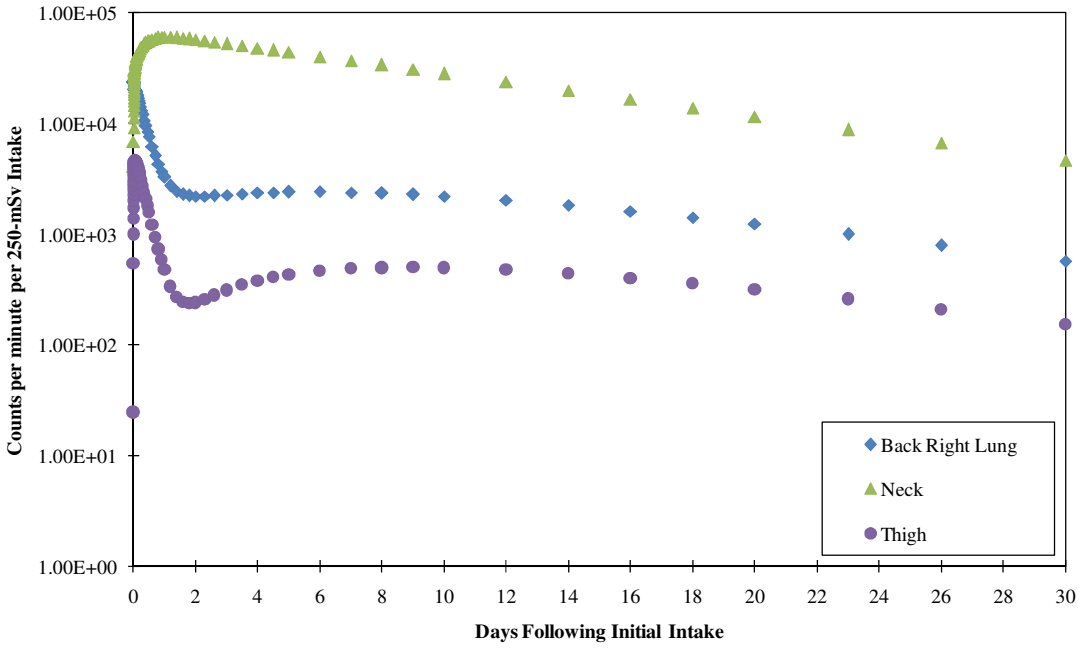

Adipose Female – Ir-192

Adipose Female: Ir-192 M			
Days	**Back Right Lung (cpm per 250-mSv Intake)**	**Neck (cpm per 250-mSv Intake**	**Thigh (cpm per 250-mSv Intake)**
0.0	7.99E+04	1.56E+04	1.07E+02
0.2	9.09E+04	2.89E+04	1.58E+04
0.5	9.66E+04	3.76E+04	2.67E+04
1.0	9.82E+04	4.25E+04	3.31E+04
2.0	9.61E+04	4.35E+04	3.22E+04
3.0	9.41E+04	4.30E+04	3.00E+04
4.0	9.24E+04	4.26E+04	2.88E+04
5.0	9.09E+04	4.22E+04	2.83E+04
6.0	8.94E+04	4.18E+04	2.80E+04
7.0	8.80E+04	4.15E+04	2.79E+04
8.0	8.67E+04	4.11E+04	2.78E+04
9.0	8.54E+04	4.08E+04	2.77E+04
10.0	8.41E+04	4.05E+04	2.76E+04
20.0	7.33E+04	3.77E+04	2.69E+04
30.0	6.46E+04	3.54E+04	2.61E+04

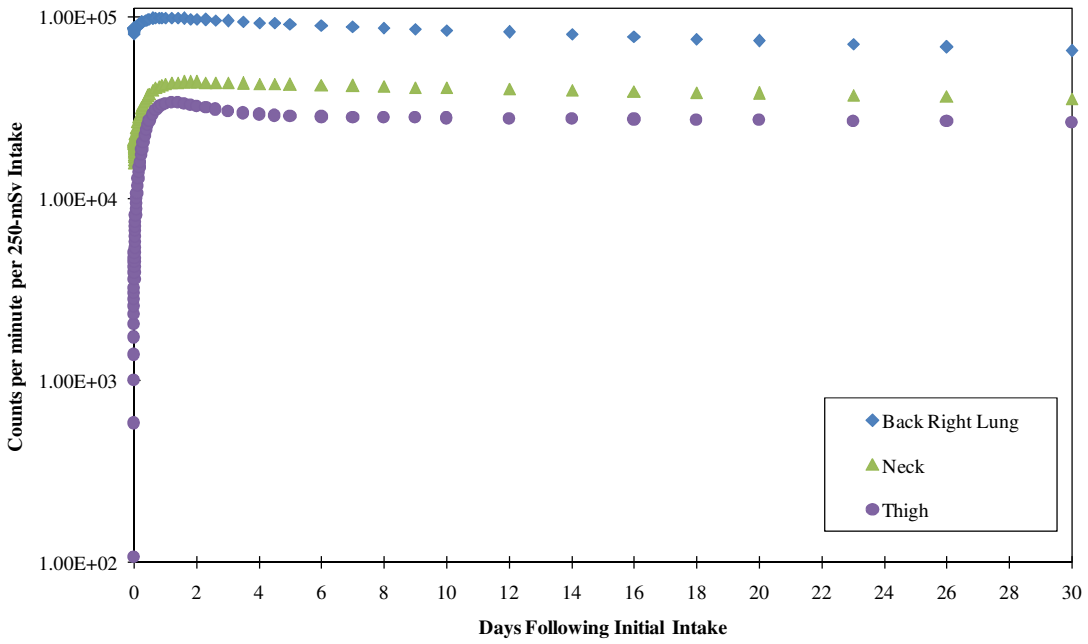

Post Menopausal Adipose Female – Am-241

Post Menopausal Adipose Female: Am-241 M			
Days	**Back Right Lung (cpm per 250-mSv Intake)**	**Neck (cpm per 250-mSv Intake**	**Thigh (cpm per 250-mSv Intake)**
0.0	4.69E+00	7.59E-01	2.84E-03
0.2	3.65E+00	7.70E-01	1.22E-01
0.5	3.34E+00	6.50E-01	1.23E-01
1.0	3.00E+00	5.13E-01	1.14E-01
2.0	2.69E+00	3.80E-01	7.66E-02
3.0	2.60E+00	3.29E-01	5.31E-02
4.0	2.57E+00	3.10E-01	4.29E-02
5.0	2.58E+00	3.02E-01	3.89E-02
6.0	2.59E+00	2.98E-01	3.76E-02
7.0	2.60E+00	2.96E-01	3.74E-02
8.0	2.62E+00	2.95E-01	3.75E-02
9.0	2.64E+00	2.94E-01	3.77E-02
10.0	2.66E+00	2.93E-01	3.80E-02
20.0	2.82E+00	2.84E-01	4.06E-02
30.0	2.99E+00	2.76E-01	4.25E-02

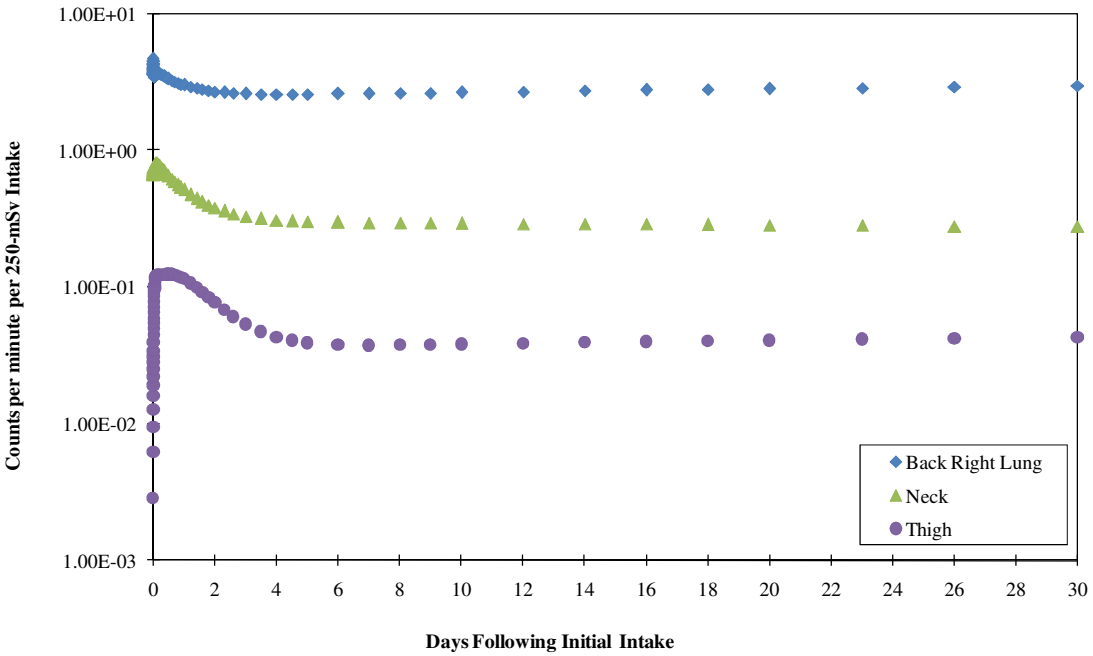

Post Menopausal Adipose Female – Co-60

Post Menopausal Adipose Female: ^{60}Co M			
Days	**Back Right Lung (cpm per 250-mSv Intake)**	**Neck (cpm per 250-mSv Intake**	**Thigh (cpm per 250-mSv Intake)**
0.0	1.48E+04	3.75E+03	7.56E+01
0.2	1.69E+04	6.11E+03	1.84E+03
0.5	1.81E+04	8.17E+03	3.08E+03
1.0	1.91E+04	1.01E+04	4.02E+03
2.0	1.94E+04	1.13E+04	3.87E+03
3.0	1.91E+04	1.13E+04	3.38E+03
4.0	1.87E+04	1.09E+04	3.06E+03
5.0	1.82E+04	1.06E+04	2.85E+03
6.0	1.78E+04	1.02E+04	2.71E+03
7.0	1.74E+04	9.94E+03	2.60E+03
8.0	1.70E+04	9.66E+03	2.51E+03
9.0	1.67E+04	9.42E+03	2.43E+03
10.0	1.64E+04	9.19E+03	2.36E+03
20.0	1.42E+04	7.85E+03	1.99E+03
30.0	1.29E+04	7.30E+03	1.88E+03

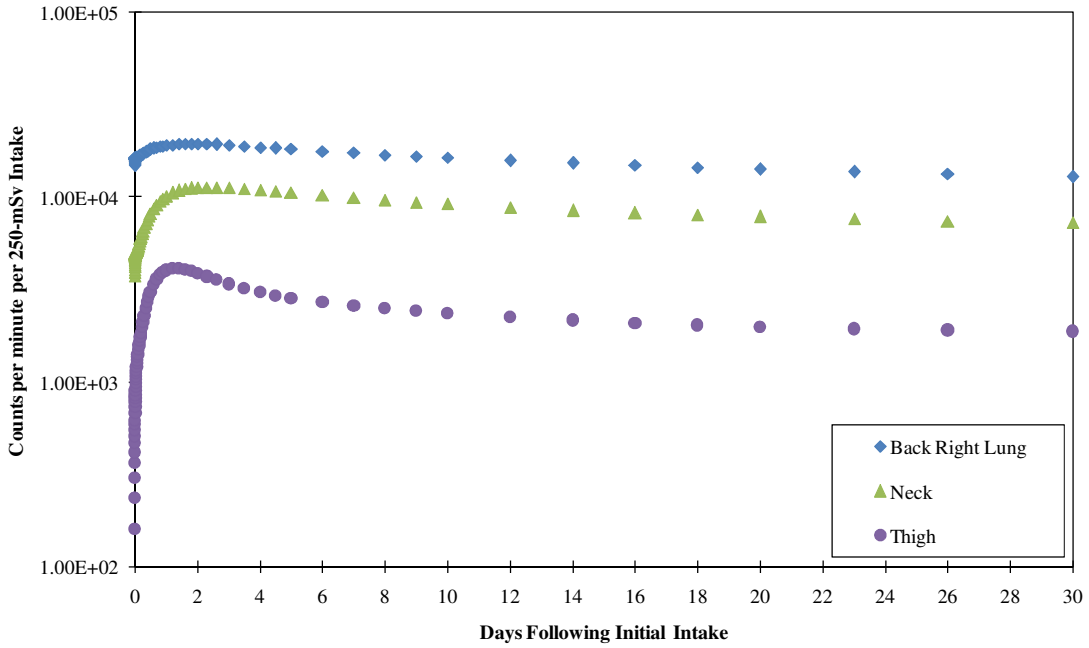

Post Menopausal Adipose Female – Cs-137

Post Menopausal Adipose Female: ^{137}Cs F			
Days	**Back Right Lung (cpm per 250-mSv Intake)**	**Neck (cpm per 250-mSv Intake**	**Thigh (cpm per 250-mSv Intake)**
0.0	4.48E+03	1.39E+03	4.86E+01
0.2	2.27E+04	2.10E+04	8.75E+03
0.5	3.60E+04	3.46E+04	1.41E+04
1.0	4.31E+04	4.20E+04	1.70E+04
2.0	4.42E+04	4.32E+04	1.74E+04
3.0	4.33E+04	4.23E+04	1.71E+04
4.0	4.25E+04	4.15E+04	1.68E+04
5.0	4.18E+04	4.09E+04	1.65E+04
6.0	4.13E+04	4.04E+04	1.63E+04
7.0	4.08E+04	3.99E+04	1.61E+04
8.0	4.04E+04	3.95E+04	1.59E+04
9.0	4.01E+04	3.92E+04	1.58E+04
10.0	3.98E+04	3.89E+04	1.57E+04
20.0	3.72E+04	3.64E+04	1.46E+04
30.0	3.49E+04	3.41E+04	1.37E+04

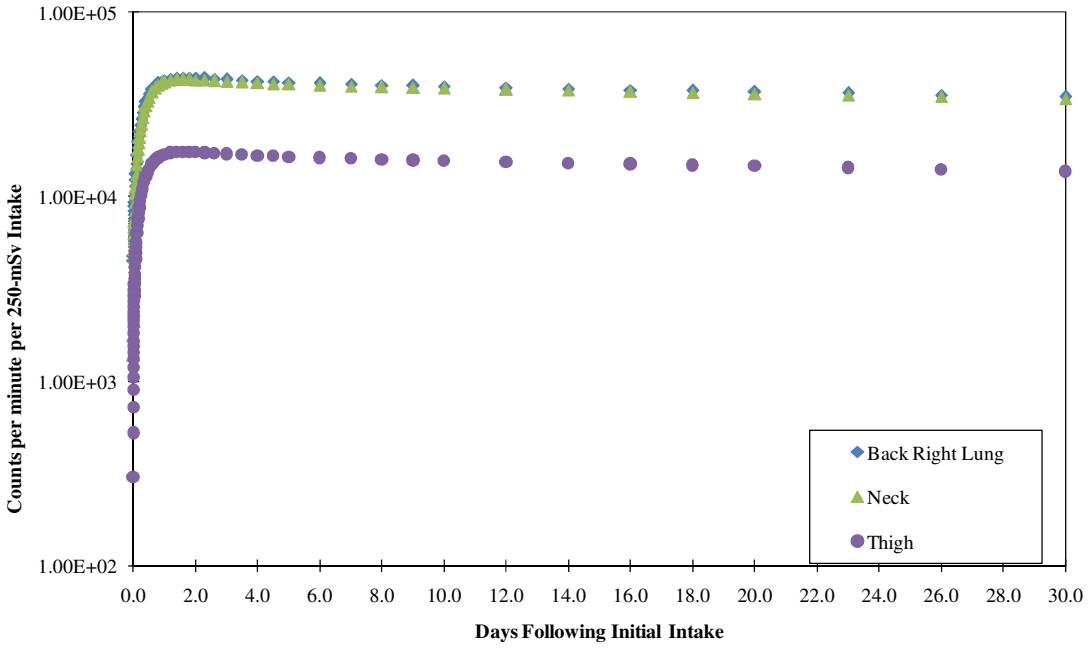

Post Menopausal Adipose Female – I-131

Post Menopausal Adipose Female: I-131 F			
Days	**Back Right Lung (cpm per 250-mSv Intake)**	**Neck (cpm per 250-mSv Intake**	**Thigh (cpm per 250-mSv Intake)**
0.0	2.16E+04	4.63E+03	2.69E+01
0.2	1.57E+04	5.18E+04	4.13E+03
0.5	7.71E+03	6.37E+04	1.83E+03
1.0	3.31E+03	6.82E+04	5.52E+02
2.0	2.22E+03	6.46E+04	2.87E+02
3.0	2.33E+03	5.94E+04	3.74E+02
4.0	2.45E+03	5.44E+04	4.56E+02
5.0	2.51E+03	4.98E+04	5.16E+02
6.0	2.53E+03	4.56E+04	5.57E+02
7.0	2.52E+03	4.18E+04	5.83E+02
8.0	2.48E+03	3.82E+04	5.96E+02
9.0	2.41E+03	3.50E+04	6.00E+02
10.0	2.33E+03	3.20E+04	5.95E+02
20.0	1.33E+03	1.30E+04	3.81E+02
30.0	6.19E+02	5.24E+03	1.84E+02

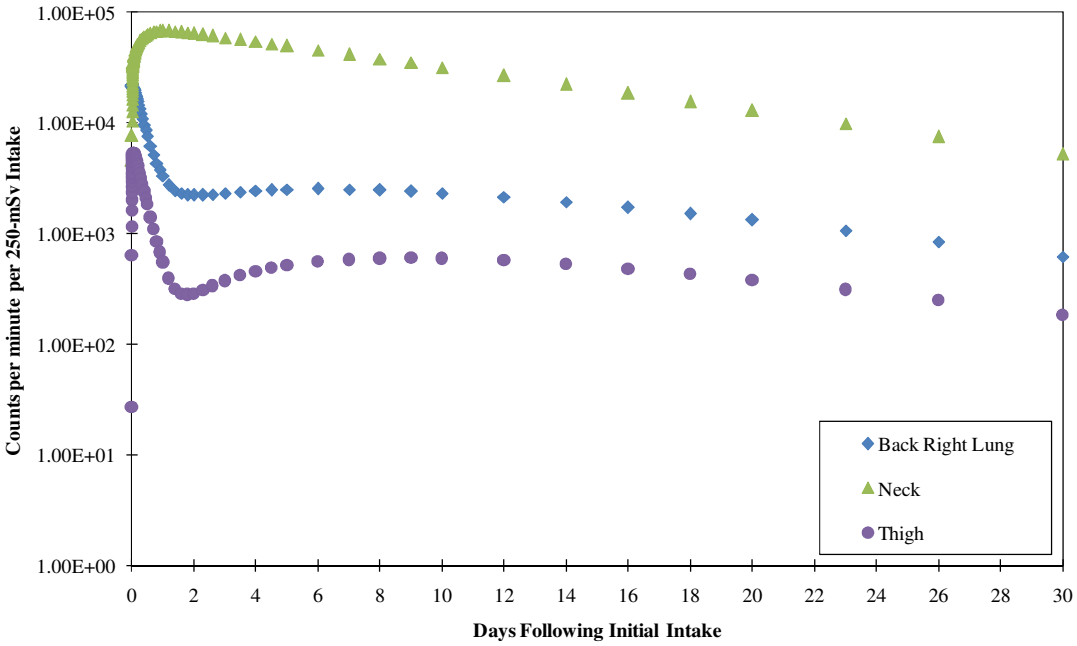

Post Menopausal Adipose Female – I-192

Post Menopausal Adipose Female: Ir-192 M			
Days	**Back Right Lung (cpm per 250-mSv Intake)**	**Neck (cpm per 250-mSv Intake**	**Thigh (cpm per 250-mSv Intake)**
0.0	7.43E+04	1.74E+04	1.21E+02
0.2	8.48E+04	3.14E+04	8.14E+03
0.5	8.98E+04	4.07E+04	1.38E+04
1.0	9.11E+04	4.60E+04	1.71E+04
2.0	8.90E+04	4.70E+04	1.50E+04
3.0	8.71E+04	4.66E+04	1.27E+04
4.0	8.56E+04	4.61E+04	1.16E+04
5.0	8.41E+04	4.57E+04	1.11E+04
6.0	8.28E+04	4.52E+04	1.09E+04
7.0	8.15E+04	4.48E+04	1.08E+04
8.0	8.02E+04	4.45E+04	1.07E+04
9.0	7.90E+04	4.41E+04	1.07E+04
10.0	7.79E+04	4.38E+04	1.06E+04
20.0	6.77E+04	4.08E+04	1.03E+04
30.0	5.97E+04	3.81E+04	1.00E+04

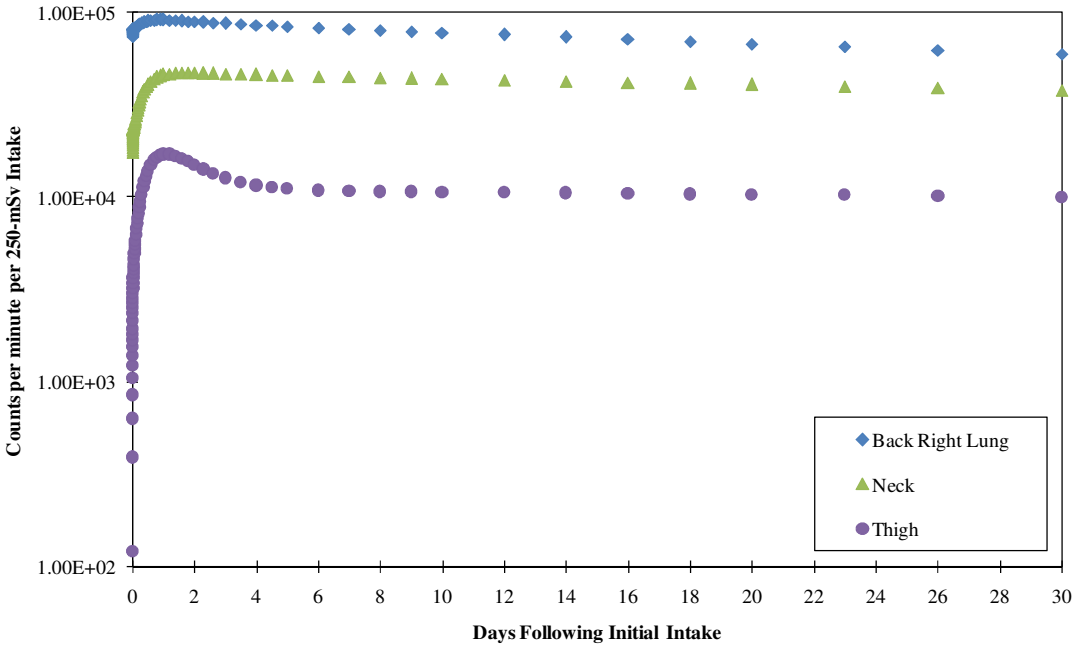

Child – Am-241

Child: Am-241 M			
Days	**Back Right Lung (cpm per 250-mSv Intake)**	**Neck (cpm per 250-mSv Intake**	**Thigh (cpm per 250-mSv Intake)**
0.0	1.25E+01	1.98E+00	1.28E-02
0.2	8.86E+00	1.74E+00	2.90E-01
0.5	7.91E+00	1.48E+00	3.29E-01
1.0	6.88E+00	1.18E+00	3.02E-01
2.0	5.89E+00	8.79E-01	1.84E-01
3.0	5.54E+00	7.64E-01	1.12E-01
4.0	5.42E+00	7.19E-01	8.05E-02
5.0	5.38E+00	7.00E-01	6.83E-02
6.0	5.37E+00	6.90E-01	6.39E-02
7.0	5.38E+00	6.85E-01	6.25E-02
8.0	5.39E+00	6.80E-01	6.23E-02
9.0	5.40E+00	6.77E-01	6.25E-02
10.0	5.42E+00	6.74E-01	6.29E-02
20.0	5.56E+00	6.44E-01	6.65E-02
30.0	5.72E+00	6.19E-01	6.91E-02

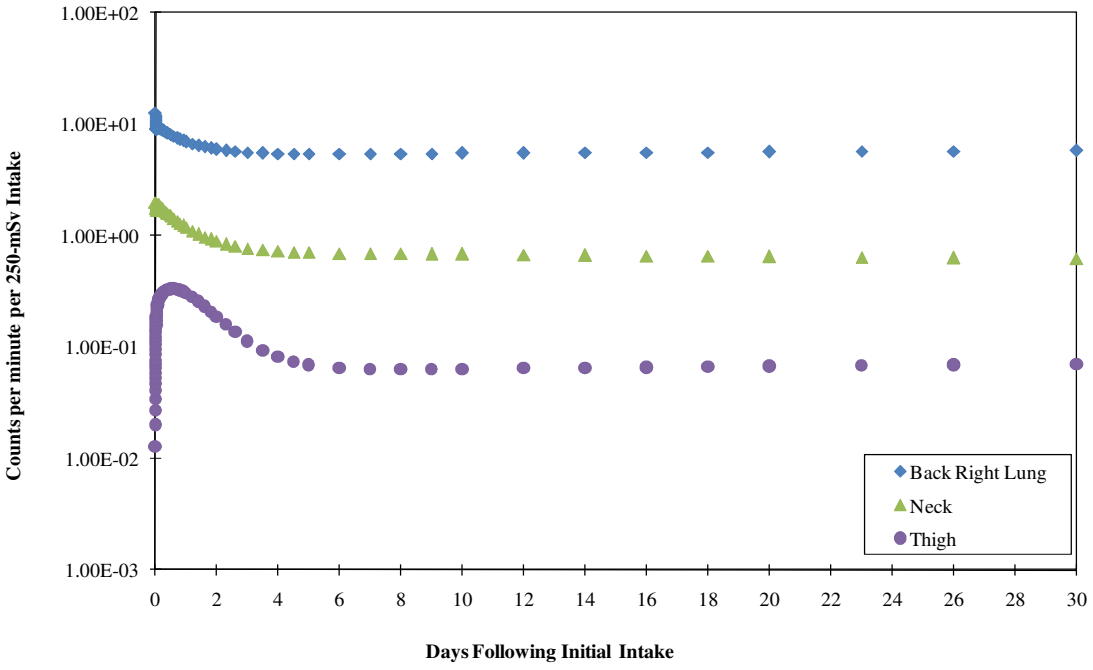

Child – Co-60

Child: ^{60}Co M			
Days	**Back Right Lung (cpm per 250-mSv Intake)**	**Neck (cpm per 250-mSv Intake**	**Thigh (cpm per 250-mSv Intake)**
0.0	3.04E+04	6.59E+03	2.90E+02
0.2	3.59E+04	1.09E+04	4.17E+03
0.5	3.88E+04	1.40E+04	6.43E+03
1.0	4.11E+04	1.69E+04	7.95E+03
2.0	4.20E+04	1.86E+04	6.98E+03
3.0	4.13E+04	1.85E+04	5.68E+03
4.0	4.03E+04	1.79E+04	4.93E+03
5.0	3.93E+04	1.74E+04	4.51E+03
6.0	3.83E+04	1.68E+04	4.25E+03
7.0	3.75E+04	1.63E+04	4.07E+03
8.0	3.67E+04	1.59E+04	3.92E+03
9.0	3.59E+04	1.55E+04	3.80E+03
10.0	3.53E+04	1.51E+04	3.70E+03
20.0	3.06E+04	1.29E+04	3.12E+03
30.0	2.80E+04	1.20E+04	2.93E+03

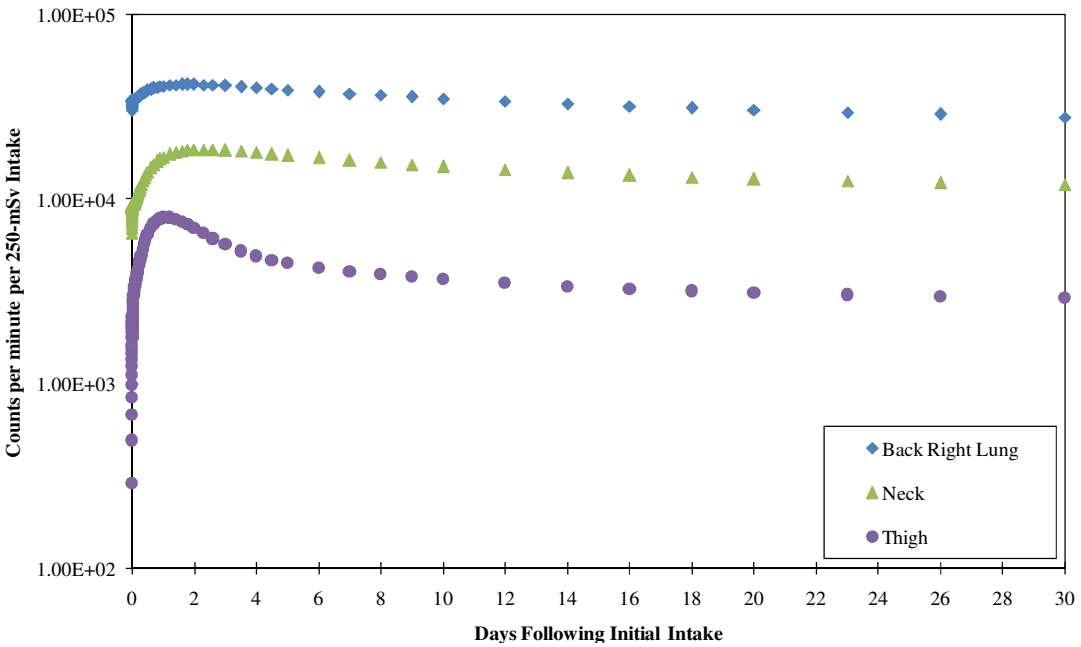

Child – Cs-137

Child: ^{137}Cs F			
Days	**Back Right Lung (cpm per 250-mSv Intake)**	**Neck (cpm per 250-mSv Intake**	**Thigh (cpm per 250-mSv Intake)**
0.0	1.10E+05	2.22E+04	5.81E+02
0.2	5.66E+05	4.01E+05	1.29E+05
0.5	8.75E+05	6.48E+05	2.07E+05
1.0	1.03E+06	7.75E+05	2.48E+05
2.0	1.06E+06	7.96E+05	2.55E+05
3.0	1.04E+06	7.82E+05	2.50E+05
4.0	1.02E+06	7.68E+05	2.45E+05
5.0	1.01E+06	7.58E+05	2.42E+05
6.0	9.95E+05	7.49E+05	2.38E+05
7.0	9.85E+05	7.41E+05	2.36E+05
8.0	9.77E+05	7.34E+05	2.34E+05
9.0	9.69E+05	7.29E+05	2.32E+05
10.0	9.62E+05	7.23E+05	2.30E+05
20.0	9.06E+05	6.79E+05	2.15E+05
30.0	8.55E+05	6.40E+05	2.02E+05

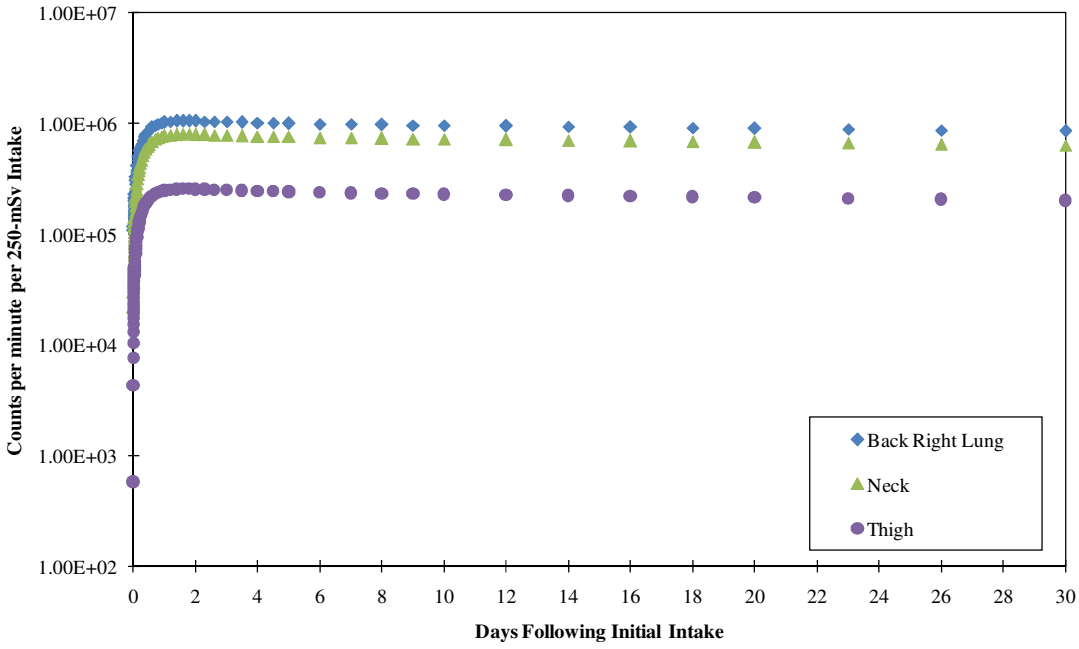

Child – I-131

Child: I-131 F			
Days	**Back Right Lung (cpm per 250-mSv Intake)**	**Neck (cpm per 250-mSv Intake**	**Thigh (cpm per 250-mSv Intake)**
0.0	1.87E+04	3.60E+03	6.23E+01
0.2	1.54E+04	1.66E+04	3.09E+03
0.5	7.87E+03	1.65E+04	1.39E+03
1.0	3.70E+03	1.60E+04	4.03E+02
2.0	2.64E+03	1.49E+04	1.74E+02
3.0	2.71E+03	1.38E+04	2.18E+02
4.0	2.78E+03	1.28E+04	2.64E+02
5.0	2.81E+03	1.18E+04	2.99E+02
6.0	2.80E+03	1.10E+04	3.22E+02
7.0	2.76E+03	1.01E+04	3.37E+02
8.0	2.69E+03	9.35E+03	3.44E+02
9.0	2.61E+03	8.62E+03	3.46E+02
10.0	2.51E+03	7.95E+03	3.43E+02
20.0	1.39E+03	3.41E+03	2.19E+02
30.0	6.43E+02	1.41E+03	1.06E+02

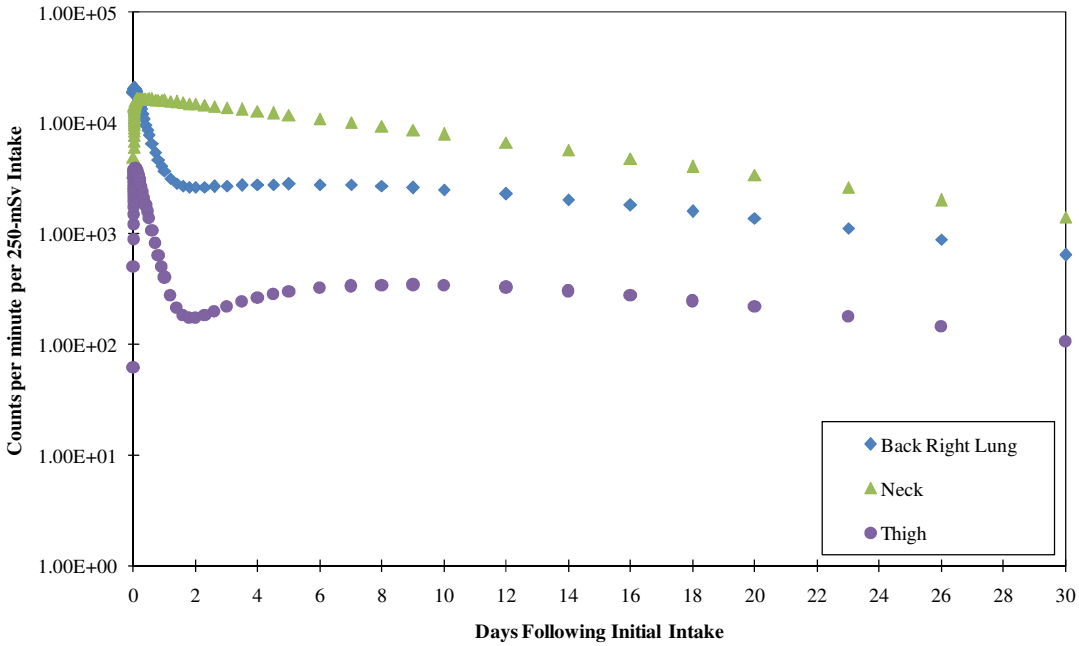

Child – Ir-192

Child: Ir-192 M			
Days	**Back Right Lung (cpm per 250-mSv Intake)**	**Neck (cpm per 250-mSv Intake**	**Thigh (cpm per 250-mSv Intake)**
0.0	1.10E+05	2.30E+04	4.20E+02
0.2	1.30E+05	3.95E+04	1.23E+04
0.5	1.39E+05	4.97E+04	2.01E+04
1.0	1.41E+05	5.51E+04	2.43E+04
2.0	1.38E+05	5.58E+04	1.96E+04
3.0	1.35E+05	5.50E+04	1.51E+04
4.0	1.32E+05	5.44E+04	1.29E+04
5.0	1.30E+05	5.38E+04	1.20E+04
6.0	1.28E+05	5.32E+04	1.17E+04
7.0	1.26E+05	5.27E+04	1.15E+04
8.0	1.24E+05	5.23E+04	1.14E+04
9.0	1.22E+05	5.18E+04	1.13E+04
10.0	1.21E+05	5.14E+04	1.13E+04
20.0	1.06E+05	4.76E+04	1.09E+04
30.0	9.35E+04	4.43E+04	1.05E+04

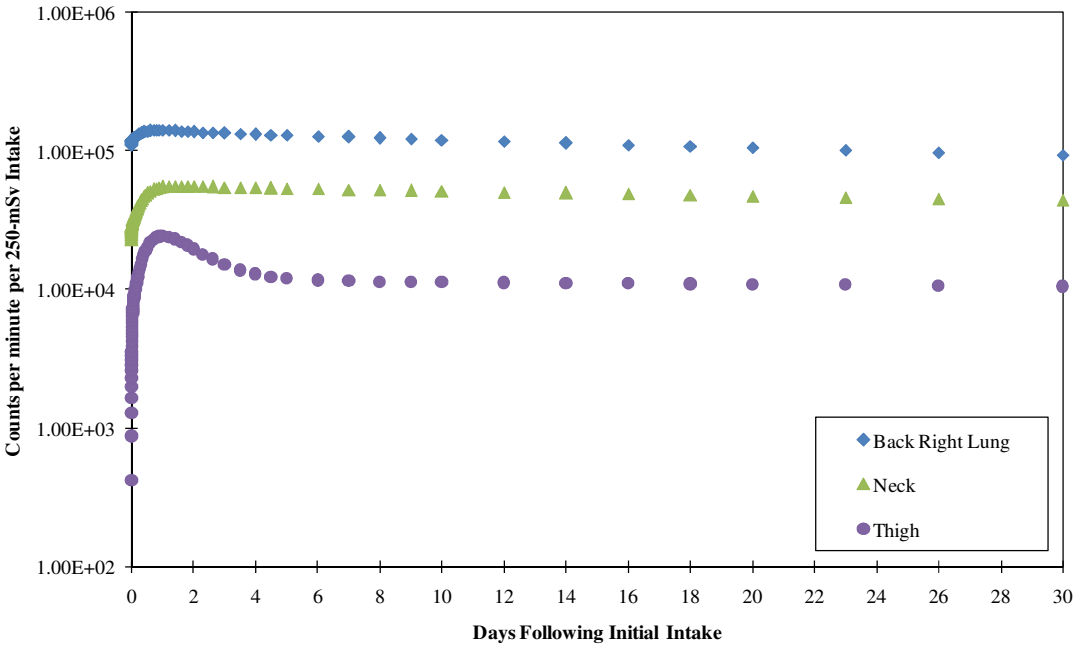

APPENDIX D: SAMPLE TRIAGE PROCEDURE SHEET FOR FIRST RESPONDERS

Canberra 802-2x2 NaI(Tl) Spectrometer (Male)

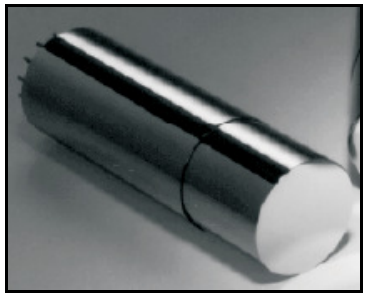

Set-Up (by Trained Technician)

- A trained technician must hook the detector up to the following NIM modules with the recommended settings:
  - High-voltage power supply: *0.91kV*
  - Preamplifier
  - Amplifier:
    - Shaping Time *0.5µs*
    - Output: *Unipolar* (to MCA)
  - Multichannel Analyzer (MCA):
    - *1024 channels*
- The amplifier coarse and fine gain should be adjusted such that the entire photopeak for the radionuclide of interest is visible on MCA interface
- The counting region of interest (ROI) is dependent on the radionuclide to be detected. The counting ROI channels should be set to encapsulate the following photopeak(s).

Nuclide	Peak(s) in ROI (keV)
Co-60	1173.2, 1332.5
Cs-137	661.7
I-131	364.5
Ir-192	316.5

- The detector should be set to acquire for a live time of time of 60 seconds.

Basic Operation (by Screening Personnel)

To Determine Background:

- First a background reading must be taken with no contaminated samples or patients present.
- Background should be acquired for a live time of 60 seconds (= 1 minute live time).
- To determine the BACKGROUND count rate in counts per minute (cpm), take the integral area counts in the ROI.
- *For example:* If you get 1200 counts in the ROI area in 60 seconds live time, the count rate is:
  - 1200 counts in 60 seconds = 1200 counts per minute

To Determine the Net Count Rate for Screening:

- Place the detector over the patient's back right lung.
- Use the software interface to start counting for 60 seconds live time. This is the number of GROSS counts in 1 minute live time.
- To determine the NET count rate (cpm), subtract the BACKGROUND from the GROSS count rates

- *For example:* If you get a reading of 18,000 counts in 60 seconds live time from a patient, this corresponds to:
  - 18,000counts in 60 seconds = 18,000 cpm
  - NET (cpm)= GROSS (cpm) – BACKGROUND (cpm)
    = 18,000-1200 = 16,800 cpm

- The NET count rate must be at least 100 cpm above background to be considered detectable in a live time of at least 60 seconds.
- The screening level is exceeded if:
  - (A) the NET count rate exceeds the count rate in the screening level table
  - *Optional: (*B) As secondary verification to method (A) – if the detector dead time exceeds the following values for a given nuclide:

Nuclide	Dead Time Threshold
Co-60	14%
Cs-137	40%
I-131	4%
Ir-192	13%

Canberra 802-2x2 NaI(Tl) (Reference Male) Screening Levels

Time (days)	Co-60 (cpm)	Cs-137 (cpm)	I-131 (cpm)	Ir-192 (cpm)
0.0	2.26E+04	3.58E+04	3.58E+04	7.87E+04
0.2	2.58E+04	1.37E+05	2.24E+04	8.97E+04
0.5	2.71E+04	2.14E+05	1.04E+04	9.31E+04
1.0	2.76E+04	2.55E+05	3.85E+03	9.25E+04
2.0	2.76E+04	2.62E+05	2.24E+03	8.93E+04
3.0	2.70E+04	2.57E+05	2.43E+03	8.71E+04
4.0	2.63E+04	2.52E+05	2.64E+03	8.54E+04
5.0	2.57E+04	2.48E+05	2.78E+03	8.39E+04
6.0	2.51E+04	2.45E+05	2.85E+03	8.25E+04
7.0	2.46E+04	2.42E+05	2.88E+03	8.11E+04
8.0	2.41E+04	2.40E+05	2.86E+03	7.98E+04
9.0	2.37E+04	2.38E+05	2.81E+03	7.86E+04
10.0	2.32E+04	2.36E+05	2.74E+03	7.73E+04
20.0	2.02E+04	2.21E+05	1.62E+03	6.68E+04
30.0	1.83E+04	2.08E+05	7.65E+02	5.84E+04

APPENDIX E: CONDENSED PROCEDURE SHEET FOR FIRST RESPONDERS

Canberra 802-2x2 NaI(Tl) Spectrometer

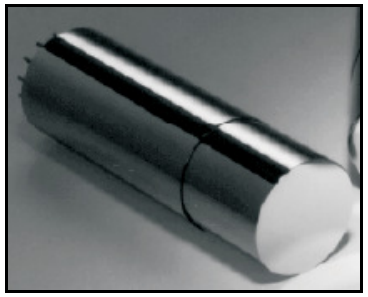

Set-Up (by Trained Technician)

- A trained technician must hook the detector up to the following NIM modules with the recommended settings:
  - High-voltage power supply: *0.91kV*
  - Preamplifier
  - Amplifier:
    - Shaping Time *0.5µs*
    - Output: *Unipolar* (to MCA)
  - Multichannel Analyzer (MCA):
    - *1024 channels*
- The amplifier coarse and fine gain should be adjusted such that the entire photopeak for the radionuclide of interest is visible on MCA interface
- The counting region of interest (ROI) is dependent on the radionuclide to be detected. The counting ROI channels should be set to encapsulate the following photopeak(s).

Nuclide	Peak(s) in ROI (keV)
Co-60	1173.2, 1332.5
Cs-137	661.7
I-131	364.5
Ir-192	316.5

- The detector should be set to acquire for a live time of time of 60 seconds.

Basic Operation (by Screening Personnel)

To Determine Background:

- First a background reading must be taken with no contaminated samples or patients present.
- Background should be acquired for a live time of 60 seconds (= 1 minute live time).
- To determine the BACKGROUND count rate in counts per minute (cpm), take the integral area counts in the ROI.
- *For example:* If you get 1200 counts in the ROI area in 60 seconds live time, the count rate is:
  - 1200 counts in 60 seconds = 1200 counts per minute

To Determine the Net Count Rate for Screening:

- Place the detector over the patient's back right lung.
- Use the software interface to start counting for 60 seconds live time. This is the number of GROSS counts in 1 minute live time.
- To determine the NET count rate (cpm), subtract the BACKGROUND from the GROSS count rates

- *For example:* If you get a reading of 18,000 counts in 60 seconds live time from a patient, this corresponds to:
  - 18,000counts in 60 seconds = 18,000 cpm
  - NET (cpm)= GROSS (cpm) – BACKGROUND (cpm)
    = 18,000-1200 = 16,800 cpm

- The NET count rate must be at least 100 cpm above background to be considered detectable in a live time of at least 60 seconds.
- The screening level is exceeded if:
  - (A) the NET count rate exceeds the count rate in the screening level table
  - *Optional: (*B) As secondary verification to method (A) – if the detector dead time exceeds the following values for a given nuclide:

Nuclide	Dead Time Threshold
Co-60	14%
Cs-137	40%
I-131	4%
Ir-192	13%

ADULT
Screening Levels

Time (days)	Co-60 (cpm)	Cs-137 (cpm)	I-131 (cpm)	Ir-192 (cpm)
0.0	1.28E+04	1.91E+04	1.86E+04	6.46E+04
0.2	1.46E+04	9.11E+04	1.35E+04	7.32E+04
0.5	1.57E+04	1.45E+05	6.51E+03	7.80E+04
1.0	1.66E+04	1.74E+05	2.69E+03	7.93E+04
2.0	1.69E+04	1.78E+05	1.75E+03	7.76E+04
3.0	1.66E+04	1.75E+05	1.87E+03	7.59E+04
4.0	1.62E+04	1.72E+05	1.98E+03	7.46E+04
5.0	1.58E+04	1.69E+05	2.05E+03	7.33E+04
6.0	1.55E+04	1.67E+05	2.08E+03	7.22E+04
7.0	1.51E+04	1.65E+05	2.08E+03	7.10E+04
8.0	1.48E+04	1.63E+05	2.05E+03	7.00E+04
9.0	1.45E+04	1.62E+05	2.01E+03	6.89E+04
10.0	1.42E+04	1.61E+05	1.95E+03	6.79E+04
20.0	1.23E+04	1.50E+05	1.12E+03	5.91E+04
30.0	1.12E+04	1.41E+05	5.27E+02	5.21E+04

CHILD
Screening Levels

Time (days)	Co-60 (cpm)	Cs-137 (cpm)	I-131 (cpm)	Ir-192 (cpm)
0.0	3.04E+04	1.10E+05	1.87E+04	1.10E+05
0.2	3.59E+04	5.66E+05	1.54E+04	1.30E+05
0.5	3.88E+04	8.75E+05	7.87E+03	1.39E+05
1.0	4.11E+04	1.03E+06	3.70E+03	1.41E+05
2.0	4.20E+04	1.06E+06	2.64E+03	1.38E+05
3.0	4.13E+04	1.04E+06	2.71E+03	1.35E+05
4.0	4.03E+04	1.02E+06	2.78E+03	1.32E+05
5.0	3.93E+04	1.01E+06	2.81E+03	1.30E+05
6.0	3.83E+04	9.95E+05	2.80E+03	1.28E+05
7.0	3.75E+04	9.85E+05	2.76E+03	1.26E+05
8.0	3.67E+04	9.77E+05	2.69E+03	1.24E+05
9.0	3.59E+04	9.69E+05	2.61E+03	1.22E+05
10.0	3.53E+04	9.62E+05	2.51E+03	1.21E+05
20.0	3.06E+04	9.06E+05	1.39E+03	1.06E+05
30.0	2.80E+04	8.55E+05	6.43E+02	9.35E+04

REFERENCES

1. X-5 Monte Carlo Team. MCNP A General Monte Carlo N-Particle Transport Code Version 5, Volumes I, II, and III: User's Guide. (Los Alamos National Laboratory/LA-CP-03-0245) (2003).

2. Eckerman, K. F., Cristy, M. and Ryman, J. C. ORNL Mathematical Phantom Series. (Oak Ridge National Laboratory) (1996).

3. Ansari, A. Meeting on handheld detector project. (2008).

4. Eckerman, K. F., Leggett, R. W., Cristy, M., Nelson, C. B., Ryman, J. C., Sjoreen, A. L. and Ward, R. C. Dose and Risk Calculation Software. (Oak Ridge: ORNL/TM-2001/190) (2006).

5. Allison, G. Nuclear Terrorism: The Ultimate Preventable Catastrophe. (New York: Henry Holt and Company) (2004).

6. DOE/NRC Interagency Working Group on Radiological Dispersal Devices. Radiological Dispersal Devices: An Initial Study To Identify Radioactive Materials of Greatest Concern And Approaches to their Tracking, Tagging, And Disposition. Report to the Nuclear Regulatory Commission and the Secretary of Energy. (2003).

7. Department of Homeland Security Working Group on Radiological Dispersal Device Preparedness. Medical Treatment of Radiological Casualties. (Department of Homeland Security) (2003).

8. Oliveira, C. A. N., Lourenco, M. C., Dantas, B. M. and Lucena, E. A. Design and Operation of a Whole- body Monitoring System for the Goiania Radiation Accident. Health Physics. 60, 51-55 (1991).

9. Kramer, G. H., Capello, K. and Hauck, B. M. Evaluation of Two Commercially Available Portal Monitors for Emergency Response. Health Physics. 92, S50-S56 (2007).

10. Kramer, G. H., Capello, K. and Hauck, B. M. The HML's New Field Deployable, High-Resolution Whole Body Counter. Health Physics. 89, S60-S68 (2005).

11. Kramer, G. H. and Hauck, B. M. Fundamental Uncertainties in Lung Counting. Health Physics. 93, 318-324 (2007).

12. Kramer, G. H., Crowley, P. and Burns, L. C. Uncertainty in the Activity Estimate from a Lung Count Due to the Variability in Chest Wall Thickness Profile. Health Physics. 78, 739-743 (2000).

13. Anigstein, R., Olsher, R. H. and Engdahl, J. C. Use of Radiation Detection, Measuring, and Imaging Instruments to Assess Internal Contamination from Inhaled Radionuclides. Part I: Field Tests and Monte Carlo Simulations Using Anthropomorphic Phantoms; Part II: Field Tests and Monte Carlo Simulations Using Anthropomorphic Phantoms (2007).

14. Lorio, R. A. Feasibility of Determining Radioactivity in Lungs Using A Thyroid Uptake Counter: A Thesis Presented to the Faculty. (Atlanta: Georgia Institute of Technology) (2005).

15. Scarboro, S. B. The Use of a Thyroid Uptake System for Assaying Internal Contamination Following a Radioactive Dispersal Event. A Thesis Presented to the Faculty. (Atlanta: Georgia Institute of Technology) (2008).

16. Canberra Industries. Canberra Scintillation Detectors - Model 802. (2003).

17. Saint Gobain Crystals. Physical Properties of Common Inorganic Scintillators. (2009).

18. Canberra Industries. Genie 2000 Gamma Analysis Software. (Canberra Industries) (2004).

19. Wang, Z. and Hertel, N. Determination of dosimetric characteristics of OptiSeed a plastic brachytherapy Pd-103 source. Applied Radiation and Isotopes. 63, 311-321 (2005).

20. Eckerman, K. F. and Sjoreen, A. L. Radiological Toolbox. (Oak Ridge: ORNL/TM-2004/27R1) (2003).

21. Knoll, G. F. Radiation Detection and Measurement. (New York: John Wiley and Sons) (2000).

22. Van Riper, K. A. Bodybuilder. (2004).

23. Tanner, J. E. Current Dose Studies on Effective Neutron Dose Equivalent. (Las Vegas, NV) (1991).

24. International Commission on Radiological Protection ICRP Publication 23: Report of the Task Group on Reference Male (1975). Annals of the ICRP. 4(1980).

25. Simpkins, R. and Hertel, N. Neutron Organ Dose and the Influence of Adipose Tissue. Proceedings of Radiation Protection and Shielding Division 12th Biennial Topical Meeting(2002).

26. Burns, K. A. Monte Carlo Simulations for Homeland Security Using Simulations for Homeland Security Using Anthropomorphic Phantoms: A Thesis Presented to the Faculty. (Atlanta: Georgia Institute of Technology) (2008).

27. International Commission on Radiological Protection ICRP Publication 66: Human Respiratory Tract Model for Radiological Protection. Annals of the ICRP. 24(1994).

28. Schwarz, R. A. MCNP Visual Editor. (2005).

29. LeJeune, J. Personal Communication. (2008).

30. Hutchinson, J. D. Handheld Gamma-Ray Spectrometry for Assaying Radioactive Materials in Lungs: A Thesis Presented to the Faculty. (Atlanta: Georgia Institute of Technology) (2005).

31. Burgett, E. Personal Communication. (2007).

32. National Institute of Standards and Technology. NIST Standard Reference Materials. (2009).

33. Williams, T. and Kelley, C. Gnuplot. (2007).

34. World Health Organization. Global Database on Body Mass Index. (2006).

35. International Commission on Radiological Protection ICRP Publication 30: Limits for Intakes by Workers, Part 1. Annals of the ICRP. 2(1979).

36. International Commission on Radiological Protection ICRP Publication 67: Age-Dependent Doses to Members of the Public from Intake of Radionuclides, Part 2. Annals of the ICRP. 23(1993).

37. International Commission on Radiological Protection ICRP Publication 68: Dose Coefficients for Intakes of Radionuclides by Workers. Annals of the ICRP. 24(1993).

38. International Commission on Radiological Protection ICRP Publication 72: Age-dependent dose to members of the public from intake of radionuclides, Part 5 Compilation of ingestion and inhalation dose coefficients. Annals of the ICRP. 26(1996).

39. Barnett, V. and Lewis, T. Outliers in Statistical Data. Wiley) (1994).

40. Strom, D. J. False Alarms, True Alarms, and Statistics: Correct Usage of Decision Level and Minimum Detectable Amount. Proceedings of Health Physics Society Annual Meeting, Continuing Education Lecture. Minneapolis, MN, July 15(1998).

41. Manger, R. P. Assessing the Dose Received by the Victims of a Radiological Dispersal Device with Geiger-Mueller Detectors. A Thesis Presented to the Faculty. (Atlanta: Georgia Institute of Technology) (2008).